CONTENTS

ABSTRACTS

Adam Adamowicz, Piotr Grześ
Finite Element Analysis of thermal Stresses in a Pad-Disc Brake System (a Review)

Rapid temperature change in components of the sliding systems induces thermal stresses due to thermal expansion. This effect is particularly evident in disc brakes working under high thermal loads. This paper deals with the finite element modelling of frictional heating process in disc brakes and clutches to study the temperature and stress distributions during operation.

Paweł Baranowski, Jerzy Małachowski, Łukasz Mazurkiewicz, Krzysztof Damaziak
Dynamic Testing of Copper Material – Numerical Approach

Split Hopkinson pressure bar (SHPB) is one of the most important and recognisable apparatus used for characterizing the dynamic behaviour of various materials. Incident pulse generated one the incident bar usually have a rectangular shape, which is proper for some materials but for others is not. Therefore, several methods of shaping the incident pulse are used for obtaining constant strain rate conditions during tests. Very often pulse shapers made of copper or similar material are implemented due to its softness properties. In this paper such material was investigated using the FE model of SHPB. Its mechanical behaviour was characterised with and without copper disc between the striker and incident bar. Numerical simulations were carried out using explicit LS-DYNA code. Two different methods were used for modelling the copper sample: typical finite Lagrangian elements and meshless Smoothed Particle Hydrodynamics (SPH) method. As a result of two techniques used axial stress-strain characteristics were compared for three different striker's velocity with an influence of the copper pulse shaper taking into account. Finally, FE and SPH method was compared with taking into consideration: the efficiency, computer memory and power requirements, complexity of methods and time of simulation.

Józef Błachnio
Analysis of Technical Condition Assessment of Gas Turbine Blades with Non-Destructive Methods

Structural components of gas turbines, particularly the blades, sustain a variety of damages during the operation process. The most frequent cause of these damages are the overheating and thermal fatigue of the material. A primary technique to assess condition of the blades is the metallographic examination. In spite of the fact that metallographic analysis delivers much more information on the structure of examined blade material, it is a type of destructive test resulting in the destruction of the blade which makes further utilization of the item impossible. The paper has been intended to discuss non-destructive testing methods and to present capabilities of applying them to diagnose objectively changes in the microstructure of a turbine blade with computer software engaged to assist with the analyses. The following techniques are discussed: a visual method, based on the processing of images of the material surface in visible light, active thermography, based on the detection of infrared radiation, and the X-ray computed tomography. All these are new non-destructive methods of assessing technical condition of structural components of machines. They have been intensively developed at research centers worldwide, and in Poland. The computer-aided visual method of analyzing images enables diagnosis of the condition of turbine blades, without the necessity of dismantling of the turbine. On the other hand, the active thermography and the X-ray computed tomography, although more sensitive and more reliable, can both be used with the blades dismounted from the turbine. If applied in a complex way, the non-destructive methods presented in this paper, are expected to increase significantly probability of detecting changes in the blade's condition, which in turn would be advantageous to reliability and safety of gas turbine service.

Błachnio Józef, Zabrocka Iwona
Image of the Surface of Gas Turbine Blade as Diagnostic Signal

This paper outlines a non-destructive method that is suitable for evaluation of condition demonstrated by gas turbine blades and is based on digital processing of images acquired from the blade surface in visible light. To enable high clearness of these images the particular attention is paid to the problem of how to provide optimum conditions for investigations and mitigate geometrical distortions of images acquired from maintenance operations. The paper demonstrates that there are relationships between operation lifetime of blades and discoloration of their surfaces due to overheating of the blade material. These relationships are revealed by digital analysis of images acquired for the blade surfaces and expressed as statistical parameter of the first and second order. To improve unambiguity of the analysis results a low-pass filter was applied. It was demonstrated that these relationships are suitable for evaluation how much the status of the blade material microstructure is altered.

Tomáš Brestovič, Natália Jasminská
Software Support Development for Numerical Solution of ANSYS CFX

The paper deals with possibilities to apply a new developed software support for simulation programme ANSYS CFX. A direct export of heat-transfer coefficients into variables used under edge conditions as well as of physical properties of gas mixtures into material properties during simulation solution of technical tasks means a significant saving of time. The paper summarizes in detail description of the software for calculation of heat-transfer coefficient during free convection (HTC-FC) and of material properties of gas mixture (MPGM) that enable to export calculated data directly into the text files which can be imported then into the programme ANSYS CFX.

Ihor Dzioba, Robert Pała, Tadeusz Pała

Temperature Dependency of Fracture Toughness of High-Strength Ferritic Steel Hardox-400

The paper presents experimental results of the changes of strength and fracture toughness characteristics of high-strength ferritic steel Hardox-400 in the temperature range from -100 OC to +20 OC. It has been shown that the strength characteristics values increase linearly with lowering the temperature. Changes of fracture toughness characteristics from temperature are more complex and they are dependent on thickness of the tested specimens.

Ihor Dzioba, Tadeusz Pała, Ilkka Valkonen

Strength and Fracture Toughness of the Welded Joints Made of High-Strength Ferritic Steel

The paper presents experimental results of the characteristics of strength and fracture toughness of the material from the different zones of welded joints made of different participation of the linear welding energy. Strength characteristics and fracture toughness were determined in the weld material, in the area of fusion line, in the material of the heat affected zone and in the base material.

Andriy Kotsyuba

Contact Interaction of Rigid Stamp and Infinite Orthotropic Plate with Close to Elliptical Hole

Numerical method of finding the contact stresses under the stamp of complex shape for the case of orthotropic plates with close to an elliptical hole, which based on constructed in Bozhydarnik et al., (2007) algorithm, is developed. The distribution of contact stresses under the stamp, which shape matches the shape of the hole, is investigated.

Ewa Och

Frictional Heating During Sliding of Two Semi-Spaces with Simple Thermal Nonlinearities

In the article the nonstationary thermal problem of friction for two semi-spaces with taking into account their imperfect thermal contact and thermosensitivity of materials (simple nonlinearity), has been considered. The linearization of this problem has been carried out using Kirchhoff transformation, and next using the Laplace integral transform. The analytical solution to the problem in the case of constant speed sliding, has been obtained. On the basis of the obtained solutions and using Duhamel's formula, the analytical solution to the problem for sliding with constant deceleration, has been obtained, too. The results of numerical analysis are presented for two friction pairs.

Bogdan Sapiński, Marcin Węgrzynowski

Experimental Setup for Testing Rotary MR Dampers with Energy Harvesting Capability

The experimental setup has been developed for laboratory testing of electromechanical energy transducers and rotary magnetorheological (MR) dampers. The design objectives are outlined and the parameters of the key elements of the setup are summarised. The structure of the mechanical and measurement and control systems is presented. Results of functional testing of a newly developed transducer and a MR rotary damper are summarised.

FINITE ELEMENT ANALYSIS OF THERMAL STRESSES IN A PAD-DISC BRAKE SYSTEM (A REVIEW)

Adam ADAMOWICZ*, **Piotr GRZES***

Faculty of Mechanical Engineering, Department of Mechanics and Applied Computer Science, Bialystok University of Technology
ul. Wiejska Street 45C, 15-351 Bialystok, Poland

a.adamowicz@pb.edu.pl, p.grzes@pb.edu.pl

Abstract: Rapid temperature change in components of the sliding systems induces thermal stresses due to thermal expansion. This effect is particularly evident in disc brakes working under high thermal loads. This paper deals with the finite element modelling of frictional heating process in disc brakes and clutches to study the temperature and stress distributions during operation.

Key words: Pad-disc brake system, Temperature, Thermal stresses, Finite element method

1. INTRODUCTION

Large amount of mechanical energy converted into heat during braking leads to temperature increase in friction elements (Fig. 1). This may have a significant influence on the thermal behaviour of the brake system. An increase in the temperature above a permissible value, frequently leads to undesirable effects such as fluctuations of the coefficient of friction, brake fade, thermal cracks, thermal deformations of the disc, degradation of the material of the pad, etc. The review articles on analytical methods to study the thermal problems of friction are given in monographs (Chichinadze, 1967; Chichinadze et al., 1979; Balakin and Sergienko, 1999) and in articles (Yevtushenko et al., 2000; Matysiak and Yevtushenko, 2000). The finite element analyses of the transient temperature fields in disc brakes are given in articles by Yevtushenko and Grzes (2010, 2014). The authors reported the techniques employed to develop the FE models of the pad-disc brake systems and clutches aiming to examine the axisymmetric and three-dimensional temperature distributions during operation. In this paper numerical studies concerning the thermal stresses in disc brakes and clutches are given and the main factors affecting the stress distributions are discussed.
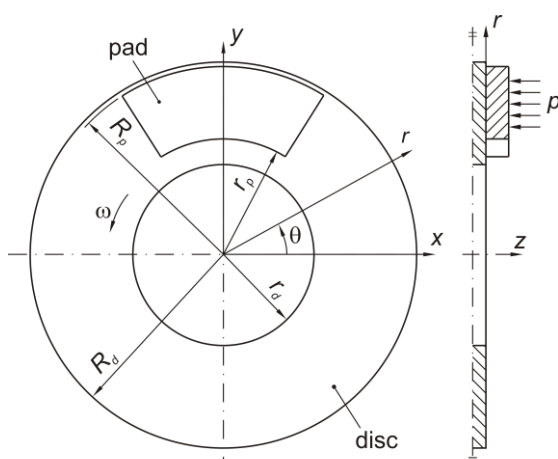

Fig. 1. A schematic diagram of a pad-disc brake system

2. THERMAL STRESSES IN DISC BRAKES

The axisymmetric transient temperature and the quasi-static thermal stress distributions in the discs of the wet clutch were determined numerically in article by Zagrodzki (1985). Two different types of the discs were analysed: the first was made entirely of steel, whereas the second was additionally coated with the friction material. At the first step of the study, the temperature fields in both types of the discs (arranged alternately) were calculated using the finite difference method (FDM). Next the thermal stresses using the finite element method (FEM) were determined only for the disc made entirely of steel, which stemmed from its frequent failure during the operation process. The contact pressure on the friction surfaces was constant and uniformly distributed. The convective heat transfer conditions according to Newton's law of cooling in the axisymmetric model were taken into account. As stated it did not have a significant effect on the volume temperature, but might have had affected the change in the local surface temperature and hence the stress. In the area of frictional contact, the temperature equality condition was used and it was assumed that the sum of the heat flux densities is equal to the power density of friction forces. The calculation of the temperature and stresses were uncoupled. Based on the carried out analysis, it was found that the determined maximum equivalent Huber-Mises stresses did not exceed the yield strength of the tested material. The obtained results were insufficient to predict the damage of the clutch discs. Due to the axial symmetry, the circumferential stress component was at the same time the principal stress component. The directions of the normal stress tensor components, almost coincided with the directions of principal stresses, therefore normal stress components were analysed the as the principal stresses. The order of the magnitude of axial stress was about 30 times lower than the circumferential and the radial stress. Near the friction surface the stresses (circumferential and radial) were compressive. Inside the disc the sign changed to the opposite. During the of the operation of the clutch, the temperature was proportional to the radial coordinate thus the radial and the circumferential stresses also varied in radial direction. The concluding remarks indicated that the essential impact on the value of the circumferential stress component has the radial tem-

191

perature gradient resulting from the difference in the relative sliding velocity of the discs. The authors presented this relationship in the diagram. The sign of circumferential stress in the presence of only the component of the axial temperature gradient were shown, then only the radial component and eventually the combined effect of both components were presented. As a result of superposition of the two components of the temperature gradient, the circumferential component of the stress was the highest on the outer surface (compression) and on the inner surface of the disc (tension). After the standstill, a separation between the signs of circumferential component occurred: a positive (inner side) and a negative (outer side). The values of the stress when disconnected discs were not as high as during the engagement of the clutch, however, lasted for a relatively long time. It was pointed out that the effect of the radial component of the temperature gradient on the values and the distribution of the stresses is crucial. It should also be noted, however, that the operating characteristics of the clutch varies from the corresponding characteristics of the disc brake. Thereby the stress distribution and the rate of its change may also differ. The equivalent Huber-Mises stress did not exceeded the yield strength of typical materials used for the clutch discs.

Assuming that the distribution of the contact pressure on the working surfaces of the discs of a wet clutch is uniform and independent of the thermal state of the considered system, the equivalent stress values do not exceed the yield strength under normal operating conditions according to Zagrodzki (1985). An attempt to qualify these assumptions have been made in article (Zagrodzki, 1990). A multidisc clutch consisting of the nine deformable discs made entirely of steel and coated with friction material were analysed. The calculated axisymmetric pressure distributions revealed its decrease with the increase in the radial distance, at the beginning of the operation of the clutch. Further two local extremes were formed, which stemmed from the boundary conditions due to the non-symmetrical geometry of the clutch. In the middle of the clutch system, the discs were heated more intensely than those at the edges (the heating took place only on the one side of the disc). It has also been observed that the discs were subjected to displacements and rotation. The detailed observation revealed that the discs were also folded. This effect has led to the uneven pressure distribution and the formation of the local heating contact areas. The equivalent Huber-Mises stress reached 380 MPa. Double reduction in Young's modulus of the friction material allowed to reduce the stress also double. Wear of the material was neglected, which, as stated could weaken the thermoelastic instability phenomenon.

The thermoelastic instability for the pad-disc brake system during a single braking at constant speed was studied by Choi and Lee (2003). The axisymmetric transient temperature fields of the pad and the disc were analysed. An influence of the angular speed and the load acting as the hydraulic pressure on a real contact area and the temperature of the friction elements were examined. The changes in the normal components of the stress tensor were analysed during braking process. Both the compressive and the tensile circumferential stresses increased during braking until the end of the process and it was the highest stress tensor component. Slightly lower values were obtained for the radial component, which after some time remained on the same level.

The coupled thermomechanical analysis for the pad-disc brake system during several applications at linearly decreasing speed was carried out in article by Choi and Lee (2004). The

influence of the properties of materials (specific heat, thermal expansion coefficient, thermal conductivity, Young's modulus) on the temperature field and the real contact area was studied. Based on calculations it was concluded that the maximum stress was reached for the circumferential component, and its value was dependent upon the number of brake applications.

The uncoupled thermomechanical analysis for the pad-disc brake system of a rolling stock (TGV) to indicate the factor affecting the disc failure was carried out in article (Dufrenoy and Weichert, 2003). The five major types of thermal gradients generated in the brake disc and their impact on the initiation and growth of the cracks were presented. It was established that the most critical in initiating of the cracks was the distribution of the hot spots in the circumference of the rubbing path, so called buckling mode of the disc. The temperature and the stresses due to the mechanical and the thermal loads were calculated. At the first stage an effect of the mechanical load, resulting from the pressure and the friction force on the stresses in the pad-disc system based on the three-dimensional contact model was studied. It was found that the maximum equivalent stress in the pad was several times lower than the limit values and can be neglected in heat conduction problems of friction. Furthermore it was also observed that the obtained stress distribution reflected only the initial state of the braking process. In the next step, the uncoupled thermomechanical analysis was performed. It was assumed that the distribution of the hot spots in the circumference is regular and independent of time. The three-dimensional model of the brake disc was developed. Due to the axial symmetry of the geometry of the disc and a regular distribution of the six hot spots in the circumference of the rubbing path, the calculation area was restricted to 1/12 segment of the disc. First the number of hot spots and the distribution of contact pressure was calculated. Next the parabolic type distribution of the heat flux density of a single spot was applied. The circumferential stress and the plastic deformation using the elastic-plastic model were determined. The outcomes of the FE modelling agreed well with the results of the thermographic measurements. Next, the residual stresses were determined experimentally using the strain gage hole drilling method. An emphasis was placed on the temperature gradients caused by local heating of the disc. The hysteresis loops for multiple braking process were shown. The possibilities of the application of the well-known hypotheses of fatigue in the disc brakes were discussed. The accuracy of assumptions of parabolic distribution of the heat flux densities of regular shapes of hot spots was verified. Applying the temperature boundary condition on the friction surfaces of the disc obtained from thermography measurements, the temperature fields in the disc were calculated numerically.

The thermomechanical macrostructural model of a disc brake of a high-speed rail (TGV) was developed in (Dufrenoy, 2004). The calculations were performed based on the algorithm incorporating varying during braking process the topography of the friction surfaces of the pads (three-dimensional model) and the disc (two or three-dimensional model), wear of the pad, temperature-dependent physical and mechanical properties of materials of the pad and the disc. The uncoupled iterative algorithm was used, according to which, the heat flux partition was determined based on the pressure distribution under static load and taking into account the thermal resistance. Then wear was determined in order to estimate the change in the volume and the topography of the friction surface of the pad, which in turn had an influence on the pressure distributions of the deformable bodies in the next step of mechanical analysis. The process was repeated in cycles. The

changes in the transient temperature fields of the pad and the disc in the radial direction were determined. The obtained outcomes were compared with the experimental results carried out using thermography techniques and thermocouples.

The problem of the crack initiation and growth in the rail wheels subjected to cyclic thermal loads due to heating and cooling during braking were examined in article (Rossmanith et al., 2006). A mechanism of fracture based on the extensive analysis of the variability of distributions of stress-temperature during braking involving multiple braking to stop, the subsequent cooling, and acceleration to the initial speed of the disc, starting another cycle was studied. The properties of materials (Young's modulus, thermal expansion coefficient and the yield strength) were dependent on the temperature. The convective heat transfer as well as the thermal radiation were included. The heat conduction was restricted to the wheel – the pads in the total energy balance were neglected. The pressure distribution in the heating area depended on the current thermal state of the disc. In order to analyse the actual conditions (real braking process), the multiple braking application was simulated. The one brake application was considered as a single load cycle. Based on the obtained outcomes, it was concluded that the residual stresses resulting from the exceeding of the yield strength, are tensile stress and their values slightly decrease from the inner to the outer surface. To analyse the mechanism of initiation and growth of cracks authors introduced the simplifying assumptions. The crack was modelled as a semi-circular of radius *a*, which retained its shape in the process of propagation. The second assumption was related to the stress field and the volume of the crack.

Finite element analysis of temperature and stress distributions based on the contact thermomechanical FE model of the pad-disc brake system was carried out in article by Scieszka and Zolnierz (2007a, 2007b). The dependencies of the coefficient of friction on the relative sliding velocity and the temperature for the mine winder disc brake using infrared techniques were determined. The results of numerical calculations in the form of transient temperature fields were verified experimentally based on the infrared measurements. The phenomenon of thermoelastic instability was analysed. A braking process was simulated and the formation of hot spots on the working surface of the disc was visualized. The concept of critical speed of the initiation of thermoelastic instability phenomenon was introduced. An attempted was made to establish a method for determining the critical speed based on the developed three-dimensional FE thermomechanical contact model. At the first stage the authors proposed the criterion of 10% of the temperature difference on the opposite sides of the disc to the initiation of the phenomenon of thermoelastic instability according to (Choi and Lee 2004) and applied to the developed numerical model of the disc brake. Based on the obtained results the dependencies of the critical speed on the thermophysical properties material of the disc and its thickness were shown. It was observed that the greatest impact on the critical speed had the coefficient of thermal expansion of the material of the disc. The decrease in the coefficient of thermal expansion as well as the Young's modulus significantly expanded the range of the critical speed of the initiation of TEI. Also, increasing the thickness of the disc led to an increase in the critical speed. It was observed that despite the initiation of the thermoelastic instability, the brake operation was not disturbed. Therefore a new criterion related to the structural restrictions, namely the size of the gap between the disc and pad was formulated (a criterion for permissible lateral run-out). The critical speed above which the axial displacement

exceeded the acceptable range was determined. In the next stage, the effect of the division of the disc on the stress was tested. For this purpose a comparative analysis of equivalent stress of sectional and solid disc during emergency braking was carried out. The distributions of the equivalent stress in the specific braking time were shown. The calculations revealed that the solid disc is subjected to the presence of the equivalent stress exceeding the yield strength of the tested steel type. Whereas this problem did not occur in the sectional disc.

The contact thermomechanical three-dimensional finite element model to study the transient temperature and the stress fields in the pad-disc brake system was developed in article by Gao et al. (2007). The temperature and the stress changes at selected radial positions on the working surface of the disc were determined. A clear relationship between the temperature evolution and the change in equivalent stress was observed. The highest values of both of these quantities were obtained in approximately half of the braking time. The maximum normal stress occurred for circumferential component (compression). Slightly lower values were reached for a radial stress component. The sign of the radial and circumferential stress in the area near the outer cylindrical surface tended to change at the end of braking. This effect was particularly marked in the case of radial stress.

The coupled thermomechanical problem for a multi-disc dry clutch made of a composite material was carried out in (Zhao et al., 2008). The transient temperature and the stress tensor components changes for a single clutch engagement and the disengagement using an axisymmetric contact FE model were calculated. The results were obtained for the operation of the clutch and after the disconnection of the discs. The highest stress values were reached for the circumferential component (compressive stress) in approximately half of the operation time of the clutch.

The identification of the nature and cause of damage of the cast-iron discs of a truck subjected to high thermal loads using the technique of macro-fractography, optical and scanning electron microscopes in article (Bagnoli et al., 2009). With a view to eliminating one of the cause of cracking originated from defects in material of the studied material (cast iron), based on the measurements, the chemical composition, structure and hardness were verified. It was found that the propagation of radial macro-cracks in the heating area of semi-elliptic shape extends from the surface into the disc as a result of thermal fatigue mechanism. Then the changes in temperature distributions and equivalent Huber-Mises stress in the disc were calculated numerically using FEM. The calculations confirmed the presence of high temperature gradients in the area of the friction surface resulting in a local increase in the Huber-Mises stress.

The transient uncoupled temperature field and the thermal stresses were analysed in the article (Collignon et al., 2013). An attempt was made to determine the type and size of the thermo-mechanical load of components of the friction pair causing damage of the discs in the form of radial macro-cracks. On a developed for this purpose bench, a series of tests of the brake system according to an algorithm established on the assumption that the mechanical energy is entirely transformed into heat during braking. A new unused disc was loaded recording changes in temperature field by using an infrared camera and thermocouples. The numerical calculations were carried out using ANSYS FE numerical package. In the model comprising 1/20 of the ventilated disc, the temperature-dependent thermophysical properties of the material were taken into account. Moreover, on the surfaces free from heating the heat exchange through thermal radiation and

convective cooling at the different values of heat transfer coefficient depending on the position took place. Elastic-plastic model was adopted for the material (cast iron) introducing beyond the established within the software the same behaviour in compression and tension, two different criteria: Huber-Mises (compression) and Rankine (tension). Temperature fields in different moments during the analysed braking process at the chosen time step were analysed. On the basis of the obtained temperature distributions thermal stresses were calculated. Slight differences in temperature changes calculated numerically and recorded during the experimental tests were justified by possible different cooling conditions of the brake system.

The comparative analysis of stress distribution in a ventilated disc with uniform and non-uniform distribution of the contact pressure was performed in article (Kim et al., 2008). The pressure distribution was determined numerically based on the contact three-dimensional computational model incorporating exclusively mechanical interactions. Based on calculations it was shown that the pressure distribution was relatively uniform, however the highest value of the pressure in the radial direction was obtained in the centre of the rubbing path. With the distance to both the outer and the inner cylindrical surface of the disc, the pressure decreased. The resulting pressure distribution was then treated as a boundary condition in the thermal analysis. A simulation of a single braking process at constant deceleration was carried out. Analysis of stress fields in the case of non-uniform pressure distribution revealed the highest values of equivalent Huber-Mises stress on the friction surface near the centre of the rubbing path. If the pressure distribution was uniform, the maximum stress values were slightly higher (about 3%), and occurred near the inner circular edge of the disc on the friction surface.

A strength of disc brakes with a circular holes (joints) made of a composite carbon/carbon quasi-isotropic material were studied in article (Lim et al., 2008). The specimens with different angles regarding the reference axis were extracted from a real disc brake and their properties were derived from the tension, compression and shear tests. The failure criterion was formulated on the basis of the maximum stress theory. The failure loads were measured and applied to the three-dimensional model of a specimen with a hole. The numerical calculations were performed using MSC Marc software.

A relatively low number of braking cycles with a significant deceleration may cause a strain leading to plastic stress. An attempt to determine the number of cycles to failure based on the Coffin-Manson criterion used under low cycle fatigue loads was taken in article (Mackin et al, 2002). In the first stage, the forces acting on the elements of the friction pair during braking were determined. Then the braking conditions (braking time, the initial velocity, the number of brake applications) that may lead to the development of the thermal cracks were set. The numerical calculations to obtain the temperature distributions were carried out using FEM. Based on the calculated radial, circumferential and equivalent Huber-Mises stress as well as the Coffin-Manson formula the number of cycles to the appearance of damage of the brake disc was predicted. The values obtained from the calculations were higher about 11% compared to the data evaluated from experimental studies. Moreover, the maximum equivalent stresses exceeded the yield strength of the tested material near the hub. According to (Mackin et al., 2002) during braking compressive stresses prevail, while during cooling the tensile residual circumferential stress are dominant. The repeating cycle of the successive states of stress comprises a mechanism of a fatigue leading to a failure.

Based on observation with a scanning electron microscope three types of structures of the material were identified defining the successive steps of cracks growth in the disc brake in article (Sakamoto and Hirakawa, 2005). The impact of the chemical composition to improve the properties of the materials used for the brake discs was discussed. This was followed by FE numerical simulation of a braking process in the axisymmetric arrangement. The results were compared with the strain measurements. Based on the calculated stress distribution, the stress intensity factors were determined. In addition, the stress intensity factors were determined from measurements carried out on CT (compact tension) specimens. The heating cycle goes from the compressive stress at the time of reaching the maximum temperature then the residual tensile stress at the decrease in temperature to the room temperature. Next, a discussion of possibilities to improve the breaking strength by changing the chemical composition of the material was carried out. Pointed out the possibility of using different methods, such as Coffin, Manson, Northcott, Blauela and other thermal fatigue tests, however, none of the methods, as stated do not provide for changes in many factors occurring during braking and require simplification.

The stress fields in a ventilated and a solid type of the brake discs using the developed fully three-dimensional FE models were studied in article by Yildiz and Duzgun (2010). The analysis was performed taking into account only the mechanical loads without the generation of heat due to friction. Three different types of ventilated and drilled brake discs different in the arrangement and shape of the holes and a solid disc with a uniform distribution of clamping force were examined. Then the modification of the distribution of force on the pad, in order to determine the most favourable from the point of view of minimizing the equivalent stress on the brake disc was proposed. It was observed that the higher stresses were induced in a ventilated brake disc compared to the solid disc.

3. CONCLUSIONS

The paper presents the finite elements analyses of the thermal stresses in disc brakes and clutches. The calculations were performed using the axisymmetric and fully three-dimensional computational models. The following conclusions on the basis of the analysed studies have been drawn:

- the contact pressure distribution (either assumed as constant in thermal analysis or calculated in contact thermomechanical analysis) affects the temperature field on the friction surfaces and changes the location of the highest equivalent Huber-Mises stress;
- the circumferential and radial stress components calculated both using the contact thermomechanical models as well as when considering two bodies separately, are dominant normal stress components and are approximately equal;
- the axial stress component is frequently neglected in the analysis of the results due to its relatively small value;
- in order to minimize the radial and being its result, the circumferential stress component, the discrepancy in the radial distribution of the heat flux density should be minimized;
- the problem of the fatigue failure of the disc brakes is not entirely explored and leaves some open questions due to the difficulty in employing directly the fatigue criterions to the brake discs.

REFERENCES

1. **Bagnoli F., Dolce F., Bernabei M.** (2009), Thermal fatigue cracks of fire fighting vehicles gray iron brake discs, *Engineering Failure Analysis*, Vol. 16, 152-163.
2. **Balakin V.A.**, **Sergienko V.P.** (1999) *Heat calculations of brakes and friction units*, MPRI of NASB, Gomel, (in Russian).
3. **Chichinadze A.V.** (1967), *Calculation and investigation of external friction during braking*, Nauka, Moscow, (in Russian).
4. **Chichinadze A.V., Braun E.D., Ginsburg A.G., Ignat'eva E.V.** (1979), *Calculation, test and selection of frictional couples*, Nauka, Moscow, (in Russian).
5. **Choi J-H., Lee I.** (2003), Transient thermoelastic analysis of disk brakes in frictional contact, *Journal of Thermal Stresses*, Vol. 26, No. 3, 223-244.
6. **Choi J-H., Lee I.** (2004), Finite element analysis of transient thermoelastic behaviors in disk brakes, *Wear*, Vol. 257, 47-58.
7. **Collignon M., Cristol A-L., Dufrénoy P., Desplanques Y., Balloy D.** (2013), Failure of truck brake discs: A coupled numerical–experimental approach to identifying critical thermomechanical loadings, *Tribology International*, Vol. 59, 114-120.
8. **Dufrénoy P.** (2004), Two-/three-dimensional hybrid model of the thermomechanical behaviour of disc brakes, *Proceedings of the Institution of Mechanical Engineers, Part F: Journal of Rail and Rapid Transit*, Vol. 218, No. 1, 17-30.
9. **Dufrénoy P., Weichert D.** (2003), A thermomechanical model for the analysis of disc brake fracture mechanisms, *Journal of Thermal Stresses*, Vol. 26, 815-828.
10. **Evtushenko O.O., Ivanyk E.H., Horbachova N.V.** (2000), Analytic methods for thermal calculation of brakes (review), *Materials Science*, Vol. 36, No. 6, pp. 857-862.
11. **Gao C.H., Huang J.M., Lin X.Z., Tang X.S.** (2007), Stress analysis of thermal fatigue fracture of brake disks based on thermomechanical coupling, *ASME Journal of Tribology*, Vol. 129, No. 3, 536-543.
12. **Kim D.-J., Lee Y.-M., Park J.-S., Seok C.-S.** (2008), Thermal stress analysis for a disk brake of railway vehicles with consideration of the pressure distribution on a frictional surface, *Materials Science and Engineering: A*, Vol. 483-484, 456-459.
13. **Lim D.-W., Kim T.-H., Choi J.-H., Kweon J.-H., Park H.-S.** (2008), A study of the strength of carbon-carbon brake disks for automotive applications, *Composite Structures*, Vol. 86, No. 1-3, 101-106.
14. **Mackin T.J., Noe S.C., Ball K.J., Bedell B.C., Bim-Merle D.P., Bingaman M.C., Bomleny D.M., Chemlir G.J., Clayton D.B., Evans H.A., Gau R., Hart J.L., Karney J.S., Kiple B.P., Kaluga R.C., Kung P., Law A.K., Lim D., Merema R.C., Miller B.M., Miller T.R., Nielson T.J., O'Shea T.M., Olson M.T., Padilla H.A., Penner B.W., Penny C., Peterson R.P., Polidoro V.C., Raghu A., Resor B.R., Robinson B.J., Schambach D., Snyder B.D., Tom E., Tschantz R.R., Walker B.M., Wasielewski K.E., Webb T.R., Wise S.A., Yang R.S., Zimmerman R.S.** (2002), Thermal cracking in disc brakes, *Engineering Failure Analysis*, Vol. 9, 63-76.
15. **Matysiak S.J., Yevtushenko A.A.** (2001) On heating problems of friction, *Journal of Theoretical and Applied Mechanics*, Vol. 3, No. 39, 577-588.
16. **Rossmanith H.P., Loibnegger F., Huber R.** (2006), Thermomechanical fatigue fracture due to repeated braking of railway wheels, *Materials Science*, Vol. 42, No. 4, 40-48.
17. **Sakamoto H., Hirakawa K.** (2005), Fracture analysis and material improvement of brake discs, *JSME International Journal Series A*, Vol. 48, No. 4, 458-464.
18. **Scieszka S., Zolnierz M.** (2007a), The effect of the mine winder disc brake's design feature on its thermoelastic instability. Part I. Set-up for finite element modelling and numerical model verification, *Problems of Machines Operation and Maintenance*, Vol. 42, No. 3, 111-124.
19. **Scieszka S., Zolnierz M.** (2007b), The effect of the mine winder disc brake's design feature on its thermoelastic instability. Part II. Finite element simulation, *Problems of Machines Operation and Maintenance*, Vol. 42, No. 4, 183-193.
20. **Yevtushenko A.A., Grzes P.** (2010), The FEM-modeling of the frictional heating phenomenon in the pad/disc tribosystem (a review), *Numerical Heat Transfer, Part A: Applications*, Vol. 58, No. 3, 207-226.
21. **Yevtushenko A.A., Grzes P.** (2014), *FEM-modeling of frictional heating during braking*, Encyclopedia of Thermal Stresses, Vol. 4, Springer Science+Business Media Dordrecht, DOI 10.1007/978-94-007-2739-7.
22. **Yildiz Y., Duzgun M.** (2010), Stress analysis of ventilated brake discs using the finite element method, *International Journal of Automotive Technology*, Vol. 11, No. 1, 133-138.
23. **Zagrodzki P.** (1985), Numerical analysis of temperature fields and thermal stresses in the friction discs of a multidisc wet clutch, *Wear*, Vol. 101, 255-271.
24. **Zagrodzki P.** (1990), Analysis of thermomechanical phenomena in multidisc clutches and brakes, *Wear*, Vol. 140, No. 2, 291-308.
25. **Zhao S., Hilmas G.E., Dharani L.R.** (2008), Behavior of a composite multidisk clutch subjected to mechanical and frictionally excited thermal load, *Wear*, Vol. 264, 1059-1068.

DYNAMIC TESTING OF COPPER MATERIAL – NUMERICAL APPROACH

Paweł BARANOWSKI[*], **Jerzy MAŁACHOWSKI**[*], **Łukasz MAZURKIEWICZ**[*], **Krzysztof DAMAZIAK**[*]

[*]Faculty of Mechanical Engineering, Department of Mechanics and Applied Computer Science, Military University of Technology,
ul. Gen. Kaliskiego 2, 00-908 Warszawa, Poland

pbaranowski@wat.edu.pl, jerzy.malachowski@wat.edu.pl, lmazurkiewicz@wat.edu.pl, kdamaziak@wat.edu.pl

Abstract: Split Hopkinson pressure bar (SHPB) is one of the most important and recognisable apparatus used for characterizing the dynamic behaviour of various materials. Incident pulse generated one the incident bar usually have a rectangular shape, which is proper for some materials but for others is not. Therefore, several methods of shaping the incident pulse are used for obtaining constant strain rate conditions during tests. Very often pulse shapers made of copper or similar material are implemented due to its softness properties. In this paper such material was investigated using the FE model of SHPB. Its mechanical behaviour was characterised with and without copper disc between the striker and incident bar. Numerical simulations were carried out using explicit LS-DYNA code. Two different methods were used for modelling the copper sample: typical finite Lagrangian elements and meshless Smoothed Particle Hydrodynamics (SPH) method. As a result of two techniques used axial stress-strain characteristics were compared for three different striker's velocity with an influence of the copper pulse shaper taking into account. Finally, FE and SPH method was compared with taking into consideration: the efficiency, computer memory and power requirements, complexity of methods and time of simulation.

Key words: Copper, Compression, FE Analysis, SHPB

1. INTRODUCTION

Hopkinson bar with all its former and actual configurations is widely used to determine material properties at high strain rates (Ellwood et al., 1982; Hopkins, 1872). Such investigations, however, are exposed to longitudinal dispersion produced from indirect effects such as lateral impact of the striker. Also, Pochhammer-Chree oscillations (Davies, 1948; Graff, 2004) can occur, which affect the mechanical behaviour of tested sample. Therefore, several methods of shaping the pulse on the incident bar are used, e.g.: by inserting a preloading bar ((Ellwood et al., 1982;Foley et al., 2010; Franz et al., 1984) or using a pulse shaper (Ellwood et al., 1982; Foley et al., 2010; Naghdabadia et al., 2012), which very often is made of copper or similar material (due to its softness properties). In addition to the previous methods a shape of the striker is modified (Cloete et al., 2008; Li et al., 2005; Seng, 2003), which in fact was the investigation object of the previous authors' paper (Baranowski et al., 2013).

It is well known that for different test conditions it is recommended to adjust thickness and diameter of the pulse shaper (Foley et al., 2010). Also, work-hardening or brittle materials need different thickness-length proportion of the disc. Moreover, as presented by other authors (Klepaczko, 2007; Jankowiak et al., 2011), such effect like friction, apart from others, influences the proper estimation of material properties using SHPB, due to the overstress state in the specimen. Authors are aware of such foundations but the main purpose of the paper is to present the possibility of two different numerical techniques for characterising a mechanical behaviour of material with and without copper disc between the striker and incident bar. In experimental conditions the use of the pulse shaper is a simple procedure, but for obtaining a constant strain rate conditions during tests many attempts have to be conducted. This can be easily achieved using numerical methods, more particularly finite element method. Also, initial tests for calibrating the actual SHPB set-up can be performed, even using literature material properties.

In the paper numerical simulations were carried out using explicit LS-DYNA code. Two different methods were used for modelling the copper sample: typical finite Lagrangian elements and meshless Smoothed Particle Hydrodynamics (SPH) method, which is considered by authors as novel in terms of SHPB pulse shaper modelling. Subsequently, mechanical characteristics of the material (stress vs. strain curves) were compared for both methods and, additionally, for three different striker's velocities with an influence of the copper pulse shaper taking into account. Finally, FE and SPH method was compared with taking into consideration: the efficiency, computer memory and power requirements, complexity of methods and time of simulation.

Presented study is the part of wider investigations which are pointed on finding the optimal shape of incident pulse for a specific type of material (brittle, ductile or soft). In these studies copper material plays a major role (is used for the pulse disc), therefore our attention is also focused on the proper material constitutive material modelling.

2. SHPB TESTING – OPERATING PRINCIPLE

A typical SHPB test starts with launching a striker using highly compressed gas , which consequently impacts the incident bar. This generates the elastic wave (incident wave) which travels through the bar and then, due to the difference between mechanical impedances of bar and specimen materials, part of the pulse comes back (reflected wave), whereas the rest of it is transmitted through the tested specimen. Next, the specimen is compressed and the wave travels to the transmission bar and generates a so called transmitted wave (Fig. 1).
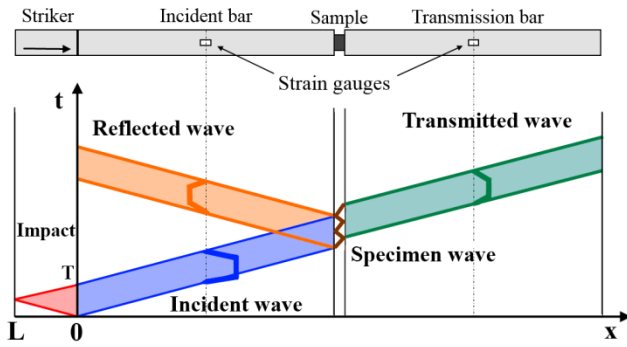
Fig. 1. Wave history route in SHPB

Based on the above Figure, in addition to the literature (Ellwood et al., 1982; Hopkins, 1872; Davies, 1948), it can be stated that pulse duration time increases proportionally with striker's length:

$$T = \frac{2L}{c_p} \qquad (1)$$

where: T – impulse duration time, L – striker length and c_p – elastic wave propagation velocity in a bar material

All three signals are sensed by strain gauges which are placed in the middle of the bars. Then the relationship between three pulses (transmitted ε_T, incident ε_I and reflected ε_R) can be described as follows [1,2,5]:

$$\varepsilon_T(t) = \varepsilon_I(t) - \varepsilon_R(t) \qquad (2)$$

According to the conventional one-dimensional SHPB theory, the nominal strain rate, strain and nominal stress in the specimen are given by Ellwood et al. (1982); Hopkins (1872) and Foley et al. (2010):

$$\dot{\varepsilon}(t) = -2\frac{C_0}{L_S}\varepsilon_R(t) \qquad (3)$$

$$\varepsilon(t) = -2\frac{C_0}{L_S}\int_o^t \varepsilon_R(t)dt \qquad (4)$$

$$\sigma(t) = -\frac{ES_{p0}}{S_{pr}}\varepsilon_T(t) \qquad (5)$$

where C_o – wave velocity in incident bar, L_s – specimen length, E – Young modulus, S_{po} – cross section area of transmitted bar, S_{pr} – cross section area of specimen, $\varepsilon_R(t)$ – reflected strain history, $\varepsilon_T(t)$ – transmitted strain history.

3. NUMERICAL SHPB TESTING

The FE model of the SHPB was based on the actual device (Fig. 2). It consists of gas gun, striker (d=20 mm, L=150 mm), copper pulse and shaper (both: d=5 mm, H=3 mm), incident bar and transmission bar (both: d=20 mm, L=2000 mm).

Numerical analyses were performed using explicit LS-Dyna solver with central difference scheme and with the implementation of modified equation of motion time integration (Klepaczko, 2007). In the carried out analyses the stability of computations was guaranteed by Courant-Friedrichs-Lewy (CFL) condition, which can be described as follows [14]:

$$C = \frac{u_x\Delta t}{\Delta x} + \frac{u_y\Delta t}{\Delta y} + \frac{u_z\Delta t}{\Delta z} \leq C_{max} \qquad (6)$$

where: u_x, u_y, u_z – velocities, Δt – time step, Δx, Δy, Δz – length intervals, C_{max} – varies with the method used (in presented investigations it was set to C_{max}=0.66, which is recommended for strongly dynamic phenomena).
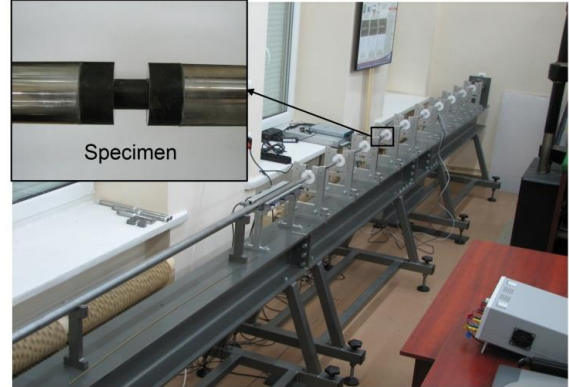

Fig. 2. Split Hopkinson Pressure Bar device used for the FE model

With the usage of finite element method the numerical model of SHPB apparatus was developed and validated (Baranowski et al., 2013). From the carried out simulations the incident impulse (axial stress) was obtained which was taken from the incident bar element from the same place, where strain gauge was glued. This choice of this particular element was dictated by the fact, that there were no differences between the stress values of the elements along the cross section area, whereas at the impact side of the bar these differences were noticed (Saint-Venant's principle was fully confirmed (Saint-Venant, 1855)). By comparing both pulses (experimental and numerical) good overall correlation was noticed: time intervals between incident and reflected impulses as well as stress values were approximately identical (Fig. 3)
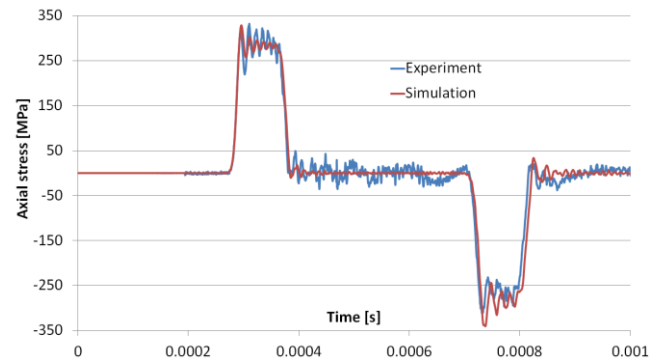

Fig. 3. Numerical and experimental impulse comparison in SHPB validation

In order to simplify and shorten computational time, symmetry of the problem was assumed and only quarter of the 3D model was taken into consideration. It is known that axially-symmetric model is less computationally expensive but chosen three-dimensional model in subsequent investigations will give the possibility to study additional effects, like dispersion effects or misalignment impacts occurring in the SHPB.

As mentioned before, copper sample was modelled using FE

and SPH mesh and for analyses with shaped incident pulse, the copper disc was described only using Lagrangian elements (Figs. 4-7). Also, dimensions of the sample were the same as in the pulse shaper (5 mm diameter, 3 mm long).

Initial velocity conditions were applied on the whole striker volume (all nodes), which values were as follows:

- v_1= 30 m/s,
- v_2= 25 m/s,
- v_3= 20 m/s.

At this point it should be also mentioned that proper contact definition is extremely important in numerical modelling of such strong dynamic phenomenon. More particular, it directly influences obtained incident impulse shape, which in fact, have an impact on the behaviour of a material sample. Thus, for the purpose of simulations surface to surface and nodes to surface contact algorithm with soft constraint option was applied, which guaranteed penetration not to occur (Hallquist, 2003). Generally, LS-DYNA, apart from the other, uses so called penalty function (Hallquist, 2003; Vulovic et al., 2007; Baranowski et al., 2012). Then, a fictional elastic element stiffness is added to the basic dynamic FE equilibrium thanks to the following energetic part:

$$\pi(u) = \kappa[(Bu - g_N)^T(Bu - g_N)] \tag{7}$$

where: u – global displacement vector, κ – fictional elastic element stiffness, B – matrix of boundary conditions kinematic, g_N – initial vector between the node and segment in contact.

Material properties for the bars were described with a typical Hooke's law elastic constitutive model (with literature steel data) since the incident and striker bar remain elastic during tests (Ellwood et al., 1982).

It is well known that the maximum stresses rises with strain rates, which also influence yielding of a material (Chmielewski at al., 2004; Janiszewski, 2012) and in presented studies copper sample, as well as the shaper, deforms in dynamic conditions where strain rate plays significant role (in the material the viscous effects are initiated). Thus, in both cases of sample modelling (FE and SPH) the Johnson-Cook constitutive material model was utilized (Tab. 1). It provides a prediction of flow stress σ_{flow} for arge strains and high strain rates, where its dependence on strain rate is linear in semi logarithmic scale (Hallquist, 2003; Johnson and Cook, 1983):

$$\sigma_{flow} = \left[A + B(\varepsilon^p)^n\right]\left(1 + C\,ln\,\dot{\varepsilon}_*^p\right) \tag{8}$$

where A, B, C, n – material constants, ε^p – effective plastic strain, $\dot{\varepsilon}_*^p$ – effective plastic strain rate.

The Grüneisen equation of state was used for describing the pressure-volume relationship of the copper sample and pulse shaper with constants taken from literature (Steinberg, 1906) (Tab. 2). It defines the pressure in compressed materials as (Hallquist, 2003):

$$p = \frac{\rho_0 C^2 \mu \left[1 + \left(1 - \frac{\gamma_0}{2}\right)\mu - \frac{a}{2}\mu^2\right]}{\left[1 - (S_1-1)\mu - S_2\frac{\mu^2}{\mu+1} - S_3\frac{\mu^3}{(\mu+1)^2}\right]^2} + (\gamma_0 + a\mu)E \tag{9}$$

and for expanded materials as (Hallquist, 2003):

$$p = \rho_0 C^2 \mu + (\gamma_0 + a\mu)E \tag{10}$$

where C – intercept of the v_s-v_p curve (shock wave velocity vs. particle velocity), S_1, S_2, S_3 – coefficients of the slope of v_s-v_p curve, γ_0 – Grüneisen gamma, a – first order volume correction to γ_0, and $\mu = \rho/\rho_0 - 1$.

Tab. 1. Properties of copper for J-C model adopted in analyses [20]

A [MPa]	B [MPa]	N	C	ρ [kg/m3]	E [GPa]	υ
92	292	0.310	0.025	1.09	115	0.33

Tab. 2. Constants required for input in the Grüneisen EOS [21]

C_0 [m/s]	S_1	S_2	S_3	γ_0
3933	1.5	0	0	1.99

3.1. FE copper sample modelling

In the FE modelling of copper sample fully integrated hexagonal elements were used (HEX8). Also, symmetry conditions were applied and only quarter of the 3D model was taken into consideration. Two analyses were carried out: with and without the copper shaper (Fig. 4 and Fig. 5). For modelling the sample as well as pulse shaper large aspect ratio elements were chosen which guaranteed the accuracy and stability of computations throughout analysis in which the copper becomes largely compressed.
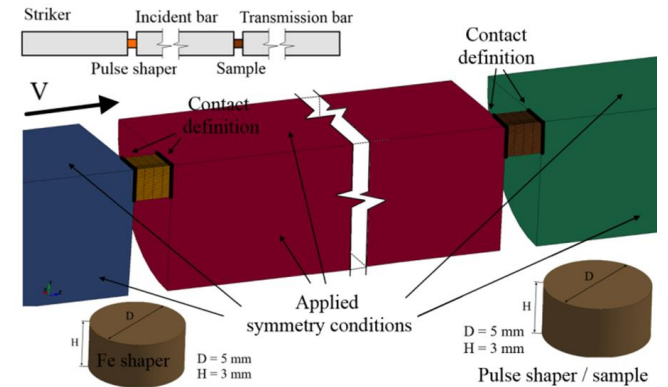

Fig. 4. Initial-boundary conditions applied for FE analysis with shaper
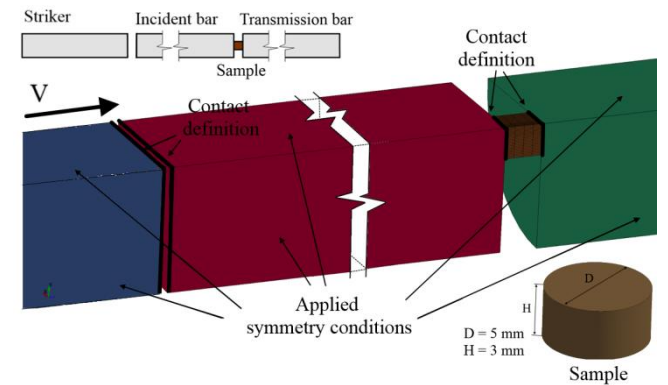

Fig. 5. Initial-boundary conditions applied for FE analysis without shaper

Interaction between striker, bars, copper disc and sample was described by the surface to surface contact procedure and no friction was assumed, which in actual conditions is reduced

as much as possible by adding a lubricate. As stated before three velocities were used, which resulted in different strain rates during tests.

3.2. SPH copper sample modelling

Smoothed Particles Hydrodynamics is a mesh-free particle method with Lagrangian nature, where computational information including mass and velocity are carried with particles. This method is mainly used for simulating fluid flows and large deformations of structures. The main difference between classical methods and SPH is the absence of a grid. Therefore, those particles are the framework of the region within the governing equations are solved (Hallquist, 2003). SPH method uses the concept of kernel and particle approximation as follows (Hallquist, 2003):

$$\prod^k f(x) = \int f(y)W(x-y,h)dy \tag{11}$$

where W – kernel function, which is defined using the function θ by the relation:

$$W(x,h) = \frac{1}{h(x)^d}\theta(x) \tag{12}$$

where d is the number of space dimensions and h is the so-called smoothing length which varies in time and in space.

SPH model of the sample (with the same dimensions as previous) consisted of 468 elements with the average distance between particles 0.035 mm (Fig. 6, 7). It should be noted that authors used a "cylinder" method for the sample modelling. This choice was dictated by the fact, that is such strong-dynamic phenomena one of the main conditions for proper analysis is that the SPH mesh must be as regular as possible and must not contain too large variations (Hallquist, 2003).

In this case the interaction between SPH sample and bars was described by the nodes to surface contact procedure. Also, no friction was assumed and quarter of the model was applied. Additionally, recommended values of bulk viscosity for SPH formulation were used in presented investigations, i.e. Q1 = 1.5 and Q2 = 1.0.

Identical to the FE case three velocities were used and two analyses were carried out: with and without the copper shaper (Fig. 6 and Fig. 7).
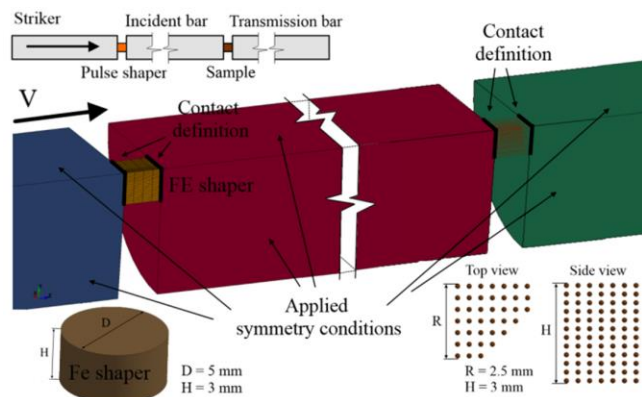

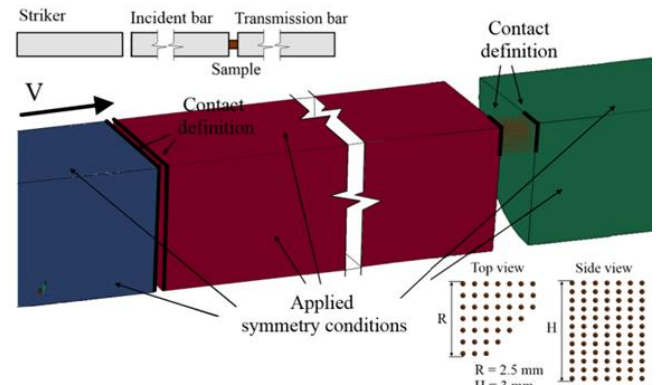**Fig. 6.** Initial-boundary conditions applied for SPH analysis with shaper

Fig. 7. Initial-boundary conditions for SPH analysis without shaper

4. RESULTS

From the performed simulations axial stress versus axial strain characteristics were obtained for all cases. In order to create curves an average value of all elements modelling specimen was taken into consideration. In Fig. 9, 12 copper sample stress-strain characteristic is presented for analyses (FE and SPH) with the shaper for three aforementioned different velocities. In Fig. 10, 13 the same result is presented but without impulse shaping, also for FE and SPH analysis.

For the FE analyses with shaper maximum axial stress achieved for v_1= 30 m/s, v_2= 25 m/s and v_3= 20 m/s were approximately 430 MPa, 406 MPa and 374 MPa, respectively. In the similar analysis (FE sample) but without shaper these values were as follows: 447 MPa, 418 MPa and 393 MPa. Also, one can see that by using the pulse shaper the incident pulse, which directly affects the material behaviour during compression, changes: its rise time increases and no oscillations can be noticed (Naghda-badia et al., 2012; Baranowski et al., 2013) (Fig. 8). On the other hand the decrease of the maximum axial stress in the specimen is clearly visible. Bearing this in mind and the fact that other authors obtained similar results (Naghdabadia et al., 2012; Jan-iszewski, 2012; Sankaye, 2011; Wu and Gorham, 1997) our curves can be regarded as appropriate and reasonable.

In the SPH analyses, also, similar results were obtained as in the FE case. Inserting the copper pulse shaper caused that the specimen deformation was reduced, which resulted in decrease of maximum axial stress and axial strain. Maximum axial stress obtained for those analyses were: 400 MPa, 384 MPa, 357 MPa with shaper and 410 MPa, 397 MPa and 376 MPa without the shaper. Figs. 11, 14 show the comparison graphs for each method.
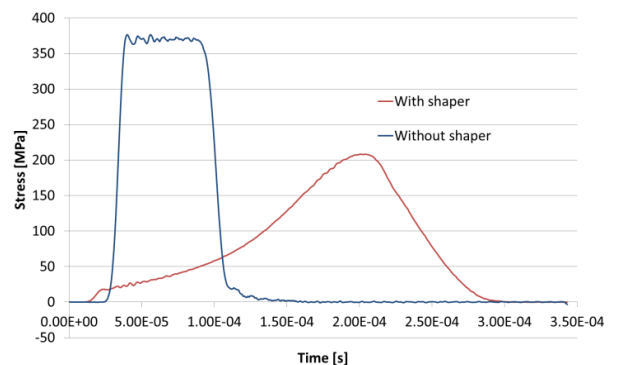

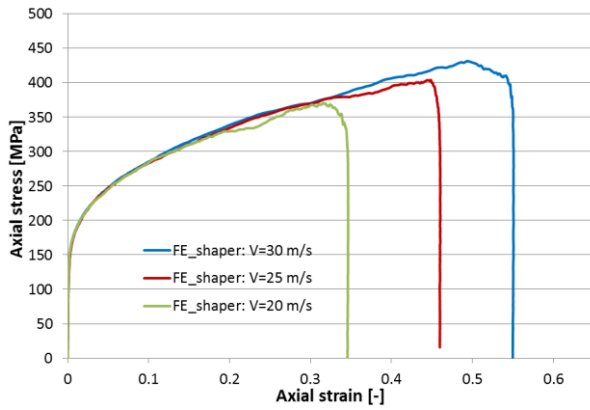**Fig. 8.** Exampary incident pulse obtained in the simulation with and without shaper

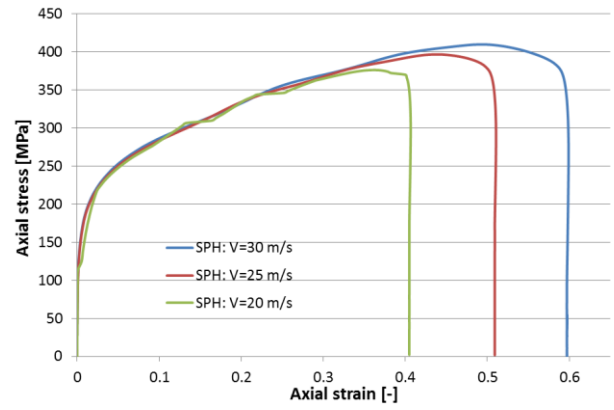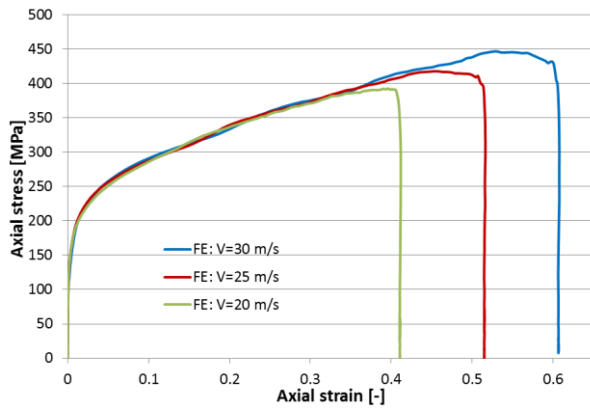**Fig. 9.** Stress-strain characteristic for the FE modelling with shaper

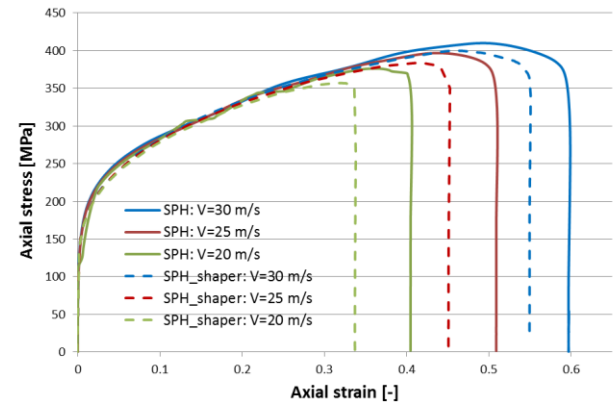**Fig. 10.** Stress-strain characteristic for the FE modelling without shaper
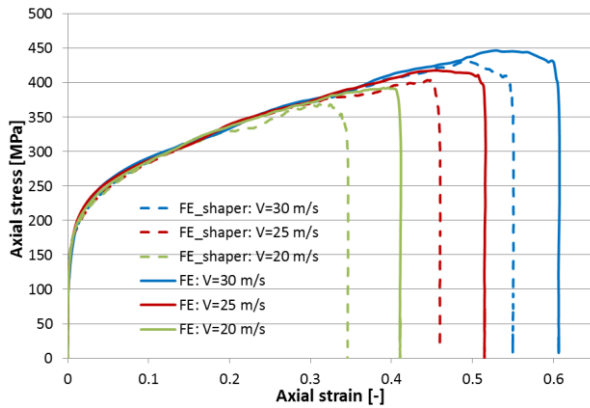

Fig. 11. Stress-strain characteristics comparison for the FE modelling

Fig. 12. Stress-strain characteristic for the SPH modelling with shaper
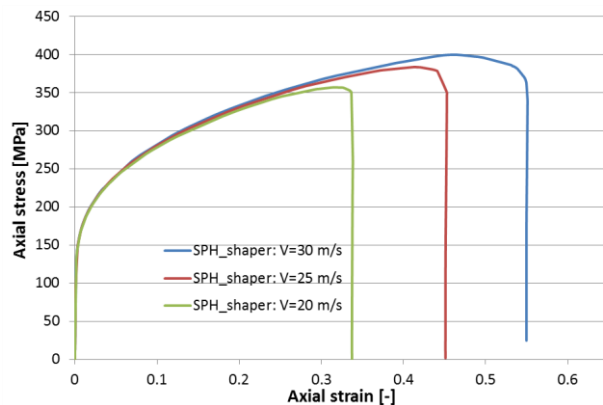

Fig. 13. Stress-strain characteristic for the SPH modelling without shaper

Fig. 14. Stress-strain characteristics comparison for the SPH modelling

4.1. FE and SPH method comparison

Figs. 15, 16 present both methods stress-strain curves for the same initial-boundary conditions. It is clearly seen that the stress and strain values obtained in SPH analyses are smaller than in FE modelling. It is caused by the fact that each element formulation handles deformation, and consequently, stresses in different way (Hallquist, 2003; Li and Liu, 2002). Differences (max stress values) between those two methods are listed in Tab.3.

It is worth to mention about the effectiveness of implemented methods (for the same termination time t_{end} = *0.0009 s* and for the same striker's velocity *v=30 m/s*). SPH formulation, due to the complex mathematical background, is much more computationally expensive – analyses were carried out for 104 min (without shaper) and 121 min (with shaper). In fact, it was also caused by the lower value of timestep, which is basically depended on the distances between particles (it was calculated as dt = *2.80e⁻⁹*). For the Lagrangian modelling the simulation (v=30 m/s) without shaper ended after 57 min, whereas with shaper after 73 min. In both cases timestep varied due to the large elements deformation as well as contact calculation: the approximate value equalled to dt = *9.72e⁻⁹*. The comparison graph is presented in Fig. 17. Also, as mentioned before, in order to perform simulations using SPH technique one of the main conditions for proper analysis is that the SPH mesh must be as regular as possible and must not contain too large variations. This indicated that there is a need to spend more time on developing a desired model.
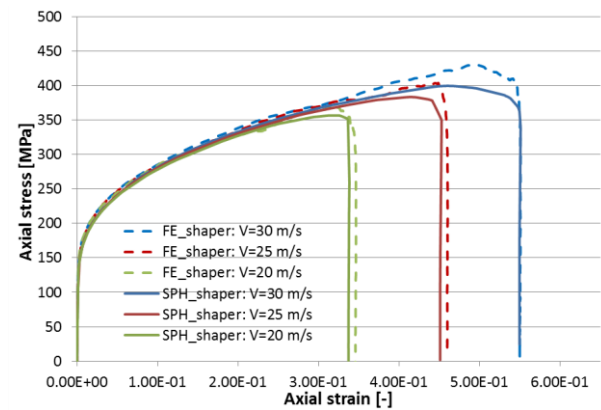
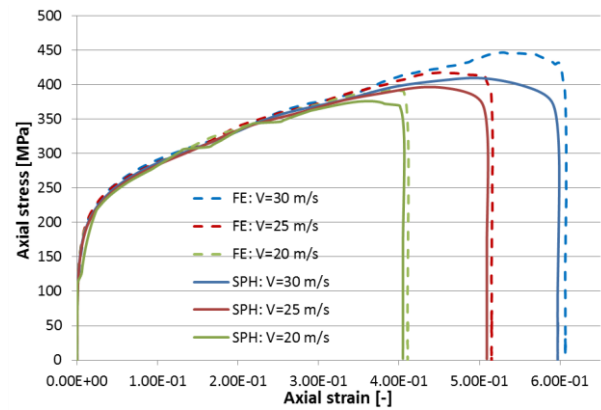**Fig. 15.** Stress-strain characteristics comparison for FE and SPH modelling (shaper)

Fig. 16. Stress-strain characteristics comparison for FE and SPH modelling (no shaper)

Tab. 3. Statistic data (axial maximum stress) of obtained results

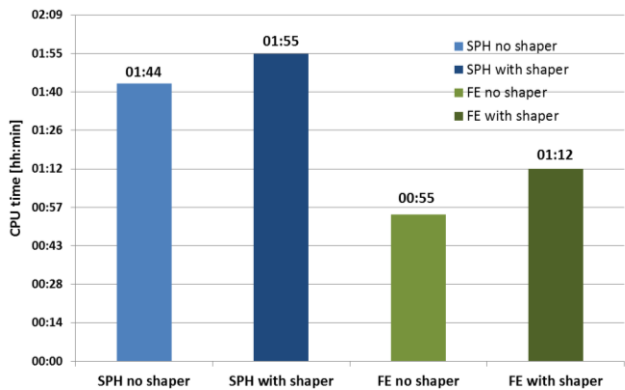|	Max. axial stress [MPa]			
	FE modelling		SPH modelling	
Impact velocity	Shaper	No shaper	Shaper	No shaper
30 m/s	430	447	400	410
25 m/s	406	418	383	397
20 m/s	374	393	357	376

Fig. 17. CPU time comparison for all cases

5. CONCLUSIONS

The paper shows the possibility of two different numerical techniques for characterising a mechanical behaviour of material with and without copper disc between the striker and incident bar. For this purpose two available methods in LS-Dyna software were implemented to model the sample: typical finite element formulation (Lagrangian) and SPH – one of the most popular from meshless methods.

From the carried out analyses stress-strain histories for copper sample were obtained and examined. Simulations with and without the shaper were performed and two aforementioned methods were taken into consideration. The influence of copper disc on obtained results was investigated as well as both methods were compared with each other. It was proved that stress-strain characteristics shapes for both techniques are similar to those presented in available literature (Naghdabadia et al., 2012; Janiszewski, 2012; Sankaye, 2011; Wu and Gorham, 1997). Although, it seems that SPH modelling gives underestimated stress values and this needs to be verified in subsequent analyses with experimental validation. Moreover, SPH formulation, due to the complex mathematical background, is much more computationally expensive. Also it seems that for such short-lasting simulations of SHPB, time needed to prepare model is disproportionate. Nevertheless, in FE modelling of copper sample as well as shaper a special care must be taken to choose a proper aspect ratio of elements (min 4). In addition to being largely compressed they also maintain in contact with the bars so the accuracy of contact definition as well as stability of computations needs to be satisfied. Thus, both methods in terms of SHPB numerical testing have some disadvantages, but all in all the FE modelling seems to be more suitable for such phenomena. But one can see that some oscillations in stress-strain curves occur in FE modelling. Authors think that the main cause of such phenomena is the contact procedure, which is different from that used in SPH modelling and where slightly penetration was possible to occur. Also, in the free particle technique the artificial viscosity was used, which could also influenced the results.

Authors are aware that obtained stress-strain impulses would not provide constant strain rates during the tests (Naghdabadia et al., 2012; Wu and Gorham, 1997). Also, only one copper shaper was used whereas it is known that for different striker velocities and material (brittle, plastic etc.) various discs should be used: with large diameter and small length or vice versa (Naghdabadia et al., 2012). Nevertheless, for this part of investigations, which has the initial character, such results will be the basis for further testing including different diameter-length ratio studies. Moreover, as discussed in the previous authors' paper (Baranowski et al., 2013), main attention of authors' tests (with this paper as a part of them) is to find an ideal incident shape for the specific type of material using a special shaped striker or the copper shaper presented here. It is also worth to add that at present authors are performing experimental testing for validation of computational analyses and for obtaining the JC material properties of various materials. Taking into account the fact that both methods of modelling are verified the results obtained in future will be much more reliable, interesting and helpful in subsequent investigations.

REFERENCES

1. **Baranowski P., Bukała J., Damaziak K., Małachowski J., Mazurkiewicz L., Niezgoda T.** (2012), Numerical description of dynamic collaboration between rigid flying object and net structure, *Journal of Transdisciplinary Systems Science*, Vol. 16, No. 1, 79-89.
2. **Baranowski P., Malachowski J., Gieleta R., Damaziak K., Mazurkiewicz L., Kolodziejczyk D.** (2013), Numerical study for determination of pulse shaping design variables in SHPB apparatus (in print), *Bulletin of the Polish Academy of Sciences: Technical Sciences.*
3. **Chmielewski R., Kruszka L., Młodożeniec W.** (2004), The study of static and dynamic properties of 18G2 steel (in polish), *Biuletyn WAT*, Vol. 53, 31-45 .
4. **Cloete T.J., V.d. Westhuizen A., Kok S., Nurick G.N.** (2009), A tapered striker pulse shaping technique for uniform strain rate dynamic compression of bovine bone, *EDP Sciences*, 901-907.
5. **Davies R.M.** (1948), A critical study of the Hopkinson pressure bar, *Philosophical Transactions of the Royal Society of London*, Vol. 240, 375-457.
6. **Ellwood S., Griffiths L.J., Parry D.J.** (1982), Materials testing at high constant strain rates, *Journal of Physics E: Scientific Instruments*, Vol. 15, 280-282.
7. **Foley J.R., Dodson J.C., McKinion C.M.** (2010), *Split Hopkinson Bar Experiments of Preloaded Interfaces,* Proc. of the IMPLAST 2010 Conference.
8. **Franz C.E., Follansbee P.S., Berman I., Schroeder J.W.** (1984), *High energy rate fabrication*, American Society of Mechanical Engineers.
9. **Graff K.F.** (2004), *Wave Motion in Elastic Solids*, Dover Publications, New York.
10. **Hallquist J.O. (2003),** *LS-Dyna:Theoretical manual*, California Livermore Software Technology Corporation.
11. **Hopkinson J.** (1872), On the rupture of iron wire by a blow, *Proc. Literary and Philosophical Society of Manchester*, 40-45.
12. **Janiszewski J.** (2012), *The study of engineering materials under dynamic loading* (in polish), Military University of Technology, Warsaw.
13. **Jankowiak T., Rusinek A., Lodygowski T.** (2011), Validation of the Klepaczko–Malinowski model for friction correction and recommendations on Split Hopkinson Pressure Bar, *Finite Elements in Analysis and Design*, Vol. 47, 1191-1208.
14. **Johnson G.R., Cook W.H.** (1983), *A constitutive model and data for metals subjected to large strains, high strain rated and high temperatures*, Proc. from the 7th International Symposium on Ballistics.
15. **Klepaczko J.R.** (2007), *Introduction to Experimental Techniques for Materials Testing at High Strain Rates*, Institute of Aviation, Scientific Publications Group.
16. **Li S., Liu W.K.** (2002), Meshfree and particle methods and applications, *Applied Mechanics Reviews,* Vol. 55. No. 1, 1-34.
17. **Li X.B., Lok T.S., Zhao J.** (2005), Dynamic Characteristics of Granite Subjected to Intermediate Loading Rate*, Rock Mechanics and Rock Engineering*, Vol. 38, No. 1, 21-39.
18. **Naghdabadia R., Ashrafia M.J., Arghavani J.** (2012), Experimental and numerical investigation of pulse-shaped split Hopkinson pressure bar test, *Materials Science and Engineering A*, Vol. 539, 285-293.
19. **Saint-Venant A. J. C. B**. (1855), Memoire sur la Torsion des Prismes, Mem. Divers Savants, Vol. 14, pp. 233–560.
20. **Sankaye S.S.** (2011), *Dynamic testing to determine some mechanical properties of aluminium, copper and dry eglin sand using Split Hopkinson Pressure Bar (SHPB), high speed phtography and digital image correlation (DIC),* Master of science thesis, Aurangabad, Maharashtra, India.
21. **Seng L.K.** (2003), Design of a New Impact Striker Bar for Material Tests in a Split Hopkinson Pressure Bar, *Civil engineering Research Bulletin*, Vol. 16, 70-71.
22. **Steinberg D.** (1906), *Equation of State and Strength Properties of Selected Materials*, Lawrence Livermore National Laboratory, Livermore, CA.
23. **Vulovic S., Zivkovic M., Grujovic N., Slavkovic R.A.** (2007), Comparative study of contact problems solution based on the penalty and Lagrange multiplier approaches, *J. Serbian Society for Computational Mechanics*, Vol. 1, No. 1, 174-183.
24. **Wu X.J., Gorham D.A.** (1997), Stress equilibrium in the Split Hopkinson Pressure Bar Test, *Journal of Physics IV France 7,* Vol. 3, 91-96.

ANALYSIS OF TECHNICAL CONDITION ASSESSMENT
OF GAS TURBINE BLADES WITH NON-DESTRUCTIVE METHODS

Józef BŁACHNIO*

*Bialystok University of Technology, Faculty of Mechanical Engineering, ul. Wiejska 45C, 15-351 Bialystok, Poland

j.blachnio@pb.edu.pl

Abstract: Structural components of gas turbines, particularly the blades, sustain a variety of damages during the operation process. The most frequent cause of these damages are the overheating and thermal fatigue of the material. A primary technique to assess condition of the blades is the metallographic examination. In spite of the fact that metallographic analysis delivers much more information on the structure of examined blade material, it is a type of destructive test resulting in the destruction of the blade which makes further utilization of the item impossible. The paper has been intended to discuss non-destructive testing methods and to present capabilities of applying them to diagnose objectively changes in the microstructure of a turbine blade with computer software engaged to assist with the analyses. The following techniques are discussed: a visual method, based on the processing of images of the material surface in visible light, active thermography, based on the detection of infrared radiation, and the X-ray computed tomography. All these are new non-destructive methods of assessing technical condition of structural components of machines. They have been intensively developed at research centers worldwide, and in Poland. The computer-aided visual method of analyzing images enables diagnosis of the condition of turbine blades, without the necessity of dismantling of the turbine. On the other hand, the active thermography and the X-ray computed tomography, although more sensitive and more reliable, can both be used with the blades dismounted from the turbine. If applied in a complex way, the non-destructive methods presented in this paper, are expected to increase significantly probability of detecting changes in the blade's condition, which in turn would be advantageous to reliability and safety of gas turbine service.

Key words: Gas Turbine, Blade, Diagnosing, Technical Condition

1. INTRODUCTION

A turbine is a rotary flow machine, converting enthalpy of the working medium, also called the working fluid (exhaust stream, gaseous decomposition products or compressed gas) into the mechanical work, causing rotation of the rotor. Because of numerous advantages, such as the ability to develop high power in a compact and low curb weight, relatively high efficiency of energy conversion of the process (30-45%), simple structure, ease of use in different climatic conditions (particularly at low temperatures of the surrounding medium), and a fairly large reliability, the turbines found many applications, among others in power industry, traction motors, marine and aviation engines as well as in aerospace technology. Unfortunately, gas turbines also have drawbacks, which mainly include high operating temperature of some of their parts such as blades and large rotor speeds. Currently, depending on the materials of which the blades are made and treatments such as cooling or blade coating using special heat resistance coating (Skočovský et al., 2004), the temperature of the gas turbine working medium ranges from 1100 to 1600 K, and in some designs it is even higher (Pike and Flower, 2006). Moreover, the rotational speed of, for instance, aerial turbine engines, depending on their design and purpose can reach as much as 100k. rpm or even more.

In the process of operation, different types of damage to the gas turbine components may occur (Błachnio and Kułaszka, 2009; Błachnio, 2011; Karczewski, 2008; Szczepanik and Rządkowski, 2012). The parts of the turbine that are the most vulnerable to damage are blades, whose technical condition is crucial for the reliability and service life of the entire turbine and the assembly,

in which it is embedded. The main causes of a gas turbine's damages are its overheating and thermal fatigue (Fig. 1).
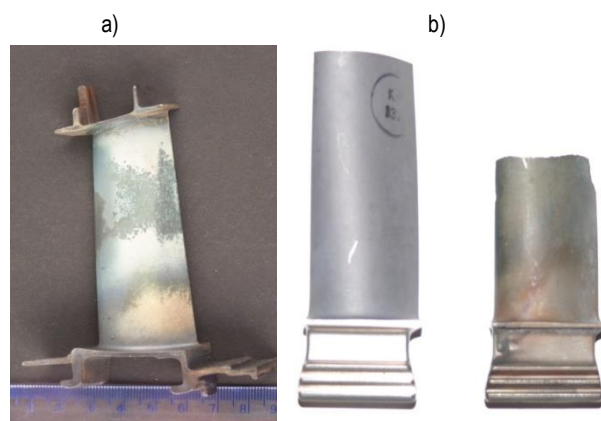

Fig. 1. a) – a vane with overheated area, b) – an image of the blade clipped due to overheating (Błachnio and Kułaszka, 2009; Błachnio, 2011)

This is mainly due to adverse operating conditions or manufacturing defects, such as use of insufficiently durable types of protective coating or applying them on the blade material in a wrong way (Błachnio and Pawlak, 2011; Burakowski, 2002; Maldague, 2001). The reaction of the blade material to mechanical loads depends mainly on its operating temperature. The choice of material for manufacturing blades with a projected durability must include their mechanical properties in the area of the

maximum temperature on a given blade. A typical temperature distribution along the blade feather is very uneven (Fig. 2). Damages to the first (central) stages of a turbine are usually caused by the impact of high temperature of exhaust, whereas damages to the last, (peripheral) stages (turbines with the longest blades) originate mainly from the effects of mechanical strain (vibration, centrifugal force) (Błachnio, 2011; Karczewski, 2008; Szczepanik and Rządkowski, 2012; Marsh, 2013).

Overheating of the blades is the result of the exceeding of the permissible average exhaust gas temperature value as well as non-uniform temperature distribution at the periphery. One of the reasons for the irregularity of the temperature behind the turbine is not appropriate fuel spray caused by varnish deposits accumulating on the injectors (Błachnio and Pawlak 2011).
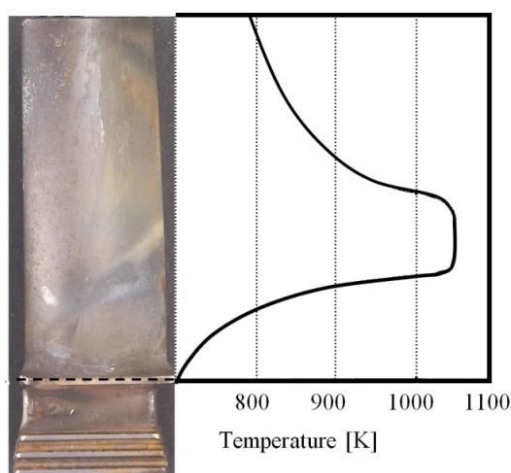

Fig. 2. A diagram of the typical temperature distribution along the gas turbine blade feather (Błachnio, 2011)

An occurrence of the failure of the gas turbine leads to its destruction. This situation forced the constructors and researchers of the turbine engines to develop non-destructive methods of evaluating the turbine's condition (Maldague, 2001). So far, the most common method is a visual one (Błachnio and Kułaszka, 2009; Karczewski, 2008). It allows for testing of overheating structures even of those hard-to-reach engine components in a non-invasive way, however, with relatively small reliability (Pitkanen et al., (2001)). The assessment of the state of overheated blade is performed visually by a diagnostician using videoscope, and comparing the resulting image with the reference one. This type of diagnosis, however, is fraught with subjective error, therefore, the diagnostician's decision is verified by performing a destructive metallographic examination.

An important task of the aircraft engines use is to adopt maximally available diagnostic methods and knowledge in order to detect early enough and interpret the symptoms of the possible risks, to perform repairs in the most favourable moment in respect of minimizing losses, as well as to prevent failures (Spychała et al., 2013; Żółtowski and Cempel, 2004). Furthermore, the high cost of repair of aircraft engines has become one of the reasons for developing new non-destructive assessing methods performed in the process of supported operating as well as during the verifications, when repairing turbine components is being conducted.

2. VISUAL METHOD BASED ON PROCESSING IMAGES OF THE SURFACE OF THE TURBINE BLADES IN VISIBLE LIGHT

Visual method is commonly used in a non-destructive examination of technical objects (Błachnio and Kułaszka, 2009; Karczewski, 2008). In the case of the use of optical instruments, and in particular a videoscope, it is possible to inspect the object without necessity of disassembling it. The acquisition and development of information that could be useful for the diagnosis of machine parts, is a complex process that requires multiple treatments. In general this process can be summarized as follows (Błachnio and Bogdan, 2010; Bogdan et al., 2009):

- Illumination of the diagnosed object located in the background with white light,
- Acquisition of the test object image,
- Digital analysis of the image,
- Presentation of information on the image.

Illuminated surface of the blade can be recognized by a light-sensitive detector (CCD matrix with an optical system – optoelectronic system) through a secondary source of light from its surface. CCD matrix counts incident photons, energy of the light rays incident on each pixel. In the case of a computer vision system the image is obtained from ambient by means of an optoelectronic device – videoscope (Fig. 3). This enables indirect method of diagnosis of the object through the processing and analysis of data collected in the form of digital images.

Fig. 3. Optoelectronic device – videoscope (EVEREST XLG3-Video Probe**.** 2006)

Features of digital images allow to determine their histogram, i.e. the frequency chart of successive values of pixels in the image. The histogram shows how numerous are points in the image with different brightness values lk (Adamczyk and Będkowski 2005; Bogdan et al., 2009). It is assumed that the first element of the histogram has the number 0, and the last is equal to the number of levels of image brightness. If the image contains mxn points and is saved using P levels of gray (for monochrome image):

$p_m = \{0,1,21, ,l_k, , 254,255\}$ and for the RGB color image:

$p_R = \{0,1,21, ,l_k, , 254,255\}$,

$p_G = \{0,1,21, ,l_k, , 254,255\}$,

$p_B = \{0,1,21, ,l_k, , 254,255\}$, then the usual result is *mxn/p* that

have a certain level of gray or shades of colour component in the case of colour images. The histogram is represented as a vector of length corresponding to the number of brightness levels, it can be written as follows (Wróbel and Koprowski, 2004):

$$h(l_k) = \sum_{m=1}^{M} \sum_{n=1}^{N} p(l_k, (m,n)) \qquad (1)$$

where: $h(l_k)$ - the sum of points, that level of gray equals l_k and

$$p(l_k, (m,n)) = \begin{cases} 1; \text{for } L1(m,n) \neq l_k \\ 0; \text{for } L1(m,n) \neq l_k \end{cases} \qquad (2)$$

Disruptions that occur in all stages of the process of acquiring and analyzing information impinge on the reduction of the efficiency of data acquisition in the form of digital images. The following assumptions for research are being assumed:

− Acquisition of images in the same conditions and the same resolution,
− Illumination – diffuse white light,
− No light interference – reflected from other surfaces,
− Acquisition of images using a videoscope of the same resolution at the same magnification.

Representative areas (averaged ROI areas – regions of interest) are selected to describe the tested surfaces unequivocally. By means of the Matlab software (Image Processing Toolbox) image of the blade surface is transformed into the RGB colour image or grayscale image. Typically, the test of image histogram is carried out in order to determine whether the "black-white" information is sufficient to describe the change of the colour caused by the action of high temperature (superheat).

Parametric description of histograms is to determine the position of the maximum value of the amplitude, i.e. the number of pixels (ordinate axis) for the values of saturation of grayscale or RGB (abscissa axis) – Fig. 4. In order to extract diagnostic information the examined waveforms of the changes of the maximum amplitude values in the function of temperature are approximated by polynomials.
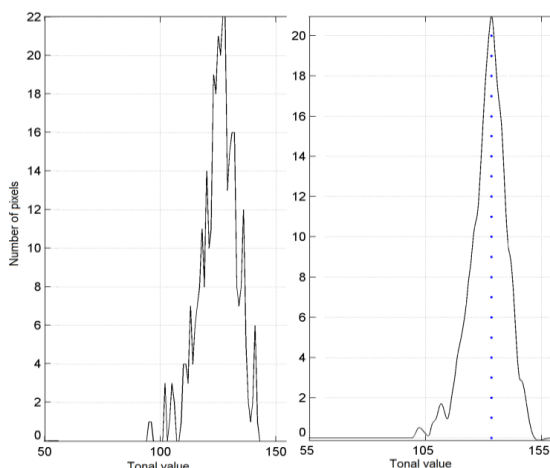

Fig. 4. Exemplary spectral analysis of the image of blade surface (Błachnio and Bogdan, 2010)

Acquisition by videoscope and computer analysis of images of the surface samples of the blades made of superalloy EI-867 WD were performed before and after heating in a furnace in realistic conditions. Studies of the first order statistics (parametric

description of histograms) of images of blades surfaces showed a monotonic decrease of values of the amplitude of grayscale saturation (Fig. 5).
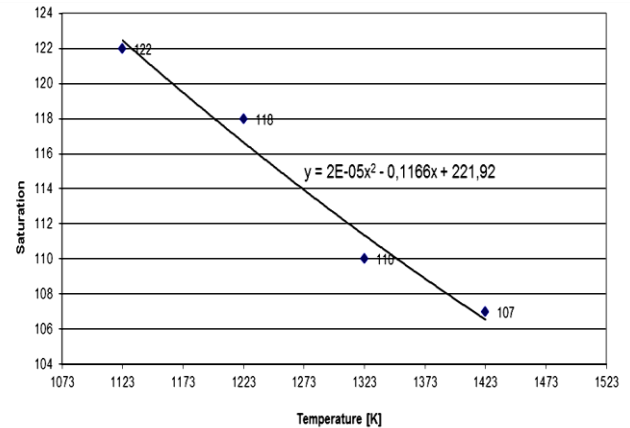

Fig. 5. The values of the position of the maximum amplitude of greyscale saturation of blade surfaces annealed in conditions similar to realistic (Błachnio and Bogdan, 2010)

3. ACTIVE THERMOGRAPHY

Active thermography is based on the detection of infrared radiation. The essence of the study is to analyze the thermal response of the material to external impulse heat stimulation. If a certain amount of energy is delivered to the surface of the material, for example in the form of a heat pulse, after its expiry the surface temperature will start changing rapidly. Due to thermal diffusion, thermal front will move into the material. The presence of areas with different thermal properties (including defects) compared with areas without defects causes a change in the diffusion rate. Thus, by monitoring the temperature field on the surface of the cooling sample, it is possible to reveal position of the defects. Depending on the stimulation method, there are a few types of active thermography, namely, pulsed thermography, lock-in thermography with modulated heating and pulsed phase thermography (Oliferuk, 2008; Holland, 2011). Pulsed thermography is considered to be a relatively simple kind of active thermography. It depends on the determination and analysis of the temperature distribution in the study area during its cooling down after prior uniform heating with the use of thermal pulse (Fig. 6).
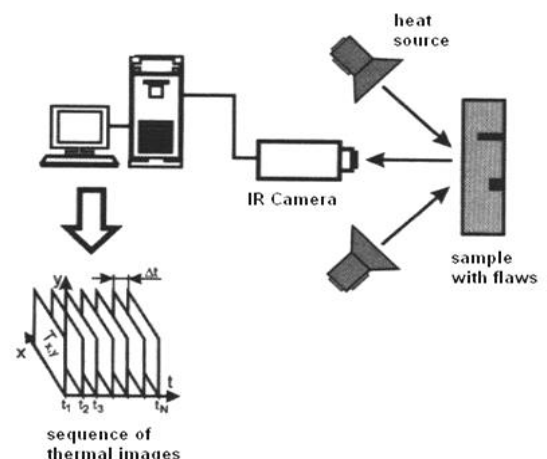

Fig. 6. Application diagram for the pulsed thermography (Oliferuk, 2008)

For one-dimensional model and homogeneous material, the expression of the temperature change during the cooling of the surface heated by short thermal pulse, is as follows (Oliferuk, 2008):

$$T(t) - T(0) \sim Q\alpha^{-0.5}t^{-0.5} \qquad (3)$$

where Q is the heat pulse energy per unit of area, t - surface cooling time, $T(0)$ is the temperature at a selected point or area of the heated surface, just after extinguishing the pulse, and $T(t)$ – the temperature in the cooling process at any time.

The occurrence of defects in the material reduces the diffusion rate which means that temperature of the surface area above the defect will be different from the temperature of the region under which there are no defects – and therefore, the aspect of the above relationship changes. This method (as well as others), has limitations, since due to rapidly fading with depth the temperature contrast it only allows for the detection of subsurface flaws.

Thermographic examinations covered the turbine blades made of alloy EL-867WD, classified into various categories: new, used - fit and damaged during turbine engine operation. The obtained results confirmed changes of parameter dependence of thermal response of the examined blade materials to stimulating heat pulse (Fig. 7).
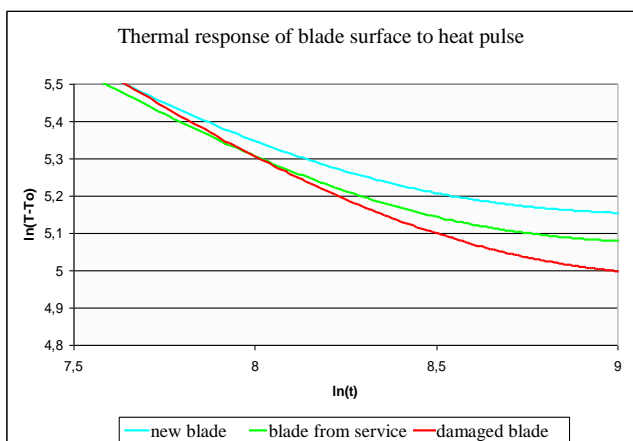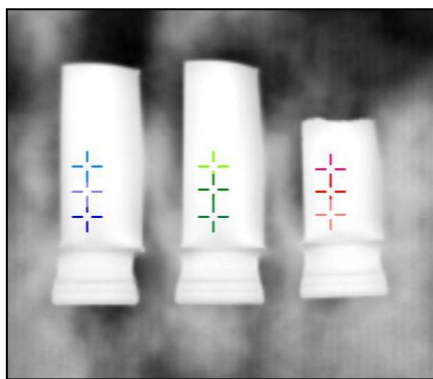

Fig. 7. Blades thermograph and changes of dependence
of the parameter ln(T-To) of the thermographic signal
at selected points of the blade surfaces (Kułaszka et al., 2011)

While on the basis of the analysis of the response to the heat pulse of the blade material classified as "unfit", it was possible to determine areas clearly deviating from the average value. These areas coincided with areas visually assessed as overheated which, combined with the results of the tests conducted on sam-

ples (Fig. 7) allows to draw conclusions on superheated structure of the material.

4. X-RAY COMPUTER TOMOGRAPHY

Tomography is the collective name for the diagnostic methods aimed at obtaining a spatial image of the machine element. In the technical diagnosis, a method of computed tomography (called CT) has been widely applied (The research report, 2011). It is a kind of X-ray tomography allowing for obtaining spatial images (3D) from the radiograph scanning of the object performed from different directions (Fig. 8).

By using the tomograph and a computer implemented program, an object tomogram is obtained. CT is now widely used in industrial production quality control process as a non-destructive method. In the computer tomography radiation source is X-ray tube. The X-ray detectors used in computer tomography are mainly ionization chambers and scintillators. In the scintillation detector, ionizing radiation creates excitation of atoms or scintillator molecules which in turn, by releasing the energy obtained this way, emit quanta of the radiation in the visible range. The light signal must then be converted into the electric signal by a photomultipliers or photodiodes. By using the X-ray source there are performed a series of radiographies with a beam of X-rays. The data stream from the detectors contains information about the absorption (scattering) of radiation through the various components of the test object. These data are stored in computer memory and digitally analyzed in order to obtain monochrome images.
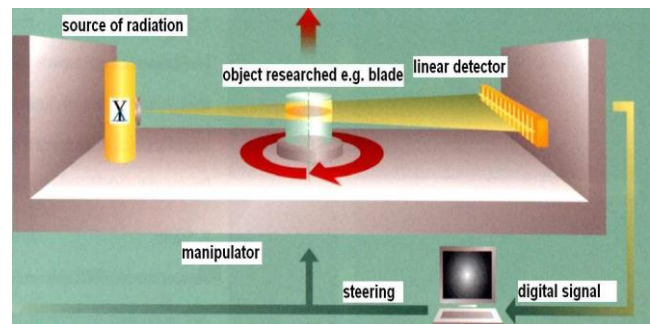

Fig. 8. The example of a tomography investigation with use of a linear
detector (Electronic Instrument CT–X-ray, 2011)

Each cross section of X-rays through object of study is divided into small parts – voxels. For each voxel there is assigned a numerical value proportional to the degree to which it absorbs radiation. To determine this value for n voxels there is a need of at least n of equations describing the absorption in a given layer. N different cross-layer projections are needed. The more projections, the better image accuracy is achieved. The most commonly used image reproducing methods are analytical methods. They are able to yield the best results, but require large computing power. Two-dimensional Fourier analysis method uses fast Fourier transform to describe obtained absorption profiles. Transformation is subjected to each of the projection, and thus the absorption coefficient in each of the voxels is obtained. The absorption coefficients are converted to CT numbers, also called HU Hounsfield units (The research report, 2011):

$$1HU = K \frac{\mu_p - \mu_w}{\mu_w} \qquad (4)$$

where: K – constant image enhancement (individual for each tomography) μ_p – pixel absorption coefficient μ_w – the coefficient of water absorption (reference value).
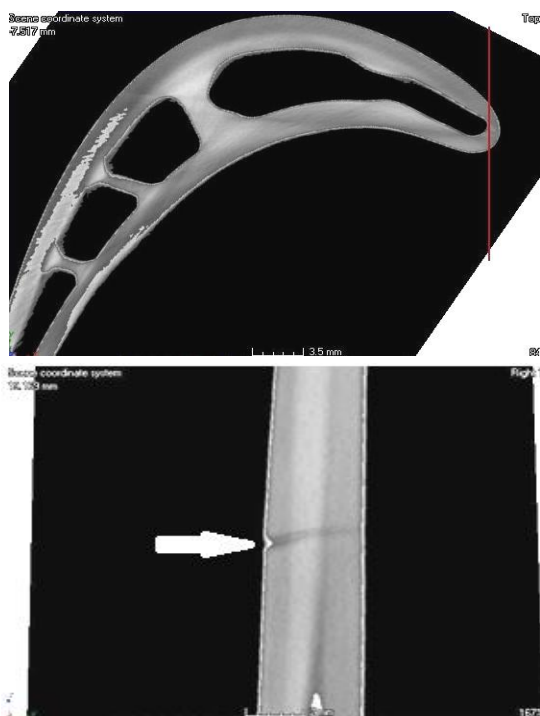

Fig. 9. Tomogram of a turbine blade with a visible crack at the leading edge (Chalimoniuk et al., 2013)

In order to obtain high accuracy of projection the internal structure of machine element, the radiation beam is limited by the diaphragm to a flat beam and a digital linear detector is used (one series of sensors). After rotating the element by 360° a flat X-ray image of slice is obtained. In order to obtain a spatial image of the entire element, the element is shifted in a vertical plane, and at each step a full turn is made. A 3D image is obtained after processing of all collected data.

Computer radiography applied to turbine blades allows the observation of actual thickness of the inner, invisible walls (Chalimoniuk et al., 2010). An image of the object can be represented in the colours and the shape of the inner wall can be determined in the appropriate scale, e.g., the size and location of the defect. Also, the geometry of the internal components can be accurately measured and the tolerance of their actual dimensions be assessed. Thus, CT scan allows to verify the correctness of realization of the component with a very high degree of accuracy and diagnose internal damages, for example, cracks, blade canals blockage, etc. (Fig. 9).

5. SUMMARY

Various types of damage to the components of gas turbines occur in the process of their operation. Of all parts of the turbine, the most vulnerable to damage are blades, whose condition has a significant impact on the reliability and durability of the entire engine and assembly, in which it is embedded. The main causes of damage to the blades of the gas turbine are their overheating and thermal fatigue. The destruction of the gas turbine blades usually starts with the destruction of the protective coating and, as a result, the blade base material is exposed to direct aggressive impact of exhaust gases. This situation leads directly to overheating of the material, seen as unfavorable changes in the microstructure. As a result, the surface roughness changes, and in particular the colour of the blade surface. The color of the surface is therefore a diagnostic signal, which is used in the visual method. Using computer analysis of image recognition, one can objectively evaluate change in the blade state, such as overheating based on the analysis of the colour changes in its surface. Visual method thus enables diagnosis of the status of the blades without necessity to disassemble the turbine.

Results of the study on gas turbine blades, the new and the used ones, after using an active thermography showed the existence of dependencies and relationships between operational heat load and signals changes of the material thermal response. These dependencies and relationships are used to assess the state of overheating of the gas turbine blade material. Although this method is more sensitive and reliable, however, it can be used after disassembling the blades from the turbine.

Computer tomography allows achieving spatial images of the test objects state in a relatively short period of time. It is characterized by high credibility and reliability. Like the previous method it can be used after disassembling the blades from the turbine. In addition, costly X-ray CT scanner is required for the research.

The use of presented non-invasive methods, especially in a complex manner, significantly increase the probability of detecting condition changes of the blades, which will increase the reliability and safety of operation of gas turbines.

REFERENCES

1. **Adamczyk J., Będkowski K.** (2005), *Digital methods in remote sensing*, SGGW Publishing House, Ed. 1, Warsaw.
2. **Błachnio J.** (2011), Analysis of causes of decohesion of a gas turbine blade made of EI-867WD alloy, Aircraft Engineering and Aerospace Technology, *An International Journal*, Vol. 83 No 1, 14-20.
3. **Błachnio J., Bogdan M.** (2010), A non-destructive method to assess condition of gas turbine blades, based on the analysis of blade-surface image, *Russian Journal of Nondestructive Testing*, Vol. 46, No. 11, 860-866.
4. **Błachnio J., Kułaszka A.** (2009), Computer aided visual inspection of the technical condition of gas turbine blades during their operation period, *Journal of KONES*, Vol. 16, No. 3, 23-30.
5. **Błachnio J., Pawlak W.** (2011), Damageability of gas turbine blades - evaluation of exhaust gas temperature in front of the turbine using a non-linear observer, *Advances in Gas Turbine Technology*, In Tech, 435-464.
6. **Bogdan M., Błachnio J., Derlatka M.** (2009), Computer-aided method of diagnostics of gas turbine blades, *Acta Mechanica et Automatica*, Vol 3, No. 4, 13-16.
7. **Burakowski T.** (2002), The proposal of determining quantitative synergism in surface engineering, *3rd International Conference on Surface Engineering*, Chengdu, P. R. China.
8. **Chalimoniuk M., Błachnio J., Krzysztofik J.** (2010), Analysis of the feasibility to investigate condition of gas turbine vanes by means of the radiographic method, *Journal of KONBIN*, No 1(13), 129-138.
9. **Chalimoniuk M., Szczepanik R., Błachnio J.** (2013), The rate of decohesion of a gas turbine blade as assessed with the X-ray computed tomography (CT), *Journal of KONES*, Vol. 20, No. 3, 89-96.

10. **Electronic Instrument CT–X-ray** (2011), *The research report, Computer Tomography for Industrial Applications*, YXLON. International.

11. **EVEREST XLG3-Video Probe (**2006), *GE Inspection Technologies*.

12. **Holland S. D.** (2011), Thermographic signal reconstruction for vibrothermography, *Infrared Physics & Technology*, 54, 503-511.

13. **Karczewski, Z.** (2008), Endoscopic diagnostics of marine engines, *Diagnostyka*, 3(47), 19-23.

14. **Kułaszka A., Bogdan M., Błachnio J.** (2011), New non-destructive methods of diagnosing health of gas turbine blades, *Advances in Gas Turbine Technology*, InTech, 465-498.

15. **Maldague X.** (2001), *Theory and practice of infrared technology for nondestructive testing*, John Wiley and Sons, New York.

16. **Marsh S.** (2013), Preventig fretting fatigue in blade dovetail roots by modifying geometry of contact surfaces, *Power Transmission Engineering*, 45-49.

17. **Oliferuk W.** (2008), *Infrared thermography for nondestructive testing of materials and equipment*, Gamma Office, Warsaw.

18. **Pike L. M., Flower H. L.** (2006), Gas turbine superalloy with improved fabricability. Advanced Materials and Processes, *ASM International*, Vol. 164, No. 6, 39- 43.

19. **Pitkänen J. et al.** (2001), NDT methods for revealing anomalies and defects in gas turbine blades, *Proc 15th WCNDT*, Rome.

20. **Skočovský P., Podrábský T., Belan J.** (2004), Operational degradation of aluminium-silicone layer of turbine blades made from Ni-based alloy, *The Archive of Machinery Technology and Automation*, Vol. 24, No. 1, 45-52.

21. **Spychała J., Pawlak W., Kułaszka A., Błachnio J.** (2013), Assessment of technical condition demonstrated by gas turbine blades by processing of images for their surfaces, *Journal of KONBIN*, 1 (21).

22. **Szczepanik R., Rządkowski R.** (2012), *A study on the dynamics of aero engine blades under different operating conditions*, Air Force Institute of Technology, Warsaw.

23. **Wróbel Z., Koprowski R.** (2004), *Practice in image processing within the MATLAB software*, EXIT Academic Publishing House, Warsaw.

24. **Zieliński T. P.** (2005), *Digital signal processing - from theory to practice*, Transport and Communications Publishers, Warsaw.

25. **Żółtowski B., Cempel C.** (2004), *Machinery fault diagnosis engineering*, Polish Society of Engineering Diagnosis, Warsaw.

IMAGE OF THE SURFACE OF GAS TURBINE BLADE AS A DIAGNOSTIC SIGNAL

Józef BŁACHNIO*, Iwona ZABROCKA**

*Bialystok Technical University, Faculty of Mechanical Engineering, ul. Wiejska 45C, 15-351 Bialystok, Poland
**student, Bialystok Technical University, Faculty of Mechanical Engineering, ul. Wiejska 45C, 15-351 Bialystok, Poland

j.blachnio@pb.edu.pl, i.zabrocka@e-mail.net.pl

Abstract : This paper outlines a non-destructive method that is suitable for evaluation of condition demonstrated by gas turbine blades and is based on digital processing of images acquired from the blade surface in visible light. To enable high clearness of these images the particular attention is paid to the problem of how to provide optimum conditions for investigations and mitigate geometrical distortions of images acquired from maintenance operations. The paper demonstrates that there are relationships between operation lifetime of blades and discoloration of their surfaces due to overheating of the blade material. These relationships are revealed by digital analysis of images acquired for the blade surfaces and expressed as statistical parameter of the first and second order. To improve unambiguity of the analysis results a low-pass filter was applied. It was demonstrated that these relationships are suitable for evaluation how much the status of the blade material microstructure is altered.

Key words: Gas Turbine, Blade, Discoloration, Computer Assistance

1. INTRODUCTION

The purpose of the technical diagnostics is to assess machine's elements and their suitability for further work. Assessment of a given detail often does not seem difficult, but the diagnostician must also make a forecast of its status in the proximal and distal lifetime horizon. In the case of non-contact testing occasionally this assessment is based on subjective impressions of the person carrying the inspection. It is a very responsible job because of the need to decide whether a part is still usable. On one hand, a part that could still be used for a long time can be replaced, on the other hand leaving it could lead to a tragic accident caused by wearing of the part (Błachnio and Kułaszka, 2009; Szczepanik and Rządkowski, 2012). Ability to assess the technical condition of the machine parts by humans depends on many external factors, hence efforts were made to establish objective ways to assess the state of the elements. [Błachnio and Bogdan, 2010; Bogdan, 2009; Żółtowski and Cempel, 2004). The continuous development of digital technology promotes computerization of processes, including the diagnostic process. Developing an algorithm for making decisions on suitability of a given element for work requires a choice in the form of input signals and parameters that are to be analyzed (Bogdan et al., 2009; Pike, 2007; Zieliński, 2005).

The article presents one of the possible ways of evaluating the degree of overheating of the gas turbine blade by image processing of its surface in visible light. As input data of the model, the digital image of the surface of operating gas turbine blades has been selected, and as a result of data processing, numerical information were obtained facilitating objective assessment of the degree of overheating of the blades.

2. RESEARCH OBJECTS

Gas turbines are widely used, among others in power plants and heat-power plants or in transportation through water, land and air. The basis of their operation is the process of combustion inherently involving gases of extremely high temperatures affecting in a negative way surfaces of turbine blades (Błachnio and Kułaszka, 2009; Karczewski, 2008; Skočovský et al., 2004).

In order to obtain images of the surface of the gas turbine blades usually optoelectronic devices are used, such as video scopes or video analyzers (Błachnio and Kułaszka, 2009; Rafałowski, 2004). They enable acquiring of images of machine parts with difficult access. Such a device (Fig. 1) consists of a central processing unit, acting as a mobile workstation that allows for management of the collected data, and the inspection probe equipped with a strong light, which is a focused beam of light, making it difficult for even illumination of the shooting area.

Fig. 1. Optoelectronic device – videoscope
(Błachnio and Kułaszka, 2009)

The acquired images of the gas turbine blade surfaces are stored in the form of a digital image of the RGB colour model in 24-bit mode (Adamczyk and Będkowski, 2005; Watkins et al.,1995; Wróbel and Koprowski, 2004). This format is the basic format of colour images and allows for up to 16 777 216 colours, as each of the three primary colours (red , green, blue) may be of 256 different shades. Any colour can be described by three

numbers in the range from 0 to 255. White colour is encoded by three numbers [255,255,255], while black is [0,0,0]. This model is mainly applied in televisions, computer screens and digital cameras.

RGB model differs significantly from the way man does it: human technique of colour identification relies on an assessment of

their attributes (Doros, 2005; Sankowski et al., 2011). The colour attribute should be understood as a characteristic, intrinsic property that is used to describe one of the three features of a colour: hue (colour, tone) – qualitative difference of a colour, its saturation – colour deviation from whiteness, brightness - indicates whether the colour is closer to white or black.
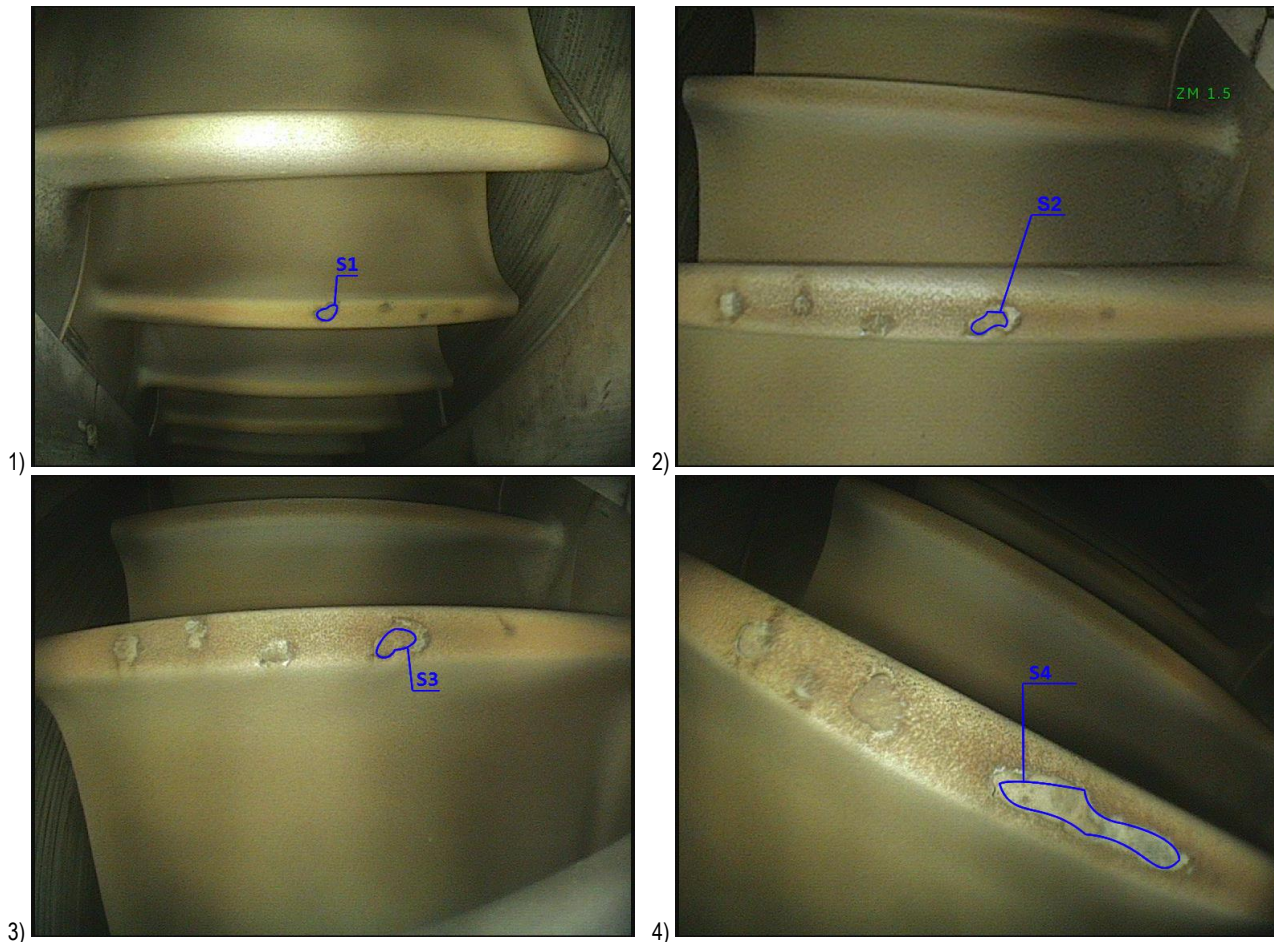
Fig. 2. Photos of a gas turbine blade after successive inspections with marked areas of interest (Spychała et al., 2012)

Fig. 3. Analyzed images of the following areas of the blade

The images of exemplary gas turbine blade, obtained by using a videoscope, are shown in Fig. 2. The photos were taken during subsequent inspections of the turbine, with a fixed interval of time between maintenance sessions (Karczewski, 2008; Spychała et al., 2012). In the next stage some interesting images were selected – showing damage to blades, also subsequently analyzed (Fig. 3). Due to the irregular shape of the damaged parts being in focus of examination, they were placed on a black background, so as to form a rectangular image of MxN pixels.

3. METHODOLOGY OF RESEARCH

To process and analyse the images Mat lab-based programs were applied . As a result, some parameters were obtained, by means of which an objective assessment of the blade feather was carried out, damaged due to overheating of its material. These parameters were determined on the basis of the histogram distribution of brightness. A histogram is one of the graphical ways of presenting the empirical distribution of characteristics. In the case of a digital image, the histogram shows the frequency

of occurrence of pixel values. On the x-axis, there are marked successive levels of values of brightness, from 0, meaning black, to 255, meaning white. The y-axis, on the other hand, is marked with the quantity of pixels of different brightness values. The histogram may not only be designed for a monochrome image, but also for each primary colour; then zero represents the darkest colour hue, and the number 255 the lightest colour.

The histogram is represented by a vector of length equal to the number of brightness levels of a given image and can be presented as follows (Bogdan, 2009; Watkins et al.,1995; Wróbel and Koprowski, 2004):

$$H(l_k) = \sum_{m=1}^{M} \sum_{n=1}^{N} p(l_k, (m,n)) \tag{1}$$

where: $H(l_k)$ – the total of points at l_k – given brightness level, and

$$p(l_k, (m,n)) = \begin{cases} 1; & \text{dla } L(m,n) = l_k \\ 0; & \text{dla } L(m,n) \neq l_k \end{cases} \tag{2}$$

Additionally, the histogram can be presented in a standardized form, i.e., the one in which each value histogram is divided by the total number of pixels *(M • N)*.

$$H_{zn}(l_k) = \frac{\sum_{m=1}^{M} \sum_{n=1}^{N} p(l_k,(m,n))}{M\,N} \tag{3}$$

Statistical parameters of the histogram are:
− medians – the middle element of an ordered set of values tested in ascending order;
− quintiles – elements which are 0% (the minimum element), 25%, 50% (median), 75%, 100% (maximum element) in ascending order set of examined values;
− percentiles – elements of a set of values in ascending order, corresponding to, e.g. 10%, 15%, etc.;
Mean value of brightness:

$$\mu = \sum_{i=0}^{L-1} \frac{i\,H(i)}{M\,N} \tag{4}$$

Variation of the brightness distribution:

$$\sigma^2 = \sum_{i=0}^{L-1} (i-\mu)^2 \frac{H(i)}{M\,N} \tag{5}$$

is a measure of the range of distribution around the mean value; the higher the value, the results are more scattered around the mean.

Skewness of histogram:

$$\mu_3 = \sigma^{-3} \sum_{i=0}^{L-1} (i-\mu)^3 \frac{H(i)}{M\,N} \tag{6}$$

is indicative of the asymmetry of distribution around the mean value; it provides information about differences between positive and negative deviations from the mean value. Its value equals 0 for symmetric distribution, $\mu_3 < 0$ for the left-asymmetric distribution, and $\mu_3 > 0$ for the right-asymmetric distribution.

Histogram kurtosis:

$$\mu_4 = \sigma^{-4} \sum_{i=0}^{L-1} (i-\mu)^4 \frac{H(i)}{M\,N} - 3 \tag{7}$$

(where: L – number of brightness levels, i – brightness level, $H(i)$ – histogram value for a given brightness level, $M\,N$– picture resolution) is an indicator of concentration level around mean value, $\mu_4 < 0$ for peaked distribution, $\mu_4 > 0$ for normal distribution.

The use of the algorithm of the main program's function (Fig. 4), which is used for image processing, resulted in the deletion of the envelope of histograms and setting the brightness level corresponding to the maximum saturation. Due to the very irregu-

lar shape of obtained histograms it was difficult to determine what is the value of brightness occurring with the largest number of pixels in the image. For this reason, filtration was conducted with the use of low-pass filter (Doros, 2005; Pawlak, 2007; Watkins et al., 1995) which was built with blocks available in Simulink (Fig. 5), a part of the MATLAB. As a result of applying this procedure, the effect of smoothing of the histogram graph was achieved (Fig. 6), which allowed for determining of the brightness values attributable to the maximum saturation. A method for obtaining of the value for this parameter represents the diagram in Fig. 7.
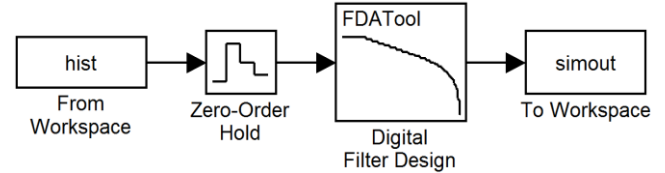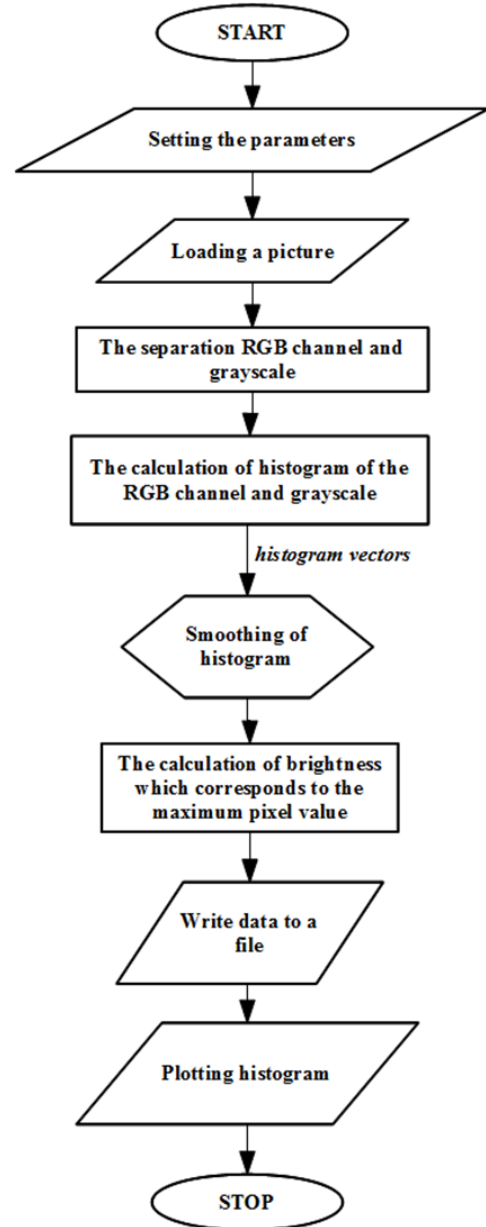

Fig. 4. Algorithm of the main program's function

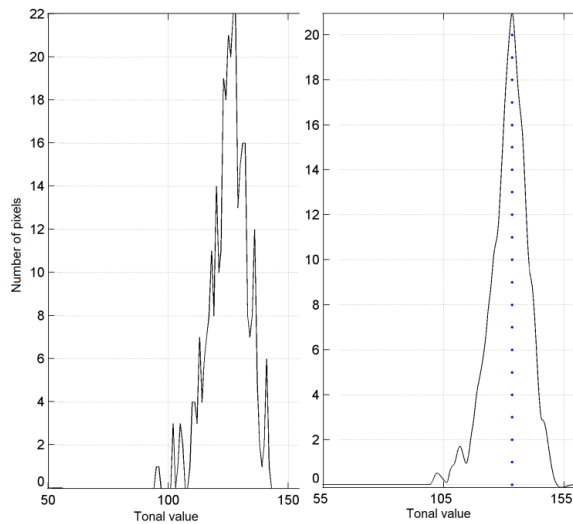**Fig. 5.** Block diagram of smoothening subprogram

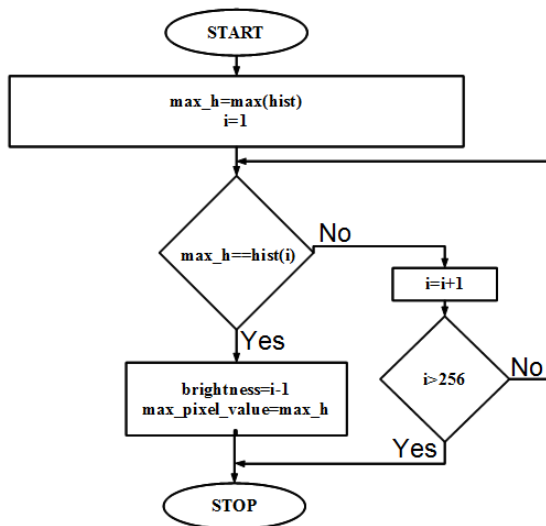**Fig. 6.** Exemplary histogram before and after smoothening process

Fig. 7. Schedule of determining the maximum value of the histogram

To calculate the statistical parameters: mean of brightness, variance, skewness and kurtosis a separate program was applied. The method of their determination has been modified so as to prevent added background from generating calculation errors.

The introduced amendment consisted in substituting values into the formulae (4), (5), (6), (7):

- for M N pixels summed up in the program, whose values are different from zero,
- $H(0) = 1$, which is resetting the sum of black pixels of the background,
- $(i-1) - \mu$ – Matlab indexes arrays starting at 1, hence the values corresponding to their own brightness levels are shifted by one.

This procedure resulted in activating the calculation of statistical parameters only for pixels transferring analyzed data.

4. RESEARCH RESULTS

Data obtained during the processing of images were placed on graphical charts that illustrate the changing parameters with the duration of the gas turbine exploitation.

Fig. 8 represents graphs showing the progression of the changing position of maximum saturation of operating blades. For monochrome images, the brightness of the areas of damage increases. In the case of RGB colour components , these results are not so obvious, the trend lines set for them have a lower correlation coefficient. Charts with average brightness of the damaged areas are presented in Fig. 9. Runs of average brightness of images are similar in shape to the waveform changes in the position of maximum saturation. Subsequent graphs represent the changes in the variance of the brightness distribution (Fig. 10) during the use of gas turbine blades. There was a significant increase in variance value, which means a greater dispersion of the values around the mean brightness of the pixel. Skewness values (Fig. 11) and kurtosis (Fig. 12) do not form a monotonic sequence and also their correlation coefficients carry low values.
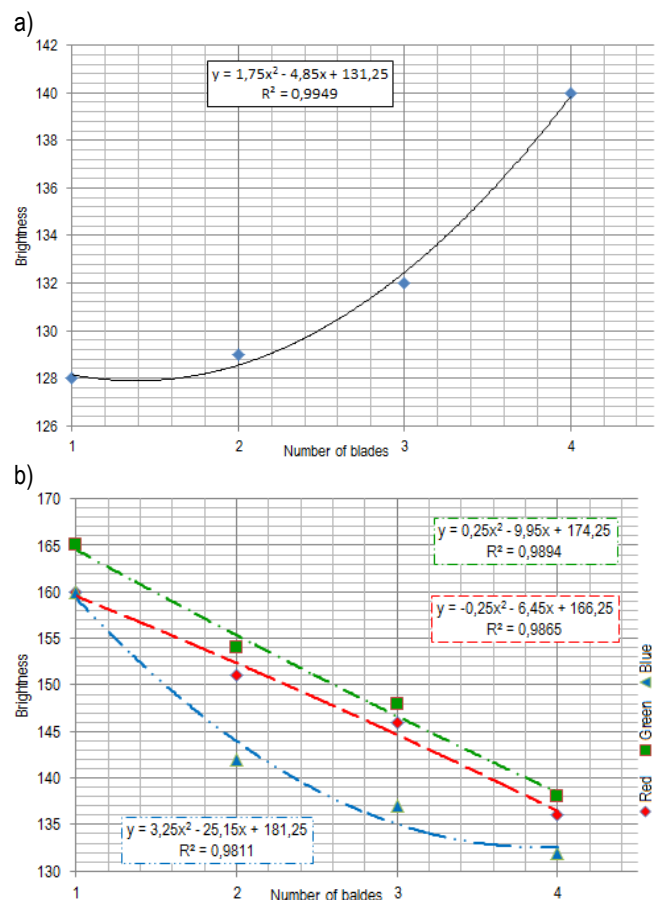

Fig. 8. The brightness values of maximum saturation of areas of interest:
a) monochrome images, b) RGB colour components

The shape and size of damages clearly indicate the expansion of their surface as a function of exploitation time. The processing of the images yielded results confirming continuation of destructive effect of high temperature exhaust on the blade material. Values of calculated statistical data for the parts of the first three diagnostic inspections are of comparable size whereas for the fourth area of interest, their increase is much higher (for clarity attributable to the maximum saturation, the mean brightness and the variance), or other sign (for the skewness and kurtosis of the distribution) with respect to others.
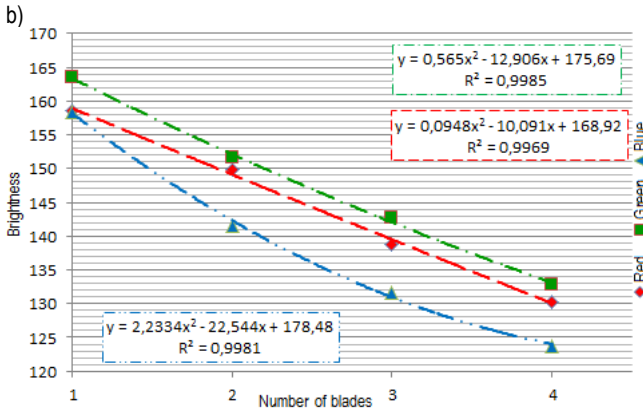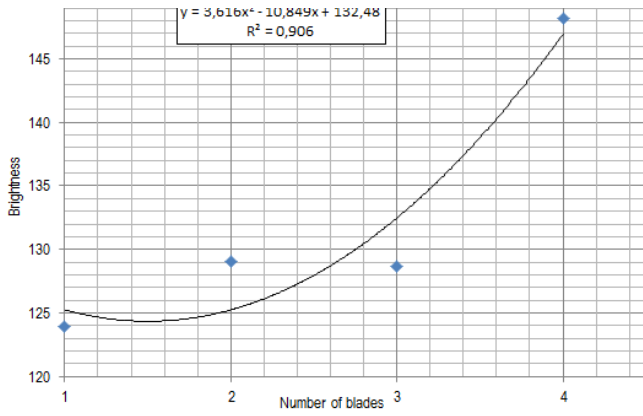
a)

b)

Fig. 9. The average brightness values of maximum saturation of areas of interest: a) monochrome images, b) RGB colour components

a)

b)

Fig. 10. Variance values for brightness distribution of areas of interest: a) monochrome images, b) RGB colour components
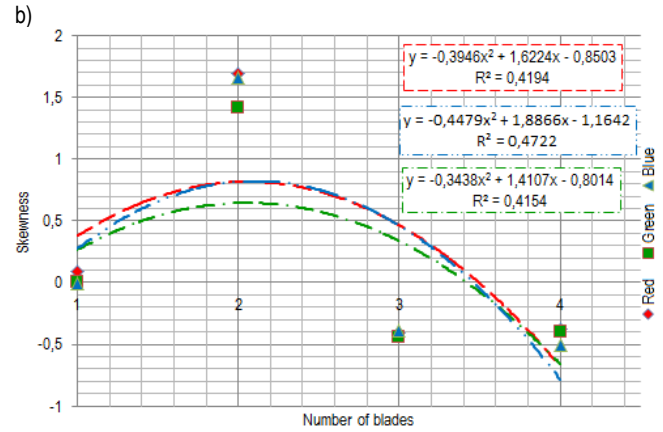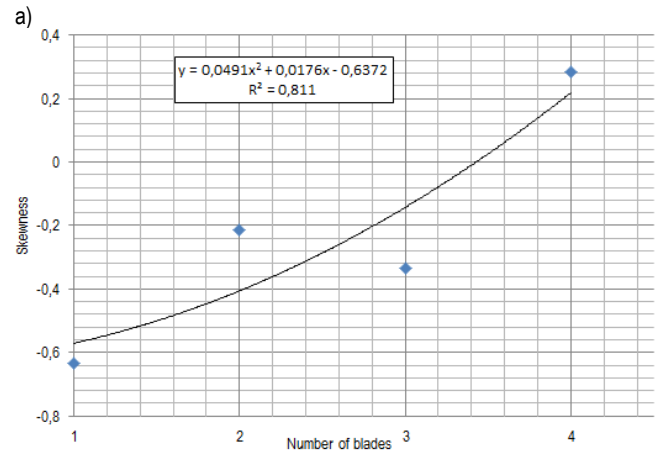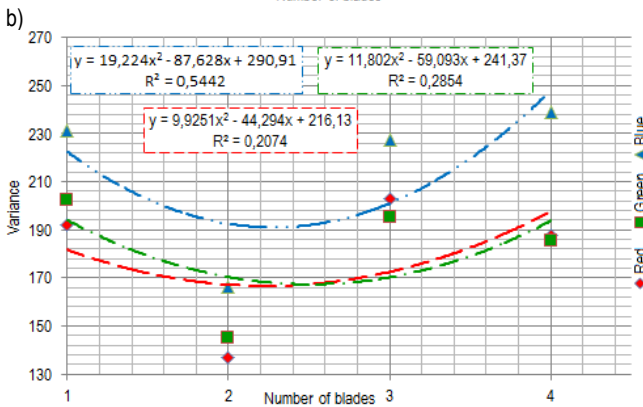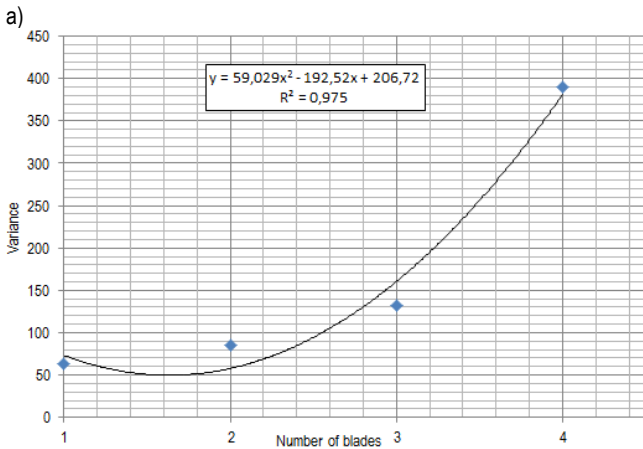
a)

b)

Fig. 11. Skewness values for brightness distribution of areas of interest: a) monochrome images, b) RGB colour components
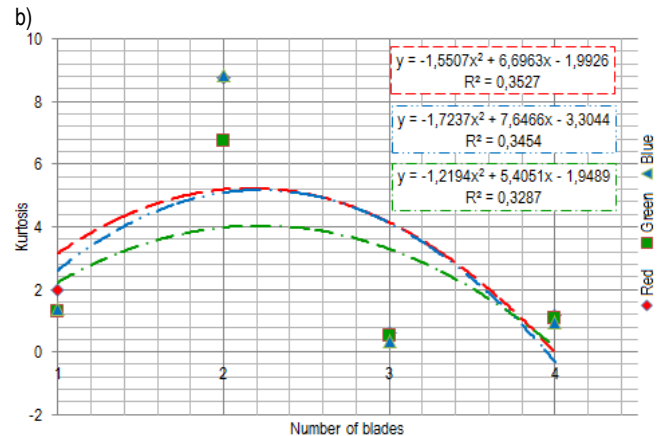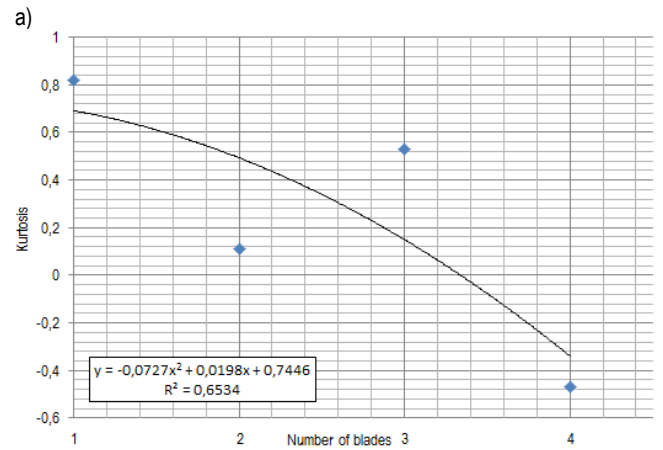
a)

b)

Fig. 12. Kurtosis values for brightness distribution of areas of interest: a) monochrome images, b) RGB colour components

5. CONCLUSION

The operation of gas turbines, like other devices is associated with the occurrence of defects of various character and degree. Due to the conditions in which turbines are operated, the most common faults are blade material overheating and thermal fatigue that are caused by exceeding the limit value for the exhaust gas temperature and its uneven distribution around the circumference of the turbine, all leading to loss of strength of the material. Furthermore, these defects make objective assessment of further ability to use the machine part even more difficult. Since the engine performance depends on the power of the turbine, its efficiency directly affects the power and fuel consumption of the engine. Consequently, the efficiency of the turbine is highly dependent on the temperature of exhaust gas supplied to it. Because gas turbines are commonly applied in power stations and the transport, it is necessary to carry out inspections in which damaged blades are eliminated from operation. However, it is important to bear in mind the fact that not every damage disqualifies a given blade from its further, proper performance. Because of this, an objective, computerized assessment of overheating can optimize the life span of a gas turbine blade.

The research methodology presented in the article is not completely resistant to interference and the results must be correlated with the structural changes of blade material. This should, however, be regarded as a pioneering attempt to develop an algorithm to decide on the suitability or unsuitability of blades for further work. It has been shown that the image of the surface of a gas turbine blade can be used as a diagnostic signal and provide information about its condition, in particular about overheating of the material.

REFERENCES

1. **Adamczyk J., Będkowski K.** (2005), *Digital methods in remote sensing*, SGGW Publishing House, Ed. 1, Warsaw.
2. **Błachnio J., Bogdan M.** (2010), A non-destructive method to assess condition of gas turbine blades, based on the analysis of blade-surface image. *Russian Journal of Nondestructive Testing*, Vol. 46, No. 11, 860-866.
3. **Błachnio J., Kułaszka A.** (2009), Computer aided visual inspection of the technical condition of gas turbine blades during their operation period. *Journal of KONES*, Vol. 16, No. 3, 23-30.
4. **Bogdan M.** (2009), *Diagnostic investigations of gas turbine blades by digital processing of images acquired for their surfaces*, PhD Thesis, Białystok Technical University, Białystok.
5. **Bogdan M., Błachnio J., Derlatka M.** (2009), Computer-aided method of diagnostics of gas turbine blades. *Acta Mechanica et Automatica*, vol 3, no. 4, 13-16.
6. **Doros M.** (2005), *Image processing*, Publishing Office of WIT, Warsaw.
7. **Karczewski, Z.** (2008), *Endoscopic diagnostics of marine engines*, Diagnostyka, 3(47), pp.19-23.
8. **Pawlak W.** (1983), The method for compensation of phase lag in analog low-pass filters, *Scientific output of the Institute of Aviation*, No. 92, Warsaw.
9. **Pike L. M., Flower H. L.** (2006), *Gas turbine superalloy with improved fabricability.* Advanced Materials and Processes, ASM International, Vol. 164, No. 6, 39 – 43.
10. **Rafałowski M.** (2004) *Integrated image analysers as applied to measurements in lighting technology and to assess shapes of objects,* Publishing Office of Białystok Technical University, Białystok.
11. **Sankowski D., Mosorov V., Strzecha K.** (2011), *Industrial systems dedicated image processing and analysis*, Polish Socientific Publishers, Warsaw.
12. **Skočovský P., Podrábský T., Belan J.** (2004), *Operational degradation of aluminium-silicone layer of turbine blades made from Ni-based alloy,* The Archive of Machinery Technology and Automation, Vol. 24, No. 1, 45 – 52.
13. **Szczepanik R., Rządkowski R.** (2012), *A study on the Dynamics of aero enkine blades under different operating conditions,* Air Force Institute of Technology, Warsaw.
14. **Spychała J., Szczepankowski A., Kułaszka A., Sujka W.** (2012), Report No23/34/2012, *Air Force Institute of Technology*, Warsaw.
15. **Watkins C. D., Sadun A., Marenka S.** (1995), *Modern methods for image processing*, WNT Publishing House, Warsaw.
16. **Wróbel Z., Koprowski R.** (2004), *Practice in image processing within the MATLAB software*, EXIT Academic Publishing House, Warsaw.
17. **Zieliński T. P.** (2005), *Digital signal processing - from theory to practice,* Transport and Communications Publishers, Warsaw.
18. **Żółtowski B., Cempel C.** (2004), *Machinery fault diagnosis engineering*, Polish Sosiety of Engineering Diagnosis, Warsaw.

SOFTWARE SUPPORT DEVELOPMENT FOR NUMERICAL SOLUTION OF ANSYS CFX

Tomáš BRESTOVIČ[*], **Natália JASMINSKÁ**[*]

[*]Faculty of Mechanical Engineering, Technical University in Kosice, Department of Power Engineering,
Vysokoškolská 4, 042 00 Košice, Slovak Republic

natalia.jasminska@tuke.sk, tomas.brestovic@tuke.sk

Abstract: The paper deals with possibilities to apply a new developed software support for simulation programme ANSYS CFX. A direct export of heat-transfer coefficients into variables used under edge conditions as well as of physical properties of gas mixtures into material properties during simulation solution of technical tasks means a significant saving of time. The paper summarizes in detail description of the software for calculation of heat-transfer coefficient during free convection (HTC-FC) and of material properties of gas mixture (MPGM) that enable to export calculated data directly into the text files which can be imported then into the programme ANSYS CFX.

Key words: Software, Numerical Methods, Multidimensional Regression, Ansys CFX, Heat-Transfer Coefficient

1. INTRODUCTION

The design of the energy equipments is closely connected with the use of numerical methods based on the finite volume method (FVM). These methods pull down the barriers of classic solutions of problems through an analytical way and speed up the whole calculation (Badida et al, 2008; Trebuňa et al., 2013). The simulation is based on creation of mostly 3D geometry that is then discretized through mesh creation with a final number of elements (Michalec et al, 2010; Kapjor et al., 2010, Kizek et al., 1999). By setting conditions of uniqueness into the simulation tool as well as by applying needed models and differential equations, a numerical calculation is carried out after which it is possible to evaluate sought parameters (Oravec et al, 2010; Durdán et al, 2009, Vranay and Vranayová, 1999). Setting physical and boundary conditions is significantly time-consuming, especially, under dependent boundary conditions. Such a condition is the value of the heat-transfer coefficient (HTC) during simulations of transient phenomena of heating or cooling bodies. The heat-transfer coefficient is considerably dependent on the surface temperature of solved mesh boundary element during free convection, namely while considering radiation (Setoodeh et al, 2011; Mansoori et al., 2002 and Tauš and Kudelas, 2012).

It is possible to use materials library data in the programme Ansys CFX during the simulation calculations in which a gas mixture is simulated. Setting individual parameters of the gas mixture sufficient for solution gives also the possibility to make up the mathematical dependence of the quantities on pressure and temperature of the solved element by means of the multidimensional regression.

The subject of this paper is the description of new created subroutines that facilitate the engineering work at numerical methods in ANSYS CFX.

2. HTC-FC SOFTWARE DEVELOPMENT

Calculations of the heat-transfer coefficient is a time-consuming matter not only with a view to the subtraction of physi-

cal properties of fluids, that are needed for setting criteria of similarity, but also with a view to the cyclic solution for more values of the surface temperatures. With regard to the requirement for speeding up the setting the boundary condition of the 3rd kind, an impulse arose for development of HTC-FC (heat-transfer coefficient – free convection) software that enables to calculate the heat-transfer coefficient for the surface temperature range of geometry specified by the user up to the scope of the criterions equation (Frestl and Masaryk, 2011; Kalaš et al., 2000).

Graphical window is divided for selection of basic geometry types from vertical areas up to the ribbed tubes where a typical dimension l (Fig. 1) is represented at each type. After starting calculation, the programme will read body temperature, fluid temperature, typical dimensions and surface emissivity while considering radiation. In the case of the requirement for storing data into a file, it is possible to set the surface temperature range of the wall as well as the temperature step, by which the calculation will be executed, in the tool bar. An inherent part of the programme is the material selection. Today, it is possible to select air, water or to set the physical properties of any fluid. All material properties are dependent on the temperature. In order to guarantee a right calculation, the programme will check not only the ranges of permissible temperatures, but also the range of individual criterion equations or similarity criteria.
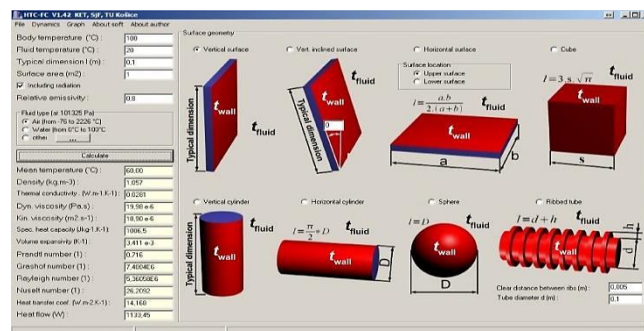

Fig. 1. View of graphical window of the HTC-FC programme

The main advantage of using HTC-FC software is the speeding up the setting the boundary condition of the 3rd kind into the simulation programme ANSYS CFX, as the programme enables to export files with the extension "ccl". They are the text files containing settings in CFX. After selection of the export into the "ccl" file, the programme will ask for the name of the boundary condition by which a duplicate setting will be avoided in case of more boundary conditions in one simulation.

The number of exported values of HTC is dependent on set temperature range and step in the tool bar. Only the total heat-transfer coefficient (Fig. 2 Total HTC - α_c) will be recorded in the file for simulation programme. If the user decides to add radiation into the calculation, it will be reflected in the total HTC as the sum of HTC of free convection and of equivalent HTC from the radiative thermal flux (Pyszko et al., 2010):

$$\alpha_c = \alpha(Pr, Gr) + \varepsilon \cdot \sigma \cdot \left(T_s^2 + T_t^2\right) \cdot \left(T_s + T_t\right) \qquad (\text{W} \cdot \text{m}^{-2} \cdot \text{K}^{-1}) \qquad (1)$$
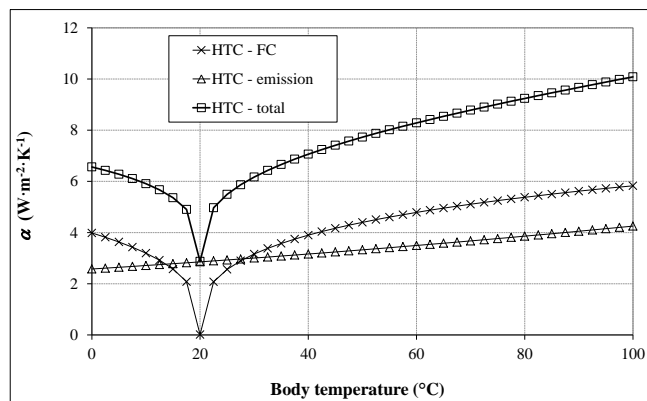

Fig. 2. Course of the heat-transfer coefficient in dependence on the body temperature

Fig. 2 shows the course of the heat-transfer coefficients during free convection calculated by means of the HTC-FC programme for vertical plate with typical dimension 1 m, fluid temperature 20 °C and emissivity 0.5. The fluid used was air.

2.1. HTC - FC software usage

The possibilities of the software usage will be demonstrated by means of cooling a horizontal steel bar of 50 mm in diameter. A CFX domain for ambient air was created during the first simulation and the entire computation of convective heat demand was directly simulated for free convection along with air movement. Radiation was computed using the "Discrete Transfer" model. A domain was created only for the steel bar during the second simulation, whereas the third type boundary condition was applied to the outer cylindrical surface area. The HTC value, computed by the HTC - FC software, and the ambient temperature are known for this condition. The numerical computation without using the fluid domain, and hence without having to solve the Navier-Stokes differential equations, is much faster.

For the horizontal cylinder shown in Fig. 3, dependence of HTC upon the surface temperature of the cylinder (Fig. 4) was generated. The initial temperature of the cylinder was 300 °C and the cooling computation lasted for an hour. The ambient air temperature was set at 25 °C and the radiation ambient was of the

same value. The mean air temperature was used for computation of physical quantities of air.
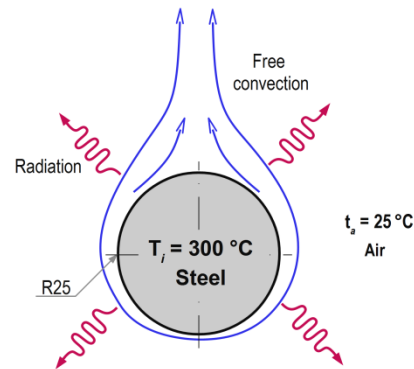

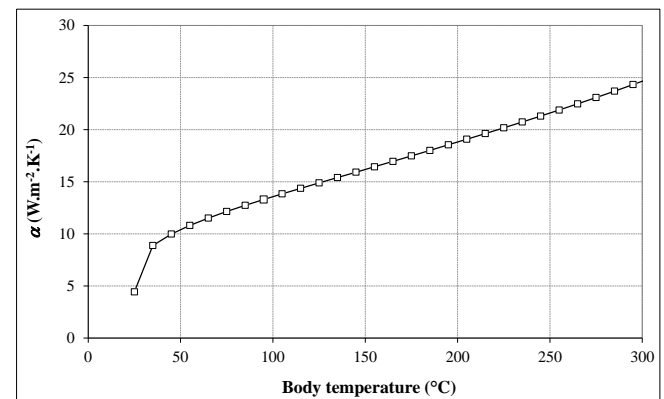**Fig. 3.** Description of cooling of a horizontal cylinder

Fig. 4. Dependence of HTC - horizontal cylinder upon temperature

The surface emissivity was assumed to be 0.7 and the constant value was considered in the whole temperature range. The thermal field of the steel bar along with ambient air after 600 seconds from the beginning of the initial time is plotted in Fig. 5. Air heating results in free convection, which cools the cylinder along with radiation.
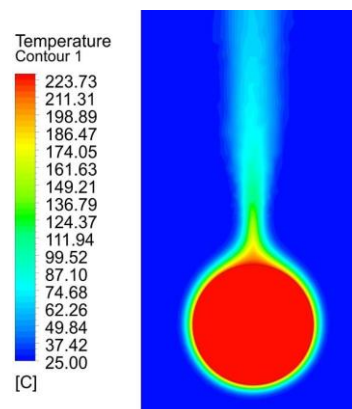

Fig. 5. The thermal field of air and the bar after 600 s for solution of air flow and radiation

The thermal field after 600 s without solution of the ambient air flow, only by applying the third type boundary condition, is shown in Fig. 6 to compare temperatures. In addition to free convection,

HTC also includes radiation HTC equivalent. Given the low value of the Biot number in the range from 0.002 to 0.011 the temperature difference is minimal between the core of the rod and its surface.
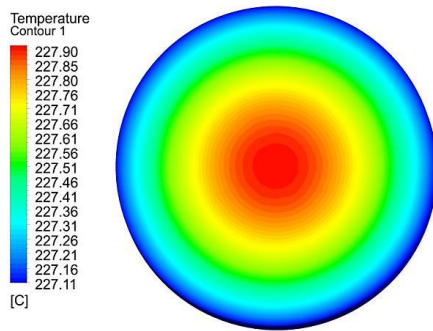

Fig. 6. The thermal field of the bar after 600 s without solution of the air flow and by applying the HTC

The deviation of the average temperature of the horizontal bar after 600 s from the beginning using the different approaches is only 0.06 °C. The comparison of temperature change during the entire solution time and the percentage deviation are shown in Fig. 7. The diagram shows that the time-consuming computation of the cooling fluid flow can be replaced by using HTC in those cases. The computation without considering the air flow was approximately twenty-six times faster in this case while the same iterative accuracy was maintained.
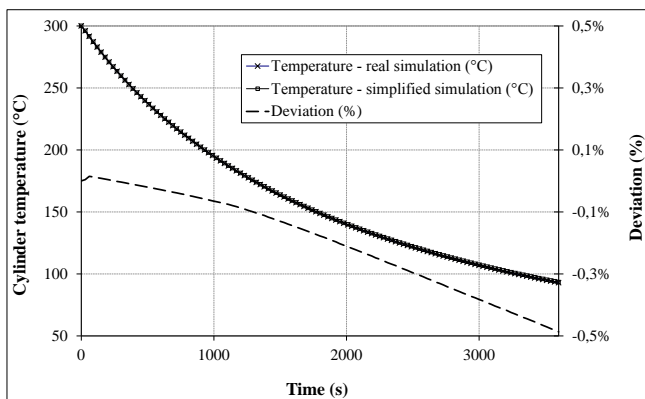

Fig. 7. The course of temperatures and their mutual deviation at simulations

Adequacy of using the simpler approach is strongly dependent upon the type of the solved issue. For complex geometrical shapes, the simulation of fluid flow is more advantageous and accurate due to the effect of mutual radiation of surfaces and the complex fluid flow.

3. MPGM (MATERIAL PROPERTIES OF GAS MIXTURES) SOFTWARE DEVELOPMENT

In ANSYS CFX, it is possible to create the gas mixtures, e. g. by import of clean gases of which the state quantities are calculated by means of Peng-Robinson equatation of state (PR EoS) with consecutive defining their mutual relation. The aim to facilitate setting and defining of gas mixture with its material properties resulted in development of MPGM software (Material Properties of Gas Mixtures,(Tkáč and Hvizdoš, 2008) that has 18 preset gases for any mixture production (Fig. 8).
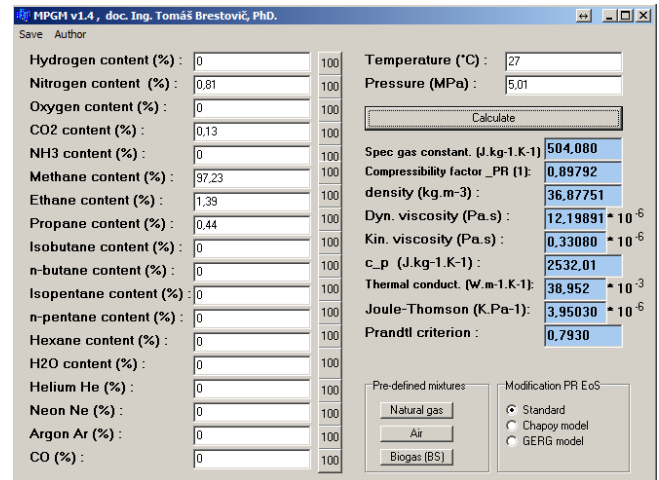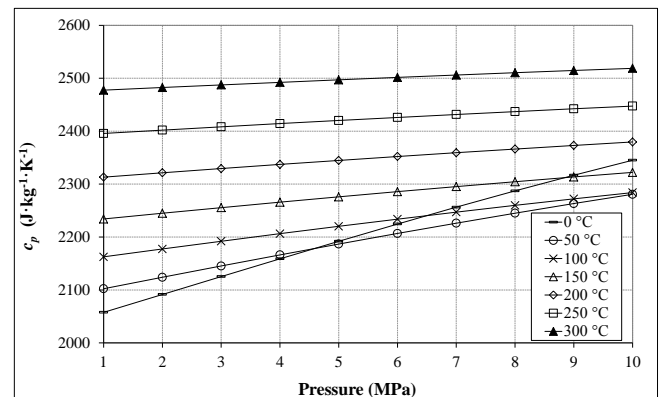

Fig. 8. Graphical window of the MPGM programme

Fig. 9. Course of specific heat c_p = f(p,T) for gas mixture 30 % H_2, 30 % N_2, 40 % CH_4

The programme calculates the compressibility factor according to PR EoS (from which the density is calculated), the specific heat (Fig. 9), transport properties as well as Joule-Thomson coefficient and Prandtl criterion for any gas mixture. These parameters can be used in practice for any of the processes using a mixture of gases at higher pressures, such as the cooling natural gas in compressor station. When the dependencies of physical quantities are exported to HTC- FC program, it can be calculated HTC on the internal heat exchange surfaces of coolers and thus cooling performance can be quantified.

3.1. Peng - Robinson equation of state

The Peng-Robinson equation of state (PR EOS) is a three-parameter modification of the Redlich-Kwong equation of state. The third parameter, which led to the more accurate results, is the acentric factor ω. The constant a was converted into a temperature-dependent one at the same time (Svoboda et al, 2007). The basic form of the equation of state is as follows:

$$p = \frac{R \cdot T}{V - b} - \frac{a}{V \cdot (V + b) + b \cdot (V - b)} \qquad \text{(Pa)} \qquad (2)$$

To compute the compressibility factor, the equation can be derived as follows:

$$z^3 - (1-B) \cdot z^2 + (A - 3 \cdot B^2 - 2 \cdot B) \cdot z - (A \cdot B - B^2 - B^3) = 0 \qquad (3)$$

Where the constants A and B are expressed as follows:

$$A = \frac{p \cdot a(T)}{R^2 \cdot T^2} \qquad (4)$$

$$B = \frac{b \cdot p}{R \cdot T} \qquad (5)$$

The computation of the equation (2) is carried out using the Newton-Raphson method. The parameter $a(T)$ is dependent on the reduced temperature, which represents the ratio of the thermodynamic temperature and the critical temperature of the ith component of a gas.

$$a(T) = 0.45724 \cdot \frac{R^2 \cdot T_k^2}{p_k} \cdot \left[1 + \kappa \cdot \left(1 - \sqrt{\frac{T}{T_k}} \right) \right]^2 \quad (J^2 \cdot mol^{-2} \cdot Pa^{-1}) \qquad (6)$$

$$b = 0.0778 \cdot \frac{R \cdot T_k}{p_k} \qquad (J^2 \cdot mol^{-2} \cdot Pa^{-1}) \qquad (7)$$

$$\kappa = 0.37464 + 1.54226 \cdot \omega - 0.26992 \cdot \omega^2 \qquad (8)$$

Where ω is the acentric factor (1), whose value for the particular components of a mixture of gases is given by references (Svoboda et al, 2007). In respect of compution of the compressibility factor for a mixture of gases, it is necessary to use the mixing rule to calculate the constants $a(T)$ and b. The rule is in the form as follows:

$$a_{zp}(T) = \sum_i \sum_j x_i \cdot x_j \cdot \sqrt{a_i \cdot a_j} \cdot (1 - K_{ij}) \qquad (9)$$

$$b_{zp} = \sum_i b_i \cdot x_i \qquad (10)$$

For the larger number of gas components, it is more appropriate to use computer software for this type of computation. It is also due to the need for implementation of the binary interaction coefficients K_{ij}, which are given in (Knapp, H. et al., 1982).

3.2. Dynamic viscosity of pure gases at high pressures

Dynamic viscosity is considered to be constant up to the pressure below 1 MPa. Above the pressure, the viscosity increases with the pressure, whereas the most common method of its calculation is the Jossi-Stiel-Thodos method (Jossi, 1962). This indicates the dependence of the additional viscosity $(\eta - \eta_0)$ on the reduced density, which is defined by the ratio of the gas density at the determining conditions to the critical density (density at the critical pressure and critical temperature). The empirical relationship applies to the non-polar gases (CH4, CO2, N2, H2, etc.). It is valid in terms of the reduced densities $\rho_r \leq 3$ and is in the form:

$$(\eta - \eta_0) \cdot \xi_d = \left(0.506 \cdot e^{1.584 \cdot \rho_r} - 0.506 \right) \cdot 10^{-6} \qquad (11)$$

If the reduced density ranges $0.3 \leq \rho_r \leq 2$, the following applies:

$$(\eta - \eta_0) \cdot \xi_d = \left(1.0637 \cdot e^{1.079 \cdot \rho_r} - 1.15 \right) \cdot 10^{-6} \qquad (12)$$

The constant ξ_d is a function of the critical temperature T_k (K), critical pressure p_k (MPa) and the molar mass M (kg·kmol⁻¹) and is in the form:

$$\xi_d = \left(\frac{T_k}{M^3 \cdot p_k^4} \right)^{\frac{1}{6}} \qquad (13)$$

For polar gases (CO, HCl, H$_2$O), the empirical relationships obtained by experiments were classified according to the reduced density as follows:

$$\rho_r \leq 0.1 \qquad (\eta - \eta_0) \cdot \xi_d = 0.7619 \cdot 10^{-6} \cdot \rho_r^{1.111} \qquad (14)$$

$$0.1 \leq \rho_r \leq 0.9 \qquad (\eta - \eta_0) \cdot \xi_d = 2.793 \cdot (9.045 \cdot \rho_r + 0.63)^{1.739} \cdot 10^{-8} \qquad (15)$$

$$0.9 \leq \rho_r \leq 2.2 \qquad \log\{-\log[(\eta - \eta_0) \cdot \xi_d] - 2.3372\} = \\ = 0.6439 - 0.1005 \cdot \rho_r \qquad (16)$$

3.2.1. Dynamic viscosity of a mixture of gases

The Dean and Stiel method, which is designed for hydrogen-free and helium-free non-polar gases, can be used for the calculation of the viscosity of a mixture of gases:

$$(\eta - \eta_0) \cdot \xi_{dh} = 0.496 \cdot \left(e^{1.439 \cdot \rho_r'} - e^{-1.111 \cdot \rho_r'^{1.858}} \right) \qquad (17)$$

The constant ξ_{dh} is calculated similarly to the consideration ξ_d of the mean molar mass of a mixture of gases:

$$\xi_{dh} = \left[\frac{T_k}{\left(\sum x_i \cdot M_i \right)^3 \cdot p_k^4} \right]^{\frac{1}{6}} \qquad (18)$$

The reduced density of a mixture of gases is calculated based on the average specific critical volume of particular components by means of a weighted mole fraction:

$$\rho_r' = \rho \cdot \sum_i (x_i \cdot v_{ki}) \qquad (19)$$

3.3. Thermal conductivity of gases at high pressures

Thermal conductivity has the same properties as viscosity at low pressures. Its value is virtually unchanged with the changing pressure up to the pressure of 100 kPa. Thermal conductivity increases with the increasing pressure at a higher pressure (Heinrich, 1982).

Stiel and Thodos developed equations for different ranges of the reduced density based on the dimensional analysis:

$$\rho_r \leq 0.5 \qquad (\lambda - \lambda_0) \cdot \vartheta_d \cdot z_k^5 = 2.697 \cdot 10^{-4} \cdot \left(e^{-0.535 \cdot \rho_r} - 1 \right) \qquad (20)$$

$$0.5 < \rho_r \leq 2 \qquad (\lambda - \lambda_0) \cdot \vartheta_d \cdot z_k^5 = 2.523 \cdot 10^{-4} \cdot \left(e^{0.67 \cdot \rho_r} - 1.069 \right) \qquad (21)$$

$$2 < \rho_r \leq 2.8 \qquad (\lambda - \lambda_0) \cdot \vartheta_d \cdot z_k^5 = 0.5733 \cdot 10^{-4} \cdot \left(e^{1.555 \cdot \rho_r} - 2.016 \right) \qquad (22)$$

The relative error of these equations ranges from 10 to 20 %.

The dependence according to (Ullmann, 2005, Purcz, 2006) is an equation commonly used for calculation of the thermal conductivity of mixtures of gases of low density. It is in the form:

$$\lambda_{GM} = \sum_i \frac{\lambda_i}{1 + \sum_{j \neq i} 1.065 \cdot \Phi_{ij} \cdot \frac{x_j}{x_i}} \qquad (\text{W·m}^{-1}\text{·K}^{-1}) \qquad (23)$$

The constant Φ_{ij} is defined by the formula:

$$\Phi_{ij} = \frac{\left[1 + \left(\frac{\eta_{0,i}}{\eta_{0,j}} \right)^{\frac{1}{2}} \cdot \left(\frac{M_j}{M_i} \right)^{\frac{1}{4}} \right]^2}{\sqrt{8} \cdot \left[1 + \frac{M_i}{M_j} \right]^{\frac{1}{2}}} \qquad (24)$$

3.4. Computation of the heat capacity and implementation of the multi-dimensional regression

The calculation of thermal capacity at higher pressures is based on the differential equation (Heinrich, 1980, Rajzinger, 2012, Purcz, 2001):

$$\left(\frac{\partial c_p}{\partial p} \right)_T = -T \cdot \left(\frac{\partial^2 v}{\partial T^2} \right)_p \qquad (\text{m}^3\text{·kg}^{-1}\text{·K}^{-1}) \qquad (25)$$

By equation integration, we receive a relation by which it is possible, at known courses of state quantities, to calculate the thermal capacity at high pressures in the form:

$$c_{p_2} = c_{p_1} - \int_{p_1}^{p_2} T \cdot \left(\frac{\partial^2 v}{\partial T^2} \right)_p \, \mathrm{d}p \qquad (\text{J·kg}^{-1}\text{·K}^{-1}) \qquad (26)$$

With regard to the complexity of calculation of the compressibility factor needed for the calculation of specific volume and its second-order derivative according to the temperature at a constant pressure, it is favourable to use the numerical solution by means of Taylor expansion:

$$c_{p2} = c_{p1} - \frac{p_2 - p_1}{n} \cdot$$
$$\cdot \sum_{j=1}^{n} T \cdot \left[\frac{v_{i-1} - 2 \cdot v_i + v_{i+1}}{(\Delta T)^2} \right]_{p_1 + j \cdot \frac{p_2 - p_1}{n}} \qquad (\text{J·kg}^{-1}\text{·K}^{-1}) \qquad (27)$$

It is not possible to add an expression according to the relation (27) to the CFX simulation, as it requires to define only a simple function $c_p = \mathrm{f}(p,T)$. In case of creating dependence of the thermal capacity on pressure and temperature, it is necessary to analyse calculated values by multidimensional regression in the programme MPGM. For approximation of a physical quantity depending on pressure and temperature, a linear model was selected with a form of an approximated function:

$$c_p = a_1 + a_2 \cdot p + a_3 \cdot T + a_4 \cdot p \cdot T +$$
$$+ a_5 \cdot p^2 + a_6 \cdot T^2 \qquad (\text{J·kg}^{-1}\text{·K}^{-1}) \qquad (28)$$

After generating the table with calculated values of a physical quantity, the programme will calculate coefficients a_1 to a_6 on the

basis of the method of least squares. By using this method, it is necessary to reach a minimum sum of squares of deviations between the real values and an approximated function given by the relation:

$$s = \sum (a_1 + a_2 \cdot p + a_3 \cdot T + $$
$$+ a_4 \cdot p \cdot T + a_5 \cdot p^2 + a_6 \cdot T^2 - c_p)^2 \qquad (\text{J}^2\text{·kg}^{-2}\text{·K}^{-2}) \qquad (29)$$

In order to meet the condition of the least deviation s, it is necessary to differentiate the function according to all sought coefficients:

$$\frac{\partial s}{\partial a_i} = 0 \qquad (30)$$

For example, it is possible to write for the coefficient a_4 on the basis of the relation (30):

$$\frac{\partial s}{\partial a_4} = 2 \cdot \sum (a_1 + a_2 \cdot p + a_3 \cdot T + a_4 \cdot p \cdot T +$$
$$+ a_5 \cdot p^2 + a_6 \cdot T^2 - c_p) \cdot p \cdot T = 0 \qquad (31)$$

By differentiation and modification according to all coefficients a_1 to a_6, it is possible to create the system of linear equations written in the matrix form as follows:

$$\begin{vmatrix} n & \sum p & \sum T & \sum p \cdot T & \sum p^2 & \sum T^2 \\ \sum p & \sum p^2 & \sum p \cdot T & \sum p^2 \cdot T & \sum p^3 & \sum p \cdot T^2 \\ \sum T & \sum p \cdot T & \sum T^2 & \sum p \cdot T^2 & \sum p^2 \cdot T & \sum T^3 \\ \sum p \cdot T & \sum p^2 \cdot T & \sum p \cdot T^2 & \sum p^2 \cdot T^2 & \sum p^3 \cdot T & \sum p \cdot T^3 \\ \sum p^2 & \sum p^3 & \sum p^2 \cdot T & \sum p^3 \cdot T & \sum p^4 & \sum p^2 \cdot T^2 \\ \sum T^2 & \sum p \cdot T^2 & \sum T^3 & \sum p \cdot T^3 & \sum p^2 \cdot T^2 & \sum T^4 \end{vmatrix} \cdot \begin{vmatrix} a_1 \\ a_2 \\ a_3 \\ a_4 \\ a_5 \\ a_6 \end{vmatrix} = \begin{vmatrix} \sum c_p \\ \sum p \cdot c_p \\ \sum T \cdot c_p \\ \sum p \cdot T \cdot c_p \\ \sum p^2 \cdot c_p \\ \sum T^2 \cdot c_p \end{vmatrix} \qquad (32)$$

The MPGM software uses also a programme unit for matrix adjustment by means of Gauss method of elimination during calculation. Fig. 9 shows the thermal capacity for a particular gas mixture composition (30 % H_2, 30 % N_2, 40 % CH_4). The function (for range 0 to 300 °C and 1 to 10 MPa) was created by regression analysis in the form:

$$c_p = 2399 + 6.131 \cdot 10^{-7} \cdot p - 1.78 \cdot T + 2.2196 \cdot 10^{-8} \cdot p \cdot T +$$
$$+ 5.919 \cdot 10^{-14} \cdot p^2 + 3.212 \cdot 10^{-3} \cdot T^2 \qquad (\text{J·kg}^{-1}\text{·K}^{-1}) \qquad (33)$$
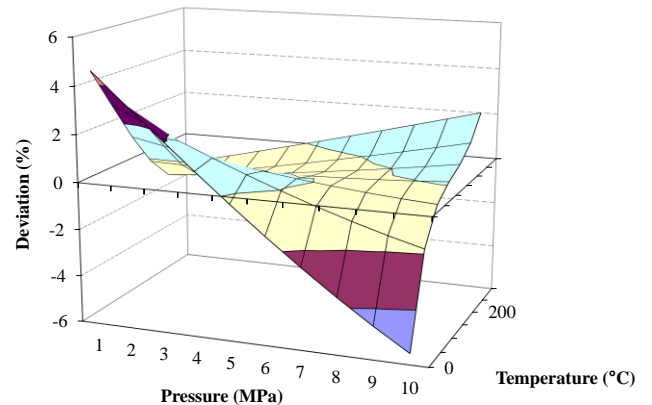

Fig. 10. Deviation between real and calculated value of the thermal capacity from regression analysis for the pressure range 1 to 10 MPa and the temperature range 0 to 300 °C

An average percentage deviation of calculated value cp according to (27) and (33) is on the level of 1 %. The least deviation

is 5.2 %, and when the range of temperatures and pressures is decreasing at approximation, the accuracy is increasing.

If it is necessary to obtain mathematical dependence of thermal capacity for the pressure range from 1 to 3 MPa and for the temperature range from 0 to 60 °C, the deviation between real values and values from the regression analysis is only up to 0.5 % (Fig. 11). The least deviations at mean values are reached from the temperature and pressure range at used form of the regression function according to (28). Table 1 shows the regression coefficients a1 to a6 of other physical quantities for model gas composition (30 % H2, 30 % N2, 40 % CH4) and the range 0 to 300 °C and 1 to 10 MPa.
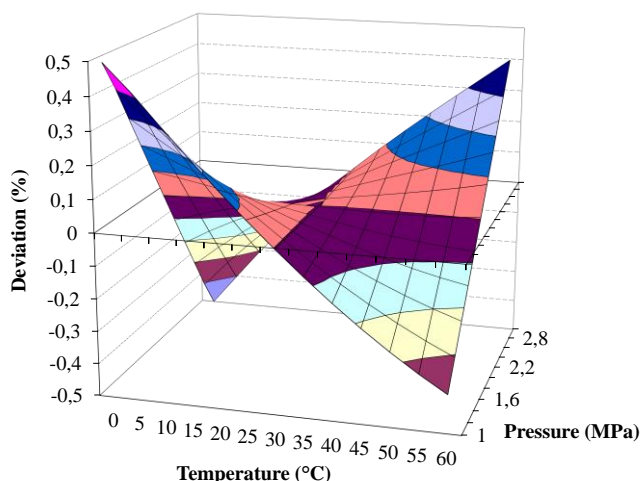

Fig. 11. Deviation between real and calculated value of the thermal capacity from regression analysis for the pressure range 1 to 3 MPa and the temperature range 0 to 60 °C

Tab. 1. Regression coefficients for selected physical quantities solved by the MPGM software

Physical quantity	a_1	a_2	a_3	a_4	a_5	a_6
Dynamic viscosity (kg·m⁻¹·s⁻¹)	4,554	$5,401 \cdot 10^{-9}$	$3,5025 \cdot 10^{-2}$	$2,309 \cdot 10^{-10}$	$4,257 \cdot 10^{-16}$	$-8,7318 \cdot 10^{-6}$
Compressibility factor (-)	0,79994	$-1,0102 \cdot 10^{-10}$	$8,1263 \cdot 10^{-4}$	$2,5849 \cdot 10^{-12}$	$-1,1717 \cdot 10^{-17}$	$-7,9707 \cdot 10^{-7}$
Thermal conductivity (W·m⁻¹·K⁻¹)	$17,99 \cdot 10^{-3}$	$1,5527 \cdot 10^{-11}$	$1,1709 \cdot 10^{-4}$	$9,8254 \cdot 10^{-13}$	$1,388 \cdot 10^{-18}$	$6,9015 \cdot 10^{-8}$
Thermal capacity (J·kg⁻¹·K⁻¹)	2399	$6,131 \cdot 10^{-7}$	-1,78	$2,2196 \cdot 10^{-8}$	$5,919 \cdot 10^{-14}$	$3,212 \cdot 10^{-3}$

It is possible to use such obtained courses of physical quantities for any gas mixture as input defining of material in the HTC-FC software. Export of equations directly into the file *.ccl* that is an input file of the ANSYS CFX programme enables the import of material properties of gas mixture. With regard to the fact that the simulation tool does not have to calculate material properties of each solved element for a long time, but it uses the approximation equations, the time needed for simulation gets short.

4. CONCLUSION

The introduction of numerical calculations into engineering method of solving various tasks becomes a necessary part of complex demands of the praxis. It is often necessary to realize solution in a relatively short time. I such a case, the designer engineer will welcome a supporting software that enables to facilitate and, especially, to speed up the whole process of solution of research as well as commercial tasks.

A full application of mentioned software requires its comprehensive treatment and tests at various types of set physical parameters. In case of the MPGM software, it is necessary to search approximation functions that describe physical properties of the gas mixtures better and more accurate and, therefore, minimize the deviations from real values.

Notations: $a_{1,2...}$ – regression coefficients; c_p – specific thermal capacity, J·kg⁻¹·K⁻¹; c_{p1} – specific thermal capacity at p_1, J·kg⁻¹·K⁻¹; c_{p2} – specific thermal capacity at p_2, J·kg⁻¹·K⁻¹; n – number of integral divisions, 1; p – pressure, Pa; p_1 – initial pressure, Pa; p_2 – final pressure, Pa; R – universal gas constant, J·mol⁻¹·K⁻¹; T – gas temperature, K; T_s – surface temperature, K; T_t – fluid temperature, K; V – molar volume, m³·mol⁻¹; z – compressibility factor, 1; v – specific volume, m³·kg⁻¹; α – free convection HTC, W·m⁻²·K⁻¹; α_c – total HTC, W·m⁻²·K⁻¹; ε – surface emissivity, 1; σ – Stefan-Boltzmann constant, W·m⁻²·K⁻⁴; ω – acentric factor.

REFERENCES

1. **Badida, M., Lumnitzer, E., Biľová, M., Fiľo, M.** (2008), *The uncertainties of environments parameters measurements as tools of the measurements quality improvement*, Univerzitet u Kragujevcu.
2. **Durdán M., Laciak, M., Kačur, J.** (2009), *Mathematical modelling of the UCG process*, AGH University of Science and Technology, Krakow, 407- 410.
3. **Ferstl, K., Masaryk, M.** (2010), *Heat transfer book*, STU Bratislava, 53- 63**.**
4. **Heinrich, J.** (1980), *Vlastnosti tekutín*, Alfa.
5. **Jossi, J. A., Stiel, L. I., Thodos, G.** (1962), The viscosity of pure substances in the dense gaseous and liquid phases, *AIChEJ*, 8,59.
6. **Kalaš, J., Lucskay, J., Vranayová, Z.** (2000), Air infiltrationnonsteady processes in dwelling rooms of apartments experimental research,Zeszyty naukowe Politechniki Rzeszowskiej, 32, Rzeszów, 157-163.
7. **Kapjor, A., Jandačka, J., Malcho, M., Papučík, Š.** (2010), Intensification of Heat Transport from the Floor Convector at Given Geometry and the Way of Use, *XXIX medzinárodná konferencia Setkání kateder mechaniky tekutin a termomechaniky*, 101- 104.
8. **Kizek, J., Lazič, L.** (1999), Simulation method for optimization of a mixture of fuel gases, *Metalurgija*, Vol. 38, No. 2, 109-113.
9. **Knapp, H. et al.** (1982), Vapor-Liquid Equilibria for Mixtures of Low Boiling Substances, *Chem. Data Ser.*, Vol. 6, DECHEMA.
10. **Mansoori, Z., Saffar-Avval, M., Tabrizi, B. H., Ahmadi, G.** (2002), Modeling of heat transfer in turbulent gas–solid flow, *International Journal of Heat and Mass Transfer*, Vol. 45, No. 6, 1173- 1184.
11. **Michalec, Z., Taraba, B., Bojko, M., Kozubková, M.** (2010), CFD modelling of the low-temperature oxidation of coal, *Archivum Combustions*, Vol. 30, No. 3, 133-144.

12. **Oravec, M., Števo, S., Sekaj, I.** (2010),Comparison of Using Simple Genetic Algorithm and Parallel Genetic Algorithm in Heat Transfer Model Optimization, *Journal of Cybernetics and Informatics*. Vol. 9, 13-18.

13. **Purcz, P.** (2001), Parallel algorithm for spatially one- and two-dimensional initial-boundary-value problem for a parabolic eauation, *Kybernetika*, Vol. 37, no. 2, 171-181

14. **Purcz, P.** (2006) Communication complexity and speed-up in the explicit difference method. Parallel Processing Letters. Vol. 16, no. 3, 313-321

15. **Pyszko, R.**, **Příhoda, M., Velička, M.** (2010), Method for determining the thermal boundary condition in the CC mould for numeric models, *In Proceedings of 19 conference METAL*, Ostrava.

16. **Rajzinger, J.** (2012), Calculation of maximum water content in various natural gases by using modified Peng-Robinson equation of state, *Communications*, Vol. 14, No. 4A, s. 29-35.

17. **Setoodeh, N., Rahimi, R., Ameri, A.** (2011), Modeling and determination of heat transfer coefficient in a basin solar still using CFD, *Desalination*, Vol. 268, No. 1–3, 103-110.

18. **Svoboda, A. a kol.** (2007), *Plynárenská příručka*, Gas Praha.

19. **Tauš, P.**, **Kudelas, D.** (2012), Počítačové modelovanie prevádzkových parametrov prototypov slnečných vzduchových kolektorov na báze recyklovaných plastov, *TechCON Magazín*, Vol. 8, No. 3, 37-40.

20. **Tkáč, J.**, **Hvizdoš, M**. (2008), *Metán hydrát a jeho využitie na energetické účely*, ALER Žilina: EDIS, 53-59

21. **Trebuňa, P.**, **Kliment, M., Halčinová, J., Fiľo, M., Markovič, J.** (2013), Developments in field of data processing through PDM, PLM and the use of system Teamcenter nowadays, *Sborník příspěvků*: 3, Valtice. – Plzeň, SmartMotion, 2013, 190-194.

22. **Ullmann, F.** (2005), *Ullmann's Chemical Engineering and Plant Design*, Vol. 1-2, John Wiley & Sons.

23. **Vranay, F.**, **Vranayová, Z**. (1999), One-pipes systems hydraulic regulation, *Systemy a technologie ogrzewania budynków*, Solina, 225-230.

TEMPERATURE DEPENDENCY OF FRACTURE TOUGHNESS OF HIGH-STRENGTH FERRITIC STEEL HARDOX-400

Ihor DZIOBA[*], Robert PAŁA[*], Tadeusz PAŁA[*]

[*]Department of Machine Design Fundamentals, Faculty of Mechatronics and Machine Design, Kielce University of Technology,
Al. 1000-lecia PP 7, 25-314 Kielce, Poland

pkmid@tu.kielce.pl, probertrobert@gmail.com, tadeusz.pala@gmail.com

Abstract: The paper presents experimental results of the changes of strength and fracture toughness characteristics of high-strength ferritic steel Hardox-400 in the temperature range from -100 OC to +20 OC. It has been shown that the strength characteristics values increase linearly with lowering the temperature. Changes of fracture toughness characteristics from temperature are more complex and they are dependent on thickness of the tested specimens.

Key words: High-Strength Ferritic Steel, Strength Characteristics, Fracture Toughness, Master Curves

1. INTRODUCTION

Ferritic steels are used for construction elements in various industries – construction in building, energetics, construction machinery and other. The widespread use of ferritic steels requires knowledge of strength characteristics and fracture toughness in temperature ranges in which they are going to be operated. Extensive studies of ferritic steels characteristics of yield stress value $200 < \sigma_y < 820$ (MPa) have been carried out by Wallin with his cooperators (ASTM E 1820-05, 2000; Wallin et al., 1984, 2004; Wallin, 1984, 2002)). Accordingly to the researches, the dependencies of the change of strength characteristics, impact and fracture toughness from the temperature have been determined. The conception of the Master Curve determination has been presented, which allows to evaluate fracture toughness in ferritic steel in areas of low plateau and transition region. On the basis of the proposed concept, the standard ASTM E1921 has been worked out (ASTM E1921-05, 2005). The concept of Master Curve was also used in the procedures of evaluation strength of the construction elements SINTAP (1999) and FITNET (FITNET, 2008; Neimitz et al., 2008).

Modern technologies allow to perform ferritic steel products, in which the yield strength is significantly higher than σ_y =820 MPa. Therefore, the question arises whether the concept of the Master Curve prepared on the basis of the traditional ferritic steels can be directly applied to the modern, high- strength ones? Based on the researches carried out on the steel specimens S960Q (σ_y > 960 MPa), it has been stated that certain modifications should be implemented during preparation of the Master Curve for this steel [5].

In this article, the experimental results obtained during tests of steel Hardox-400 have been presented. The influence of the tests temperature in the range from -100 to +20 OC on the strength characteristics and fracture toughness of different thickness specimens have been shown.

2. MATERIAL, RESEARCH METHODS

Steel Hardox-400 is a low alloy steel of ferritic matrix. Chemical composition is given in Tab. 1. During the manufacture of steel it is thermo-mechanically treated to give the microstructure of tempered bainite-martensite (Fig. 1) having a hardness of about 400HV. Specimens (12x24x116 mm) were cut out of the plate of 30 mm thickness. Hardness distribution in the direction of the plate thickness is shown in the figure 2a. Since the hardness varies in thickness, the specimens for determining the fracture toughness, SENB were cut so, that the initial crack tip was located in the centre of the thickness plate (Fig. 2b). Specimens for the uniaxial tension test to determine the characteristics of the material were also collected from the central part of the plate.

Tab. 1. Chemical composition of the steel Hardox-400 (in mas. %)

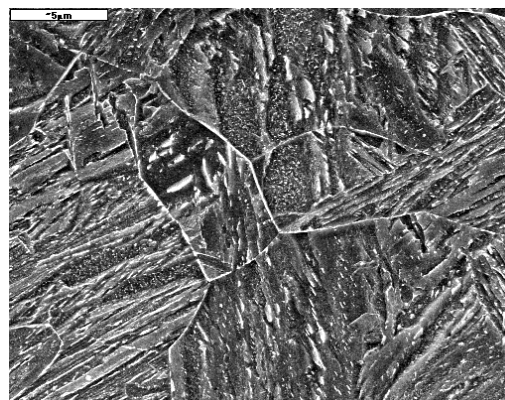|	C	Si	Mn	P	S	Cr	Ni	Mo	B
Hardox-400	0.12	0.52	1.25	0.01	0.001	0.66	0.04	0.012	0.001

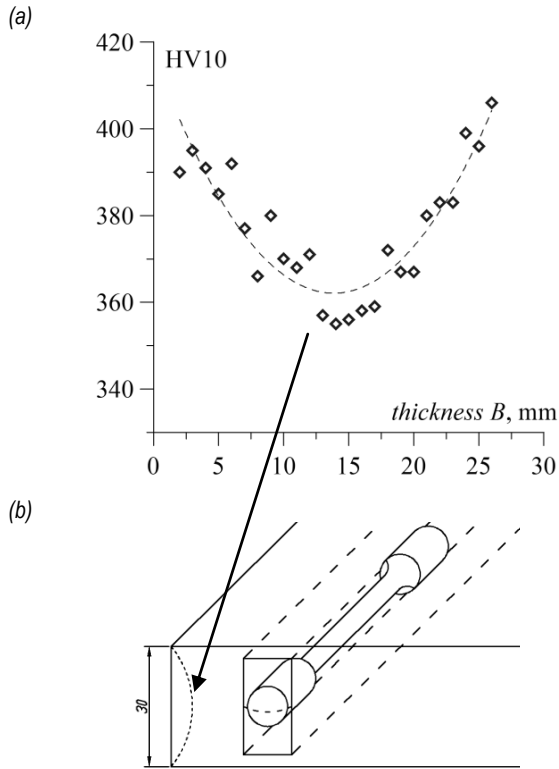**Fig. 1.** The microstructure of the steel Hardox-400, 5000x

(a)

(b)

Fig. 2. *a)* hardness distribution along the thickness of the plate; *b)* the scheme of cutting uniaxially tensioned specimens and three-point bend specimens

The researches were carried out on the universal testing machine MTS-250 equipped in the automated control system and data record in the temperatures range from -100 ºC to +20 ºC. The tests in the minus temperatures were carried out in a thermal chamber in the evaporated nitrogen environment. The accuracy of maintaining the desired temperature during the test was ±0.5 ºC. The uniaxial tension tests were carried out on standard fivefold specimens. The signals of force, *P,* and elongation of the measuring part of the specimen, *u,* were recorded in real time.

Fracture toughness characteristics were determined on the three-points bend specimens with one-side notch (SENB, 12x24x110 mm, a_0/W=0.5) according to the standard ASTM E1820-05 [1]. The signals of force, *P,* specimen deflection at the load point, u_{ext}, crack opening, u_{COD}, and potential change, *U,* were recorded during fracture toughness determination. In the case of ductile fracture mechanism, the critical value of J integral, J_{IC}, was determined on each single specimen using the potential change method to determine the crack growth and to draw up the J_R-curve [1,2]. In the case of brittle fracture, preceded by plasticity area in front of the crack tip, the critical value of the J integral, J_C, was calculated according to the formula:

$$J_C = \frac{2A_C}{B(W-a_0)} \qquad (1)$$

where: A_c is deformation energy at the moment of cracking, calculated on a basis of the graph $P = f(u_{ext})$; a_0 is total crack length, notch plus fatigue pre-crack. The critical values of the J, J_C integral were converted into units of the stress intensity factor:

$$K_{JC} = \sqrt{\frac{J_{IC}E}{(1-\nu^2)}} \qquad (2)$$

where: *E is* Young's modulus, ν- is Poisson's ratio.

3. STRENGTH CHARACTERISTICS

Sample graphs for the testing temperature *T*= -20 ºC of the stress-strain curves (σ-ε) are shown in the figure 3. The graphs of the real σ-ε were made to the moment where becomes apparent a maximum force value, taking into account the constant volume of the measuring part of the specimen.
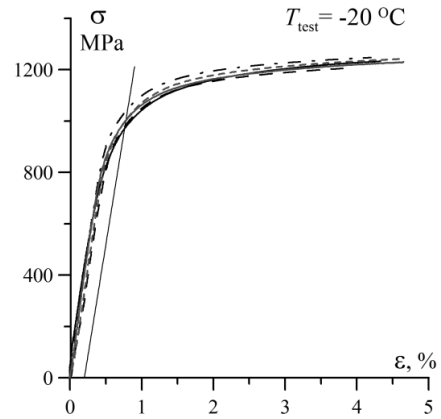

Fig. 3. The example of a σ-ε graphs for the steel Hardox-400
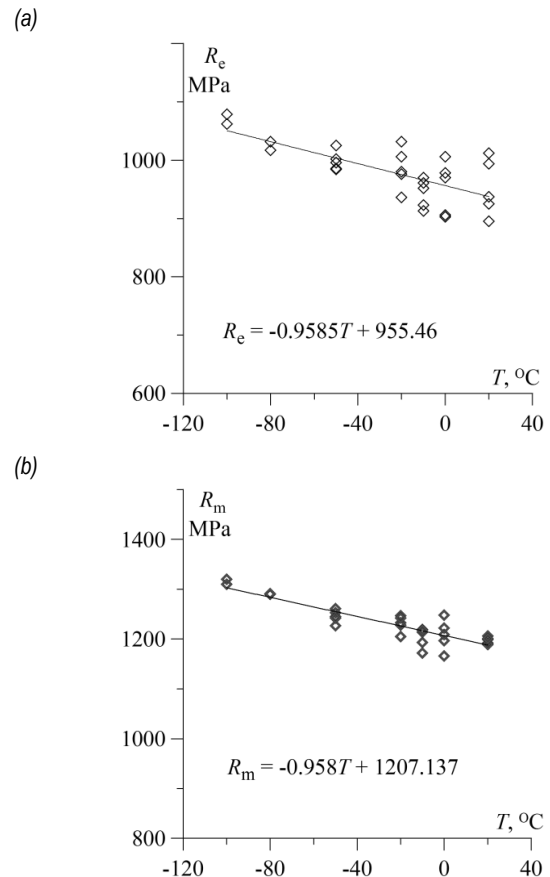
(a)

(b)

Fig. 4. The change of the strength characteristics depending on the test temperature: *a)* R_e; *b)* R_m

In Fig. 4, are shown tendencies of the change of strength characteristics, R_e and R_m, from the test temperature: increase of these values with lowering the temperature causes. This in-

crease is steady, it can be shown by means of the linear function. The largest data scatter was observed in the temperature range [-20; +20] °C. The change tendencies of the Young's modulus, *E,* strain values for steady extension, $\varepsilon(R_m)$ and the values of total relative extension A_5 are similar. For all these values was noted increase together with lowering the temperature, which can be described by means of linear functions:

$$R_e = -0.9585T + 955.46 \tag{3}$$

$$R_m = -0.9585T + 1207.137 \tag{4}$$

$$E = -0.00912T + 181.085 \tag{5}$$

$$\varepsilon(R_m) = -0.011T + 4.297 \tag{6}$$

$$A_5 = -0.0185T + 15.718 \tag{7}$$

Only the values of relative restrict of the cross-section of the specimen slightly decrease with lowering the temperature.

4. FRACTURE TOUGHNESS

Critical values of fracture toughness were determined on the specimens of the thickness *B*, from 1 to 24 mm in the temperatures range [-100; +20] °C. K_{JC} changes depending on the test temperature of the selected thickness of the tests are shown in Fig. 5. Similarly, as for the strength characteristics for fracture toughness, has large scatter of data. The largest data scattering occurs in the transition region, where cracking mechanism changes from the cleavage fracture to the plastic one (Fig. 5). Fig. 6a presents dependencies of the critical value of fracture toughness K_{JC} from temperature for the specimens of thickness from the range 1÷12 mm. The fracture toughness was determined on specimens with thickness $B \geq 8$ mm generally gradually decreases slightly with increasing thickness for the corresponding test temperature (Fig. 6a). For thickness $B \leq 4$ critical values of fracture toughness remain almost constant level to a certain temperature, then K_{JC} were decreases, caused by changes in the mechanism of crack propagation from plastic to ductile-brittle. In the specimens of thickness $B = 4$ mm the decrease of fracture toughness was observed at the temperatures lower than -10 °C. Reduction in thickness also lowers the temperature at which the crack propagation mechanism changes. For specimens of the thickness $B \leq 2$ mm is a temperature lower -50 °C.

Fig. 6b presents the change dependencies of the fracture toughness critical value, K_{JC}, on *B* thickness. Dependency course points to the irregular change shape K_{JC} from *B* at each tested temperature. In the dependencies for a suitable temperature occurs a maximum achieved at some thickness characteristic. From the maximum point, K_{JC} values decrease with the specimen thickness. Reducing the thickness of the specimen below value, at which the maximum occurs, causes a rapid reduction in the critical value of fracture toughness. With increasing thickness of the specimen, above the corresponding maximum, the K_{JC} values also reduce, but less rapidly. Along with the lowering of the test temperature, dependencies are located below, maintaining its characteristic shape, and maximum point descends and moves towards the thickness reduction side.
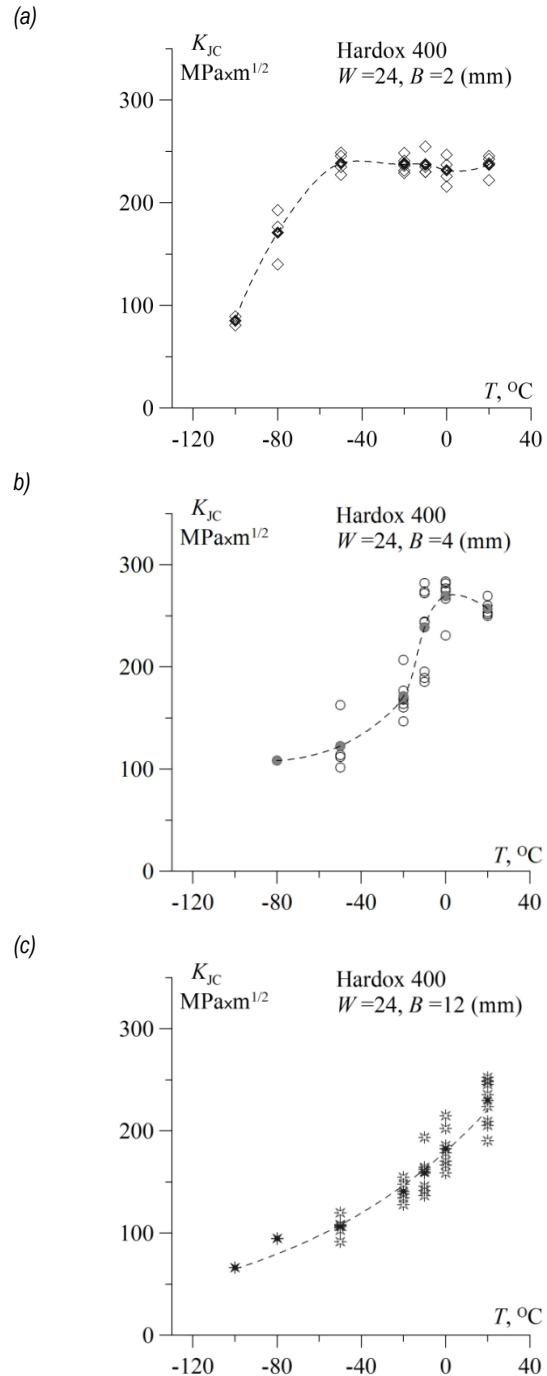
(a)

b)

(c)

Fig. 5. K_{JC} - *T* dependency for the specimens of thickness *B*: *a)* 2 mm; *b)* 4 mm; *c)* 12 mm

Specimen thickness, *B*, necessary for the dominance of plane strain during determination of K_{IC} critical value, is determined from the dependence (ASTM E 1820-05, 2000):

$$B \geq B_K = 2.5 \left(\frac{K_C}{\sigma_y} \right)^2 \tag{8}$$

However, the plane strain dominance during JIC determination is assured for the specimens of the B thickness, determined from the connection (ASTM E 1820-05, 2000):

$$B \geq B_J = \alpha \frac{J_C}{\sigma_y} \tag{9}$$

In the formulas (8) and (9) σ_y is yield stress, $\alpha = 25$ for the bent specimens or $\alpha = 175$ for the tensioned specimens.

ness for ferritic steel, $K_{min} = 20$ MPa·m$^{1/2}$ (ASTM E1921-05, 2005; Wallin et al., 2004, Wallin, 2002).

The change dependency KJC on B in the range, where the condition (9) is satisfied, was described by means of the function (10) (solid lines on the graph Fig. 6b). The dashed line shows the spaces in which are located the dispersions towards the central trend, they do not exceed ±10%.

5. SUMMARY

As a result of the research it has been shown that the strength characteristics R_e and R_m, Young's modulus, E, strain values for steady extension, $\varepsilon(R_m)$, and the values of total relative extension, Z, increase along with lowering the research temperature. Change of these values can be described by means of the linear function ((3)-(7) formulas). Changes of fracture toughness characteristics from temperature are more complex and they are dependent on thickness of the tested specimens. In thickness range of the specimens, which satisfies the condition (9), fracture toughness dependency on thickness for a chosen temperature can be described by the function of type (10). Results, contained in this article, are the first part of a larger research aimed at experimental-numerical analysis of the steel cracking process including microstructural factors.
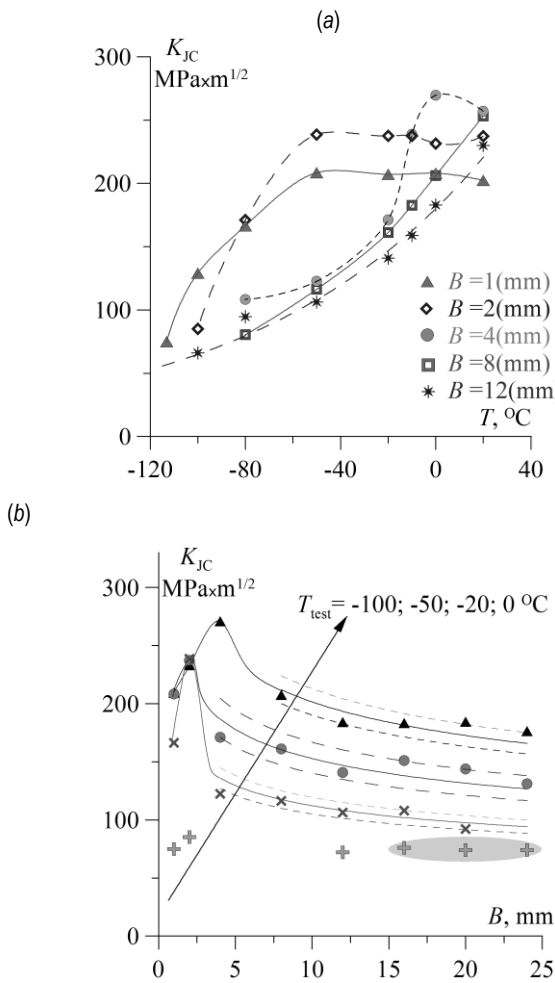
Fig. 6. K_{JC} dependencies: *a)* on the *T* test temperature for specimens of various thickness *B*; *b)* on thickness *B* for the various T

Differences of specimens thickness required according to the conditions (8) and (9) are big: $B_J/B_K \approx 15 \div 60$. From all specimens presented in the article, the condition (8) satisfies only specimens of the thickness $B > 16$ mm, tested at the temperature $T = -100\ ^\circ$C (shaded area in the Fig. 6b). There is much more specimens, which thickness corresponds to the condition (9). For the test temperature $T = 0\ ^\circ$C are specimens of thickness $B \geq 8$ mm, for $T = -20$ and $-50\ ^\circ$C are specimens – $B \geq 4$ mm.

The dependencies shown in the fig. 6b indicate that the critical value of fracture toughness, K_{JC}, is not constant value, K_{JC} decreases along with specimen thickness increase. On the basis of statistical researches for ferritic steels ($\sigma_y < 820$ MPa) has been proposed formula, which describes the change of the K_{JC} on the specimen thickness, B (ASTM E1921-05, 2005; Wallin et al., 2004, Wallin, 2002):

$$K_{JC(B_1)} = K_{min} + \left(\frac{B_2}{B_1}\right)^{\frac{1}{4}} \left(K_{JC(B_2)} - K_{min}\right) \qquad (10)$$

where: $K_{JC(B_1)}$ and $K_{JC(B_2)}$ are the critical values of fracture toughness for the specimens of thickness B_1 and B_2 ($B_1 > B_2$), respectively; K_{min} is the minimum critical value of fracture tough-

REFERENCES

1. **ASTM E 1820-05** (2000), *Standard Test Method for Measurement of Fracture Toughness*. ASTM; Philadelphia.
2. **ASTM E1921-05** (2005),*Test Method for Determination of Reference Temperature T0 for Ferritic Steels in the Transition Range*, ASTM, Philadelphia.
3. **FITNET** (2008), *Fitness – for – Service. Fracture – Fatigue – Creep – Corrosion*, Edited by M. Koçak, S. Webster, J.J. Janosch, R.A. Ainsworth, R. Koerc.
4. **Neimitz A., Dzioba I., Graba M., Okrajni J.** (2008), Assessment of the strength, durability and safety of the structural components containing defects, *Kielce University of Technology* (in Polish).
5. **Neimitz A., Dzioba I., Limnell T.** (2012), Master Curve of ultra high strength steel, *International Journal Pressure Vessels and Piping*; Vol. 92,19-26.
6. **SINTAP** (1999), *Structural Integrity Assessment Procedure for European Industry*, Project No Be95-1426, British Steel.
7. **Wallin K, Nevasmaa P, Laukkanen A, Planman T.** (2004), Master Curve analysis of inhomogeneous ferritic steels, *Engineering Fracture Mechanics*; Vol.71, 2329-2346.
8. **Wallin K.** (1984), The Scatter in K$_{IC}$ Results, *Engineering Fracture Mechanics*. Vol. 19, 1085-1093.
9. **Wallin K.** (2002), Master curve analysis of the "Euro" fracture toughness dataset, *Engineering Fracture Mechanics*; Vol. 69, 451-481.
10. **Wallin K., Saario T., Törrönen K.** (1984), Statistical Model for Carbide Induced Brittle Fracture in Steel, *Metal Science*, Vol.18, 13-16.

STRENGTH AND FRACTURE TOUGHNESS OF THE WELDED JOINTS
MADE OF HIGH-STRENGTH FERRITIC STEEL

Ihor DZIOBA*, **Tadeusz PAŁA***, **Ilkka Valkonen****

*Department of Machine Design Fundamentals, Kielce University of Technology,
Aleja 1000-lecia Państwa Polskiego, 7, 25-314 Kielce, Poland
**Rautaruukki Oyj, R&D Centre, Harvialantie 420, Hameenlinna, Finland

pkmid@tu.kielce.pl, tadeusz.pala@gmail.com, Q0782.rrsteel@ruuki.com

Abstract: The paper presents experimental results of the characteristics of strength and fracture toughness of the material from the different zones of welded joints made of different participation of the linear welding energy. Strength characteristics and fracture toughness were determined in the weld material, in the area of fusion line, in the material of the heat affected zone and in the base material.

Key words: High-Strength Ferritic Steel, Welded Joints, Strength and Fracture Toughness Characteristics for Welded Joints Material

1. INTRODUCTION

In order to increase competitiveness and to meet the requirements that are specified by the customer, the companies produce steels with favorable operating parameters (Porter, 2006). These steels are characterized by properties of high strength, hardness, wear resistance. The high level properties of the steel can extend the life-time of components, reduce the frequency and cost of replacement parts to be used, which leads to increased safety during operation of the equipment.

To fully utilize and apply the high-strength ferritic steel in structures and mechanisms is necessary to take into account the issue of its weldability. Welded joints in terms of strength are places where there is a heightened risk of the occurrence of damage, due to the different microstructures of the material in the different zones of the joints (Tasak and Ziewiec, 2006), the presence of micro-defects and welding residual stress and the geometric factor, which causes the joint to be treated as a kind of stress concentrators (FITNET, 2008; Neimitz et al., 2008). Obtaining a proper strength of the welded joint, if the base material is high-strength steel, is a difficult task to accomplish. Technology selection and filler material should be provided, so that the material characteristics in all of zones of the welded joints, were similar to the base material characteristics.

This paper presents the results of experiments carried out on the material of two types of joints, made of high-strength ferritic steel S960QC, in which the welding process had different linear energy of welding - 0.7 kJ/mm and 1.2 kJ/mm. The measurements of hardness, strength characteristics were determined and the fracture toughness critical value of the material from the different zones of welded joints.

2. MATERIALS AND RESEARCH METHODS

Joints are made of sheet metal with a thickness of 8 mm high-strength ferritic steel S960QC. Chemical composition is given in

Tab. 1. As a result of thermo-mechanical processing steel obtains fine-grained microstructure of bainite-martensite (Fig. 1a) with a hardness of ≥ 350 HV10 and strength characteristics: $R_e \geq 960$ MPa, $R_m \geq 1000$ MPa. As a result of welding carried out with a linear speed of 1.2 kJ/mm (A) and a linear speed of 0.7 kJ/mm (B) in the welds was fine ferrite microstructure (Fig. 1b) and martensite (Fig. 1c). Hardness distributions were measured on the cross-section of the joint along the horizontal and vertical measuring lines (Fig. 2a) according to the Vickers's method at the load of 10 N, with a frequency of every 1mm.

Tab. 1. Chemical composition (in mass %)

	C	Si	Mn	P	S	Ti	Cr	Ni	Mo	V	Cu
S960-QC	0.11	0.25	1.20	0.020	0.010	0.07	CEV=C+Mn/6+(Cr+Mo+ V)/5+ (Cu+Ni)/15				

Strength characteristics of the tested joints were determined in the uniaxial tension test on a modernized testing machine UTS-100, equipped in the automated control system and results recording. Uniaxial tension test was carried out on the fivefold, flat specimens, cut out from the appropriate zones of the welded joint, along the weld axis (Fig. 2b). References from A1 to A4 correspond respectively to the specimens cut out from the weld material (WM), heat affected zone of the material at the fusion line (HAZFL), heat affected zone at the end of the normalization zone (HAZN), material at the end of the heat affected zone (HAZE) and base material (BM). During the uniaxial tension tests performance, *P* force signals and extension of the measuring part of the specimen, u_{ext}, were recorded in time.

Fracture toughness was determined on SENB specimens of dimensions: 8x16x64 mm (a_0/W =0.5) on MTS-250 testing machine, equipped with the automated control system and results recording. The a_0 is crack length, which include notch and fatigue pre-crack. The planes a_0 are placed according to A1-A4.

Tests at the minus temperatures were performed in a thermal chamber in the evaporated nitrogen environment. Accuracy

of maintaining the set temperature during test was ±0.5 °C. During fracture toughness determination the load signal, *P,* specimen diffraction at the load point, u_{ext}, crack opening u_{COD} and potential change, *U* were recorded in time. Critical value of fracture toughness was determined according to the ASTM E1820-05 (2000).
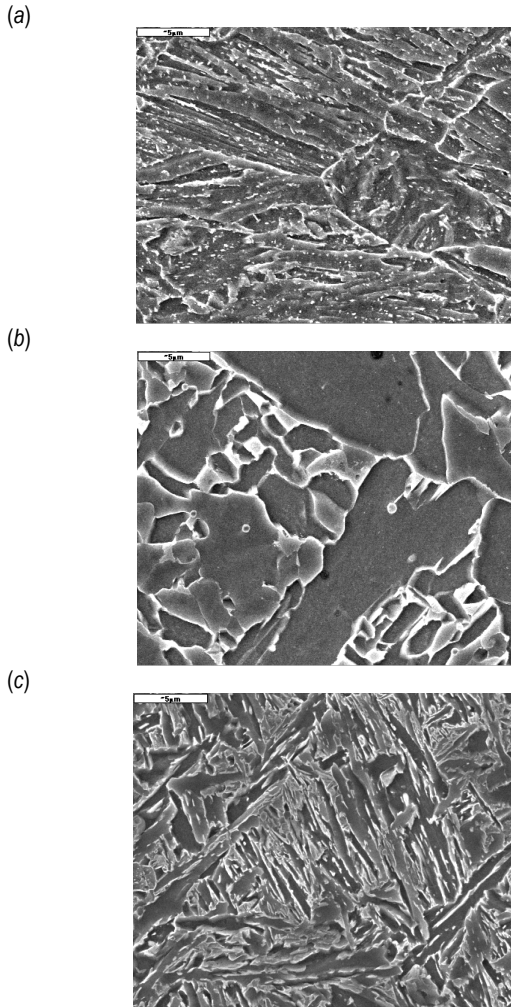
(*a*)

(*b*)

(*c*)

Fig. 1. Microstructure: a) – base material; b) – weld material in joint A;
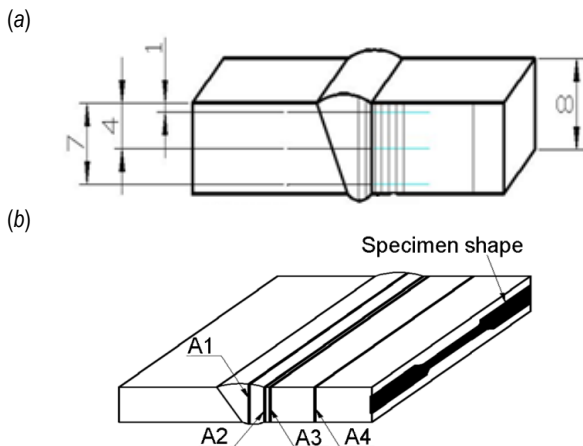c) – weld material in joint B

(*a*)

(*b*)

Fig. 2. Schemes: a) of hardness measuring in the cross- section
of the joint; b) – of selecting the specimens to determine strength
characteristics from the joint zones

In the case of ductile fracture mechanism, the critical value of J integral, J_C, was determined on a single specimen using of the potential change method to determine the crack growth and to draw up the J_R-curve [1]. In the case of brittle fracture, preceded by plasticity area in front of the crack tip, the critical value of the J integral was calculated according to the formula:

$$J_C = \frac{2A_C}{B(W-a_0)} \tag{1}$$

In eq. (1) A_c is deformation energy at the moment of cracking, calculated on a basis of the graph $P = f(u_{ext})$.

The critical values J_C were converted into units of the stress intensity factor:

$$K_{JC} = \sqrt{\frac{J_C E}{(1-\nu^2)}} \tag{2}$$

where: E *is* Young's modulus, ν- is Poisson's ratio.

3. TESTS RESULTS

The hardness distribution for joints with linear welding energy (LWE) 1.2 kJ/mm is shown in figure 3a. The lowest hardness (~170 HV10) is observed in the weld material. With increasing distance from the axis of the weld hardness gradually increases reaching a value of 360-370 HV10 in the base material. In the joint of LWE = 0.7 kJ / mm, weld material hardness is close to the level of the weld material (Fig. 3b). The minimum level of hardness (~250 HV10) was recorded in the material HAZFL. Next, with increasing distance from the axis of the weld showed a gradual increase in hardness of the material to a level corresponding to the base material. Vertical lines marked the place, where the notches are made in the SENB specimens for determining fracture toughness. From these places also were cut out the flat specimens to determine the strength characteristics (sch. 2b).
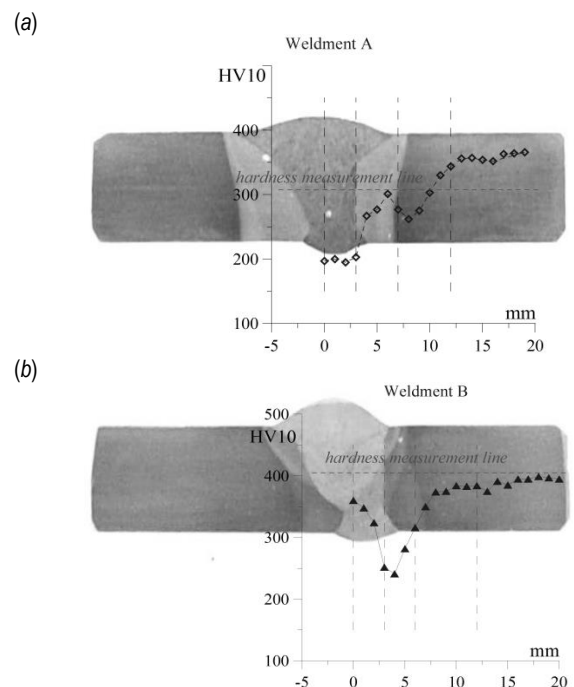
(*a*)

(*b*)

Fig. 3. Hardness distributions of the welded joints A (*a*) and B (*b*)

The change of hardness in the thickness direction of the joints A and B are shown in the fig. 4. In the weld material of the joint A hardness increases slightly from the face to the root (Fig. 4a). In the zone with distance 8 mm from the axis of the weld the nature of the hardness change is not regular. In the zones which are located at a distance from the axis of 8-18 mm, the hardness value remains approximately constant at thickness, and increases along with the distance from the weld. At a distance of more than 18 mm from the weld axis a significant change in hardness was not observed, indicating no thermal effect on the base material.

In the joint B hardness distributions in the weld material are comparable to the base material (Fig. 4b). The lowest level of hardness was observed in the material near the fusion line. Next, as the distance from the weld, hardness in areas increases and at 10 mm reaches a level appropriate to the base material.
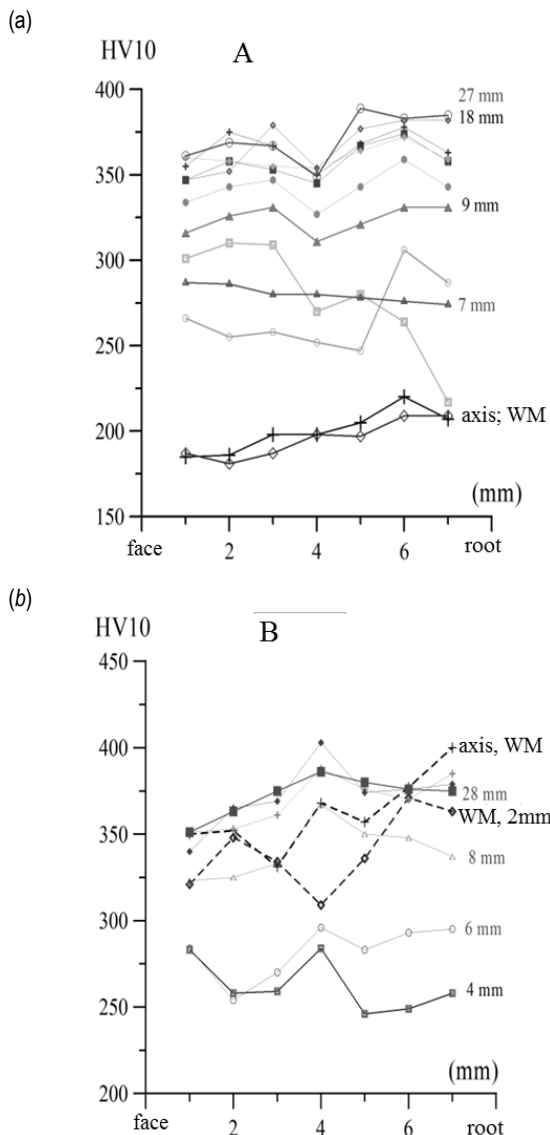
(a)

(b)

Fig. 4. Distribution of hardness in the thickness direction:
(a) joint A; (b) joint B

The measurements of hardness helped to establish the width of the heat affected zone in the joints: in the joint A (LWE= 1.2 kJ/mm) it is twice more than in the joint B (LWE= 0.7 kJ/mm). Measurements of hardness allowed to determine in the joints the

zones of low hardness, which is expected to be a low level of strength characteristics. On the basis of hardness measurements were selected areas, in which mechanical properties and fracture toughness would determined.

For the joint A (LWE = 1.2 kJ / mm) the lowest yield stress, R_e, and ultimate strength, R_m, at the same time of the highest elongation value, $\varepsilon(R_m)$, obtained in the weld material (Tab. 2). In the following zones the strength characteristics values of R_e and R_m increase, and the level of $\varepsilon(R_m)$ decreases. In the case of the joint B, (LWE = 0.7 kJ/mm) the lowest level of strength characteristics, R_e and R_m, and the highest $\varepsilon(R_m)$ has HAZFL material (Table 2). For WM, HAZN level of R_e and R_m increases, and $\varepsilon(R_m)$ - decreases. The highest levels of R_e and R_m at the lowest $\varepsilon(R_m)$ in both joints correspond to the HAZE material. The results shown in Tab. 2 demonstrate that the welding regime B allows to higher strength characteristics of material for all areas of joint, than the of regime A.

Tab. 2. The mechanical properties of welded joints materials

| | | Linear welding energy | | | | | | |
| | | A: LWE=1.2 kJ/mm | | | | B: LWE=0.7 kJ/mm | | |
Joint zone	BM	WM	HAZFL	HAZN	HAZE	WM	HAZFL	HAZN	HAZE
E, (GPa)	185	190	192	193	190	178	187	185	191
R_e, (MPa)	1005	535	607	670	1125	850	678	963	1183
R_m, (MPa)	1090	667	728	862	1180	1090	912	975	1208
n	55	13.3	16.37	13.16	85	14.2	11.33	123	111
$\varepsilon(R_m)$, (%)	3.1	16	8.5	5.8	2.5	5.1	6.2	2.7	2.2

Dependency of strength characteristics changes of R_e and R_m on hardness are shown in the Fig. 5. Based on the dependencies, which shown in the Fig. 5, one can evaluate the level of strength characteristics in every area of the welded joint with just the measurement of hardness.
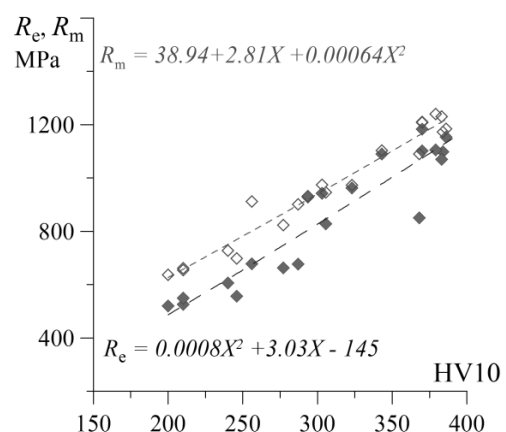

Fig. 5. The change of strength characteristics on hardness

Depending on the critical values of fracture toughness K_{JC} of test temperature for the material from different weld joints A and B shown in Figs. 6a and 6b, and for the base material in Fig. 6c. At room temperature the weld material in the joint A, with microstructure of fine ferrite (Fig. 1b), has high fracture toughness (~ 300 MPam$^{1/2}$, Fig. 6a).
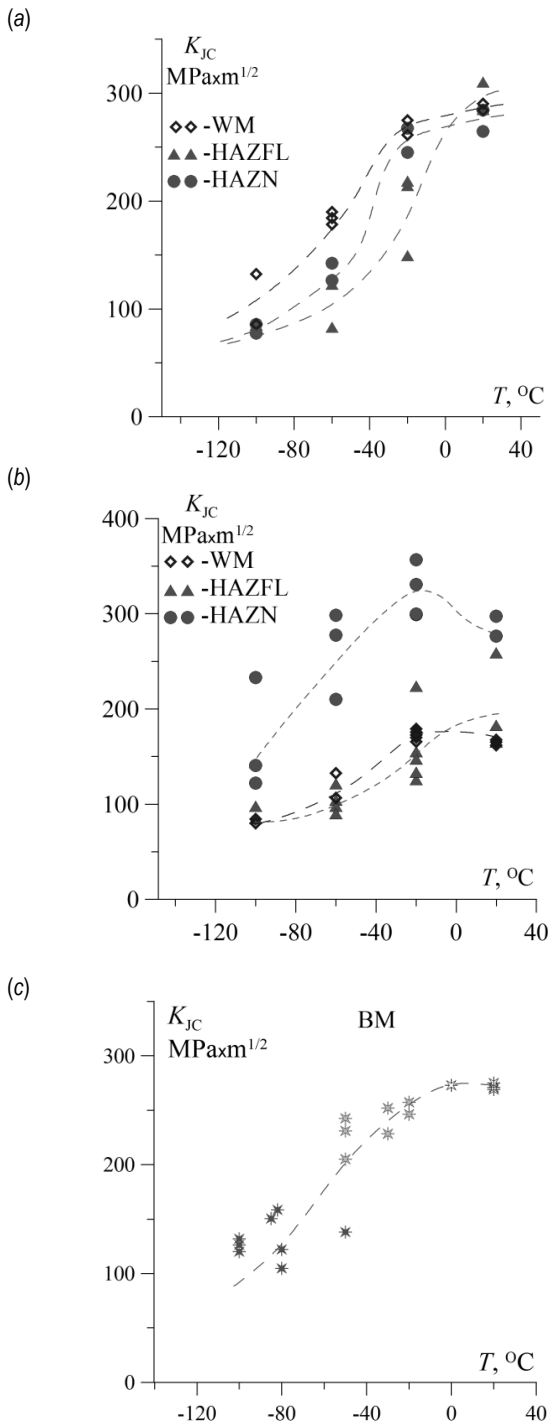
(a)

(b)

(c)

Fig. 6. K_{JC} dependency on the test temperature of different joints zones A (a), B (b), and BM (c)

Along with the lowering test temperature the fracture toughness WM also decreases, although always maintains the highest level of fracture toughness as compared to the material of the other joint zone A (Fig. 6a). The lowest level of fracture toughness is for the HAZFL material, especially at minus temperatures. At minus test temperatures were observed high scatter of the fracture toughness critical values in this material.

For the joint B, the lowest level K_{JC} is also present in the HAZFL material (Fig. 6b). Fracture toughness of WM in the B joint (with martensite microstructure (Fig. 1c)), is generally lower than in WM of A joint. The greatest difference was observed for tests at 20 °C. Along with lowering the temperature, the difference in K_{JC}

level for the WM of the joint A and B disappears. In the HAZN material of the joint B, registered a high K_{JC} level, which exceeds the K_{JC} values for HAZN of the joints A and BM (Fig. 6a, 6b, 6c). The fracture toughness increase, which occurs in the HAZN material of the joint B in comparison to the BM, can be carried out as a result of favorable parameters of tempering bainite-martensite microstructure BM (Bhadeshia, 2001; Dzioba, 2010).

4. SUMMARY

The mechanical properties and fracture toughness of the material from the different zones of welded joints made of high-strength ferritic steel was determined. Welding with higher LWE =1.2 kJ/mm leads to a formation of a fine-grained ferritic microstructure in WM of strength characteristics level ~0.5R_e and 0.5R_m, relative to BM. Fracture toughness of WM is a bit higher than BM. Welding of the lower LWE = 0.7 kJ/mm leads to the formation of the martensite microstructure in the WM of strength characteristics level ~0.85R_e and 0.85R_m, relative to BM. However, fracture toughness in this case is low: 0.5K_{JC} BM for temperature [-60 ÷ 20] °C and 0.8K_{JC} BM for T= -100 °C.

The weakest link in terms of fracture toughness in both joints is HAZFL material. Lower boundaries of the scattered data of K_{JC} for the HAZFL material in both joints are similar for $T \leq$ -20 °C. Nevertheless, the fracture toughness of the joint A and B is comparable, the level of the strength characteristics is higher in the joint B, which indicates that generally the joint B is better. Tensile tests carried out on specimens without notches with joints A and B showed, that the joint B strength is higher of ~ 15% [5].

REFERENCES

1. **ASTM E 1820-05**. (2000), *Standard Test Method for Measurement of Fracture Toughness*, ASTM; Philadelphia.
2. **Bhadeshia H.K.D.H.** (2001), Bainite in Steels, Institute of Materials, London.
3. **Dzioba I.** (2010), Properties of the 13HMF steel after operation and degradation under laboratory conditions, *Materials Science*, 46 (3), 357-364
4. **FITNET.** (2008), *Fitness – for – Service. Fracture – Fatigue – Creep – Corrosion*, Edited by M. Koçak, S. Webster, J.J. Janosch, R.A. Ainsworth, R. Koerc).
5. **Gałkiewicz J., Pała T., Dzioba I.** (2012), Strength properties of the welded joints made from high-strength ferritic steels, *XXIII Symposium: Fatigue and Fracture Mechanics*, Bydgoszcz – Pieczyska, 63-72 (in Polish).
6. **Neimitz A., Dzioba I., Graba M., Okrajni J.** (2008), *Assessment of the strength, durability and safety of the structural components containing defects*, Kielce University of Technology (in Polish).
7. **Porter D.** (2006), Developments in hot-rolled high strength structural steel, *Nordic welding conference 06, New trends in welding technology*, Tampere, Finland.
8. **Tasak E., Ziewiec A.** (2006), Welded joint structure of low-carbon and low-alloy steels, *Welded Review* 11/2006, 7-12 (in Polish).

CONTACT INTERACTION OF RIGID STAMP AND INFINITE ORTHOTROPIC PLATE WITH CLOSE TO ELLIPTICAL HOLE

Andriy KOTSYUBA[*]

[*]Lutsk National Technical University, Lvivska Str. 75, 43018 Lutsk, Ukraine

akaerkaj@rambler.ru

Abstract: Numerical method of finding the contact stresses under the stamp of complex shape for the case of orthotropic plates with close to an elliptical hole, which based on constructed in Bozhydarnik et al., (2007) algorithm, is developed. The distribution of contact stresses under the stamp, which shape matches the shape of the hole, is investigated.

Key words: Orthotropic, Elliptical Hole, Numerical Methot, Contact Stresses

1. INTRODUCTION

The problem of contact interaction of rigid smooth stamp of complex shape with elliptic boundary close to the hole (with the semi-axis R_x and R_y) in orthotropic infinite plate is examined. This problem sufficiently for such cases is studied: stamp has a circular shape and is close in size to the hole (Abd-El-Naby et al., 1993; Kombel, 2003; Panasyuk and Tepliy, 1975; Savin, 1968); stamp or system of stamps with corner points (Syackyj and Shynkarchuk, 2010; Syackyj and Trohymchuk, 2009, 2010a); infinite plate has elliptical (Bozhydarnik et al., 2007; Kombel, 2003; Sawin, 1968; Syackyj and Shynkarchuk, 2010, Syackyj and Trohymchuk, 2009) or more complex forms hole (Maksimovic et al., 2012; Syackyj and Shynkarchuk, 2011; Syackyj and Trohymchuk, 2010a, b); the contour of the curved hole infinite plate is partially strengthened (Syackyj and Trohymchuk, 2009, 2010b) etc.
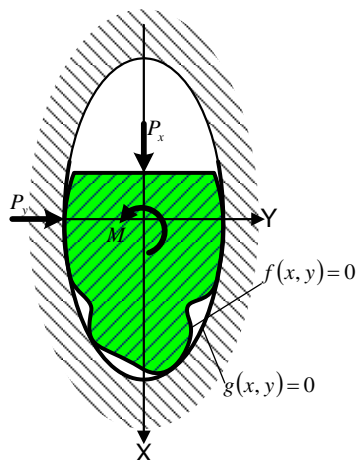

Fig. 1. Problem

Developed in this paper, a numerical method allows solving flat contact problems of elasticity theory in which the contact area is unknown in advance and may include individual sites.

We assume that the plate is weakened by close to an elliptical hole. Let the equation of the path that limits the hole, is given in implicit form $g(x, y) = 0$ (or parametric – $x = g_1(\alpha)$, $y = g_2(\alpha)$) and the border punch to the contact interaction – the equation:

$$f(x, y) = 0 \tag{1}$$

Suppose that known forces applied to the piston head and moment vectors are equal (P_x, P_y) and M.

While solving, we have that between the stamp and orthotropic body there are frictional forces. Assume that the stamp is in a state of limited equilibrium and there is the Coulomb's-Amontons law.

To solve the problem we use the numerical-analytic method (Bozhydarnik et al., 2007), which is based on the method of integral equations of mechanical quadratures and quadratic programming.

2. CONTACT CONDITIONS

Assuming that after the contact interaction shifting of the stamp in the direction of the coordinate axis Ox in the distance D_x and the angle of its rotation θ, we obtain from Bozhydarnik et al., (2007) terms of the contact form:

$$f_1(\alpha)\tilde{u}(\alpha) + f_2(\alpha)\tilde{v}(\alpha) = -\tilde{f}(\alpha) - D_x f_1(\alpha) \\ + \theta f_3(\alpha) + \delta(\alpha) \tag{2}$$

where: $\tilde{f}(\alpha) = f\big(g_1(\alpha), g_2(\alpha)\big)$;
$f_1(\alpha) = f_x'\big(g_1(\alpha), g_2(\alpha)\big)$;
$f_2(\alpha) = f_y'\big(g_1(\alpha), g_2(\alpha)\big)$;
$f_3(\alpha) = g_1(\alpha) \cdot f_2(\alpha) - g_2(\alpha) \times \times f_1(\alpha)$;
$\tilde{u}(\alpha) = u\big(g_1(\alpha), g_2(\alpha)\big)$;
$\tilde{v}(\alpha) = v\big(g_1(\alpha), g_2(\alpha)\big)$
plate boundaries due to the influence of an applied thereto a stamp; displacements – $\delta(\alpha) = o(\tilde{u}, \tilde{v})$ – additional members that have another order of smallness relative displacements.

Let the tangent τ at the stamp associated with the normal σ according to the Coulomb's-Amontons law $- \sigma = \rho\tau$ (ρ – coefficient of friction), whereas in the case of an elliptical hole axis R_x and R_y and the value for the displacement can be presented as:

$$\begin{cases} \tilde{u}(\alpha) = \int_\Omega \sigma(\xi)\big(K_1(\alpha,\xi) - \rho K_2(\alpha,\xi)\big)d\xi \\ \tilde{v}(\alpha) = \int_\Omega \sigma(\xi)\big(K_2(\alpha,\xi) - \rho K_1(\alpha,\xi)\big)d\xi \end{cases} \qquad (3)$$

where Ω – a set of segments along which there is contact;

$$\begin{cases} K_1(\alpha,\xi) = -\dfrac{1}{\pi}[-n_1\ln 2\sin\dfrac{|\alpha - \xi|}{2}R_y\cos\xi \\ \qquad\qquad -n_2\dfrac{\alpha - \xi + \pi}{2}R_x\sin\xi] \\ K_2(\alpha,\xi) = -\dfrac{1}{\pi}[-n_3\ln 2\sin\dfrac{|\alpha - \xi|}{2}R_x\sin\xi \\ \qquad\qquad +n_2\dfrac{\alpha - \xi + \pi}{2}R_y\cos\xi] \end{cases}$$

where: $n_1 = \frac{\beta_1+\beta_2}{E_1}$, $n_2 = \frac{-v_{12}}{E_1} + \frac{1}{\beta_1\beta_2 E_2} = \frac{-v_{12}}{E_1} + \frac{\beta_1\beta_2}{E_1} = \frac{-v_{21}}{E_2} + \frac{1}{\beta_1\beta_2 E_2} = \frac{-v_{21}}{E_2} + \frac{\beta_1\beta_2}{E_1}$, $n_3 = \frac{\beta_1+\beta_2}{E_2\beta_1\beta_2}$; here E_1, E_2 i v_{12}, v_{21} – the Young's modulus and the Poisson's ratio for the axes Ox and Oy; β_1 i β_2 – positive roots of the characteristic biquadratic equation:

$$\frac{\beta^4}{E_1} + \left(-\frac{2v_{12}}{E_1} + \frac{1}{G}\right)\beta^2 + \frac{1}{E_2} = 0$$

where G – the shear modulus.

Further, we suppose that the hole is close to the semi-axis R_x and R_y of the elliptical shape. Then its equation in parametric form is: $g_1(\alpha) = \tilde{R}_x(\alpha)\cos\alpha$, $g_2(\alpha) = \tilde{R}_y(\alpha)\sin\alpha$, $\alpha \in [-\pi,\pi)$, where $R_x - \tilde{R}_x(\alpha) = g_{x\varepsilon}(\alpha)$, $R_y - \tilde{R}_y(\alpha) = g_{y\varepsilon}(\alpha)$. Here $g_{x\varepsilon}$ and $g_{y\varepsilon}$ – limited by the absolute small number ε of features that characterize the deviation from the elliptical shape hole. We consider that the size ε is quite small, and in its relationships for displacements can be neglected without significant effect on the distribution of the desired contact stresses, i.e., moving on the surface of the hole set relations (3).

Additional equality for finding unknown D_x and θ looks like:

$$\begin{cases} \int_\Omega (\xi)\big(\tilde{R}_y(\xi)\cos\xi - \rho\tilde{R}_x(\xi)\sin\xi\big)d\xi = P_x \\ \int_\Omega (\xi)\big(\tilde{R}_x(\xi)\sin\xi - \rho\tilde{R}_y(\xi)\cos\xi\big)d\xi = P_y \end{cases} \qquad (4)$$

3. CONSTRUCTION OF INTEGRAL EQUATIONS

Let the stamp has a form close to elliptical with the semi-axis of the r_x and r_y. Then its equation is possible to present as the parametric form: $x = \tilde{r}_x(\alpha)\cos\alpha$, $y = \tilde{r}_y(\alpha)\sin\alpha$, $\alpha \in [-\pi,\pi)$, where $r_x - \tilde{r}_x(\alpha) = f_{x\delta}(\alpha)$, $r_y - \tilde{r}_y(\alpha) = f_{y\delta}(\alpha)$. Here $f_{x\delta}$ and $f_{y\delta}$ – limited by the absolute small number of features δ that characterize the deviation from the elliptical shape stamp.

To construct the integral equation (2) it was necessary to find the appropriate function f, i.e. an equation for hard punch in implicit form (1). If we draw considerations for arbitrary functions $\tilde{r}_x$ and $\tilde{r}_y$, then it is very much complicate further calculations. Therefore, to simplify, we assume that $f_{x\delta}(\alpha) = r_x\delta\cos(k\alpha)$ and

$f_{y\delta}(\alpha) = r_y\delta\cos(k\alpha)$. Then the equation stamp (1) has the form:

$$(x-\varepsilon)^2 + my^2 - r_x^2\big(1-\delta\cos(k\hat\alpha(x,y))\big)^2 = 0 , \qquad (5)$$

where $m = \dfrac{r_x^2}{r_y^2}$; $\hat\alpha(x,y) = \begin{cases} \arctan\left(\dfrac{r_x y}{r_y x}\right), & x > 0; \\[2mm] \arctan\left(\dfrac{r_x y}{r_y x}\right) + \pi, & x < 0, y \geq 0; \\[2mm] \arctan\left(\dfrac{r_x y}{r_y x}\right) - \pi, & x < 0, y < 0; \\[2mm] \dfrac{\pi}{2}\,\mathrm{sgn}\, y, & x = 0, y \neq 0. \end{cases}$

Ignoring the size δ, hold linearization of integrated equation (2) for a hard punch whose shape is given by equation (5). Then in condition (2) function $\tilde{f}$, $\tilde{f}_1$, $\tilde{f}_2$ i $\tilde{f}_3$, we obtain as a:

$$\begin{aligned} \tilde{f}(\alpha) &= \tilde{R}_x^2(\alpha) - r_x^2\big(1-\delta\cos(k\tilde\alpha(\alpha))\big)^2 + \varepsilon^2 - 2\tilde{R}_x(\alpha)\varepsilon\cos\alpha + \\ &\quad +\big(m\tilde{R}_y^2(\alpha) - \tilde{R}_x^2(\alpha)\big)\sin^2\alpha , \\ \tilde{f}_1(\alpha) &= 2\big(\tilde{R}_x(\alpha)\cos\alpha - \varepsilon\big) - \\ &\quad -r_x^2\delta k\big(1-\delta\cos(k\tilde\alpha(\alpha))\big)\sin(k\tilde\alpha(\alpha))\tilde\alpha_1(\alpha) , \quad \tilde{f}_2(\alpha) = 2m\times \\ &\times\tilde{R}_y(\alpha)\sin\alpha - r_x^2\delta k\big(1-\delta\cos(k\tilde\alpha(\alpha))\big)\sin(k\tilde\alpha(\alpha))\tilde\alpha_2(\alpha) , \\ \tilde{f}_3(\alpha) &= 2\tilde{R}_x(\alpha)\tilde{R}_y(\alpha)\sin\alpha\cos\alpha(m-1) + 2\tilde{R}_y(\alpha)\varepsilon\sin\alpha + \\ &\quad +r_x^2\delta k\big(1-\delta\cos(k\tilde\alpha(\alpha))\big)\big(\tilde{R}_y(\alpha)\tilde\alpha_1(\alpha)\sin\alpha - \tilde{R}_x(\alpha)\tilde\alpha_2(\alpha)\times \\ &\quad\times\cos\alpha\big)\sin(k\tilde\alpha(\alpha)); \qquad (6) \end{aligned}$$

where

$$\tilde\alpha(\alpha) = \hat\alpha\big(\tilde{R}_x(\alpha)\cos\alpha, \tilde{R}_y(\alpha)\sin\alpha\big),$$
$$\tilde\alpha_1(\alpha) = \hat\alpha_x'\big(\tilde{R}_x(\alpha)\cos\alpha, \tilde{R}_y(\alpha)\sin\alpha\big),$$
$$\tilde\alpha_2(\alpha) = \hat\alpha_y'\big(\tilde{R}_x(\alpha)\cos\alpha, \tilde{R}_y(\alpha)\sin\alpha\big).$$

After substituting relations for displacements (3) and functions (6) in the linearized form of condition (2), we obtain the integral equation in the form:

$$\int_\Omega \sigma(\xi)J(\alpha,\xi)d\xi + D_x f_1(\alpha) - \theta f_3(\alpha) = -\tilde{f}(\alpha) , \qquad (7)$$

where $J(\alpha,\xi)$ is the core of the integral equation and it looks quite bulky.

4. THE NUMERICAL ALGORITHM FOR SOLVING THE PROBLEM (Syackyj and Shynkarchuk, 2011; Maksimovic et al., 2012)

Determination of contact stresses of these equations is quite a challenge, because there may be a contact on a few areas, finding of the boundaries is reduced to finding the solutions of nonlinear equations. Solving this problem in the article carried out numerically. We introduce into consideration the area $D = [a,b]$, that contains all of the contact area, and additionally define in it out of the contact areas (at $\alpha \notin \Omega$) $\sigma(\alpha) = 0$. Then

conditions (7, 4) can be written as a system of equations-inequalities:

$$
\begin{cases}
\int_D \sigma(\alpha) J(\alpha,\xi) d\xi + D_x f_1(\alpha) - \theta f_3(\alpha) = F(\alpha), \sigma(\alpha) < 0, \\
\int_D \sigma(\alpha) J(\alpha,\xi) d\xi + D_x f_1(\alpha) - \theta f_3(\alpha) \le F(\alpha), \sigma(\alpha) = 0, \\
\int_D \sigma(\xi)\big(\tilde{R}_y(\xi)\cos\xi - \rho \tilde{R}_x(\xi)\sin\xi\big) d\xi = P_x, \\
\int_D \sigma(\xi)\big(\tilde{R}_x(\xi)\sin\xi + \rho \tilde{R}_y(\xi)\cos\xi\big) d\xi = P_y;
\end{cases}
\tag{8}
$$

where $F(\alpha) = -\tilde{f}(\alpha)$.

The function $J(\alpha,\xi)$ has logarithmic characteristics. To construct quadrature formulas we use the approach known in science. Smooth function $\sigma(\xi)$ we describe with linear, piecewise continuous functions:

$$
\sigma(\xi) = \sum_n \sigma_n S_h(\xi - \alpha_n),
\tag{9}
$$

where $S_h(\alpha) = \begin{cases} 1 - \dfrac{|\alpha|}{h}, & |\alpha| \le h, \\ 0, & |\alpha| > h; \end{cases}$ $\sigma_n = \sigma(\alpha_n)$; $\alpha_1, \alpha_2, ..., \alpha_N$ –

nodal points covering the region $[a, b]$; moreover $\alpha_{j+1} = \alpha_j + h$ a – partitioning step. Substituting (9) into the integral:

$$
I(\alpha) = \int_a^b \sigma(\xi) J(\alpha,\xi) d\xi,
\tag{10}
$$

we obtain quadrature formulas:

$$
I(\alpha_\nu) = \sum_{n=0}^N A_{\nu,n} \sigma_n, \quad \nu = \overline{0, N};
\tag{11}
$$

where:

$$
A_{\nu,n} = \int_{-h}^h S_h(t) J(\alpha_\nu, \alpha_n + t) dt.
\tag{12}
$$

Based on formulas (11) and (12) the system of equations and inequalities (8) can be written as:

$$
\begin{cases}
\sum_{n=0}^{N+2} A_{\nu,n} \sigma_n = F_\nu, \ \sigma_\nu < 0, \\
\sum_{n=0}^{N+2} A_{\nu,n} \sigma_n \le F_\nu, \ \sigma_\nu = 0, \\
\sum_{n=0}^N \lambda_n^1 \sigma_n = P_x, \sum_{n=0}^N \lambda_n^2 \sigma_n = P_y, \ \nu = \overline{0, N};
\end{cases}
\tag{13}
$$

where: $A_{V,N+1} = f_1(\alpha_V), A_{V,N+2} = -f_3(\alpha_V), F_V = -\tilde{f}(\alpha_V),$
$\lambda_n^1 = \int_{-h}^h S_h(t)\big(\tilde{R}_y(\alpha_n + t)\cos(\alpha_n + t) - \rho \tilde{R}_x(\alpha_n + t)\sin(\alpha_n + t)\big)dt,$ $\lambda_n^2 = \int_{-h}^h S_h(t)\big(\tilde{R}_x(\alpha_n + t)\sin(\alpha_n + t) - \rho \tilde{R}_y(\alpha_n + t)\cos(\alpha_n + t)\big)dt.$
It marked $\sigma_{N+1} = D_x, \sigma_{N+2} = \theta$.

Then the system (13) is reduced to quadratic programming problem (Maksimovic et al., 2012), namely the problem

of minimizing the magnitude $Y = \sum_{\nu=0}^{N+2}\left(\sum_{n=0}^{N+2}\big(A_{\nu,n}\sigma_n - F_\nu\big)\sigma_\nu\right)$

under conditions:

$$
\begin{cases}
\sum_{n=0}^{N+2} A_{\nu,n} \sigma_n \le F_\nu, \ \partial e \ \nu = \overline{0, N}, \\
\sum_{n=0}^N \lambda_n^1 \sigma_n = P_x, \sum_{n=0}^N \lambda_n^2 \sigma_n = P_y, \\
\sigma_n \le 0, \ \partial e \ n = \overline{0, N};
\end{cases}
$$

where it is assumed that $A_{N+1,n} = A_{N+2,n} \equiv 0, \ n = \overline{0, N+2}$. This problem is solved numerically using methods known in the studies.

Contact area using the above algorithm can be found directly. Solving the problem (13) and finding the appropriate distribution of contact stresses σ_n, we obtain that the points where $\sigma_n < 0$ determine the contact area, and have the points where $\sigma_n = 0$ determine the areas that are free from stress.

At sufficiently high accuracy of the proposed algorithm indicate solutions of problems given in Maksimovic et al. (2012). In particular, for a circular punch from the above given examples, it follows that with the choice of a sufficiently great number of nodal points can be obtained solution with pre-specified accuracy.

5. CONTACT STRAINS UNDER THE STAMP, THE SHAPE OF WHICH MATCHES THE SHAPE OF THE HOLE

Let first we have the case of isotropy, for which executed basic equations for generalized plane stress state and the equation of the hole is given by ratio (5). Then in parametric form, it will look like:
$x = \tilde{r}_x(1 - \delta\cos(k\alpha))\cos\alpha, \quad y = \tilde{r}_y(1 - \delta\cos(k\alpha))\sin\alpha,$
$\alpha \in [-\pi, \pi]$.

For simplicity, we assume that $E_1 = E_2 = E = 1.25$; $G = 0.5$; $v_{12} = v_{21} = v = 0.25$; $\rho = 0$; $Q_y = -\frac{P_y}{2GR} = 0$ $(R = \frac{R_x + R_y}{2})$ and $\delta = 0$ (i.e., the surface of the hole is not wavy).

The results of calculations of contact stresses with $\chi = 2.2$; $N = 601$ i $D = [-100^o, 100^o]$ are shown in Fig. 2 (as in work Maksimovic et al. (2012)). For different directions of the main force vector are obtained different distributions of contact stresses. For curves (1-4) force acts in the direction of major axis, and for curves (1'-4') – in minor axis direction. Here curves (1 and 1') correspond to the principal vector of force $Q_x^1 = -\frac{P_x^1}{2GR} = 0.005$, curves (2 and 2') – $Q_x^2 = 0.01$, curves (3 and 3') – $Q_x^3 = 0.015$, curves (4 and 4') – $Q_x^4 = 0.02$.

As seen from this figure, in the case of force acts in the direction of major axis maximum stress is reached in the center of the contact area. When the action efforts act in the minor axis direction (Fig. 2b) maximum in the distribution of contact stresses is achieved at the points $\alpha = \mp 55^o$, while it at the appropriate value of the force is more than 2 times smaller than in Fig. 2a. In addition, in two cases there is almost a linear relationship between the maximum values of the stresses and the main force vector. Contact area in all the cases coincides and is $\approx [-84^o, 84^o]$.
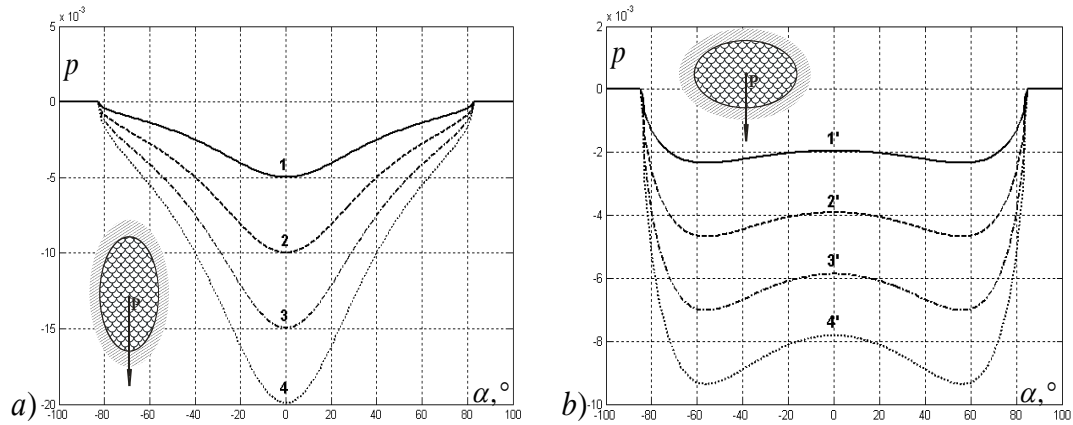
Fig. 2. Contact stresses under stamp of elliptical form: a) force acts in the direction of major axis; b) force acts in the direction of minor axis

Further, we assume that there is a orthotropy for which basic equations for generalized plane stress condition are performed. Unlike previous abstract example, consider specific application cases of orthotropic materials. For example, first we have aluminum borosilicate fiberglass (E-glass), which is characteristic for isotropic properties in the plane, which is perpendicular to the direction of the fibers. For this material we have:

$$E_x = 6.25 \text{ GPa}; E_y = 21.2 \text{ GPa},$$

$$G_{xy} = 9 \text{ GPa}, v_{xy} = 0.251 \tag{14}$$

From the characteristics (14) we pass to dimensionless characteristics:

$$E_1 = \frac{E_x}{2G_{xy}} = 3\frac{17}{36}, \ E_2 = 1\frac{8}{45}, \ G = 0.5, \ v_{12} = 0.251,$$

$$v_{21} = 0.251 \cdot \frac{E_2}{E_1} = 0.251 \cdot \frac{212}{625} = 0.0851392. \tag{15}$$

The results of calculations of contact stresses, if $\delta = 0.0004$, $k = 20$ (there is waviness of surfaces of the hole and stamp), $N = 461$, $D = [-90^o, 94^o]$, at different values of the coefficient of friction ρ and the main vectors of forces Q_x та Q_y are shown in Fig. 3 and 4. Curves (1-4) in both figures correspond to the coefficient of friction $\rho = 0$, curves (1'-4') – $\rho = 0.2$, and curves (1"-4") – $\rho = 0.4$.
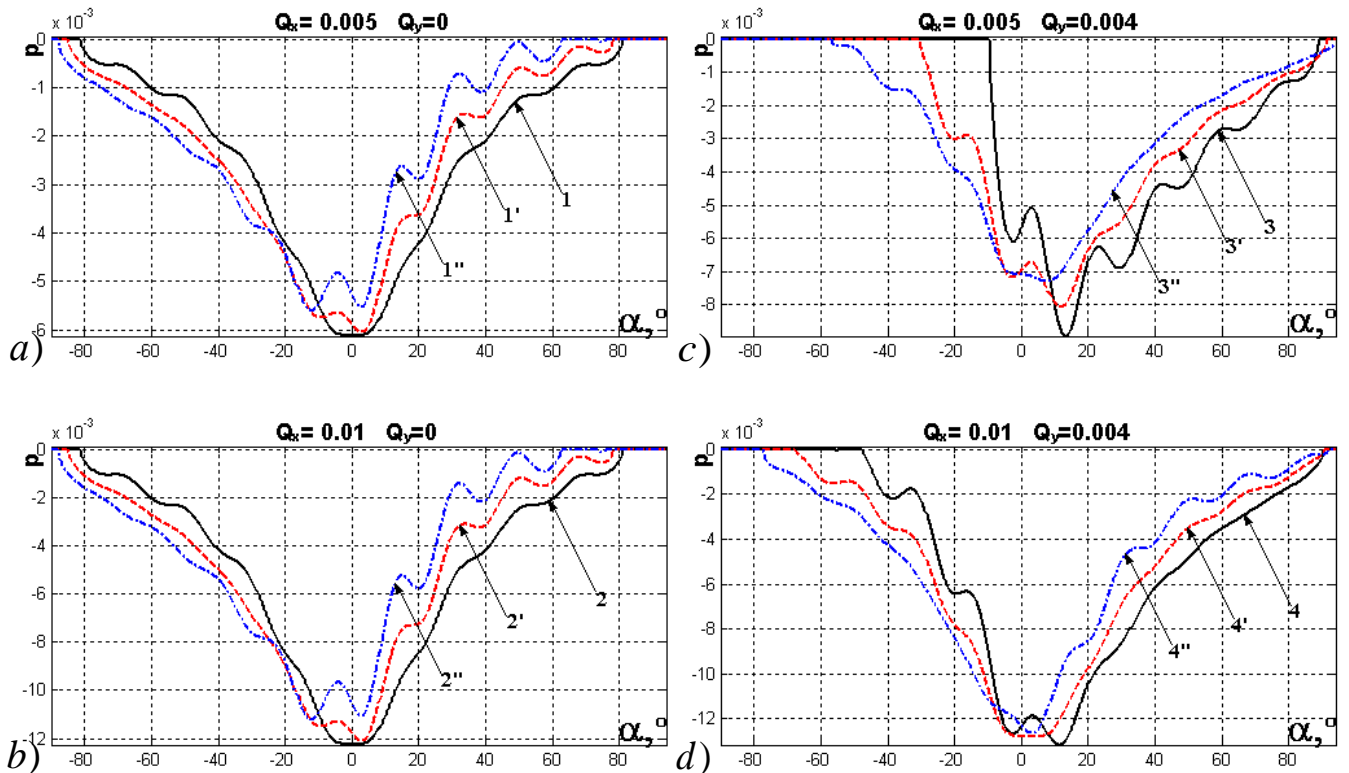

Fig. 3. Contact stresses under the stamp, which shape is similar to the elliptical on the surface of a similar hole in the orthotropic plate (E-glass), when bigger force acts in the direction of major axis
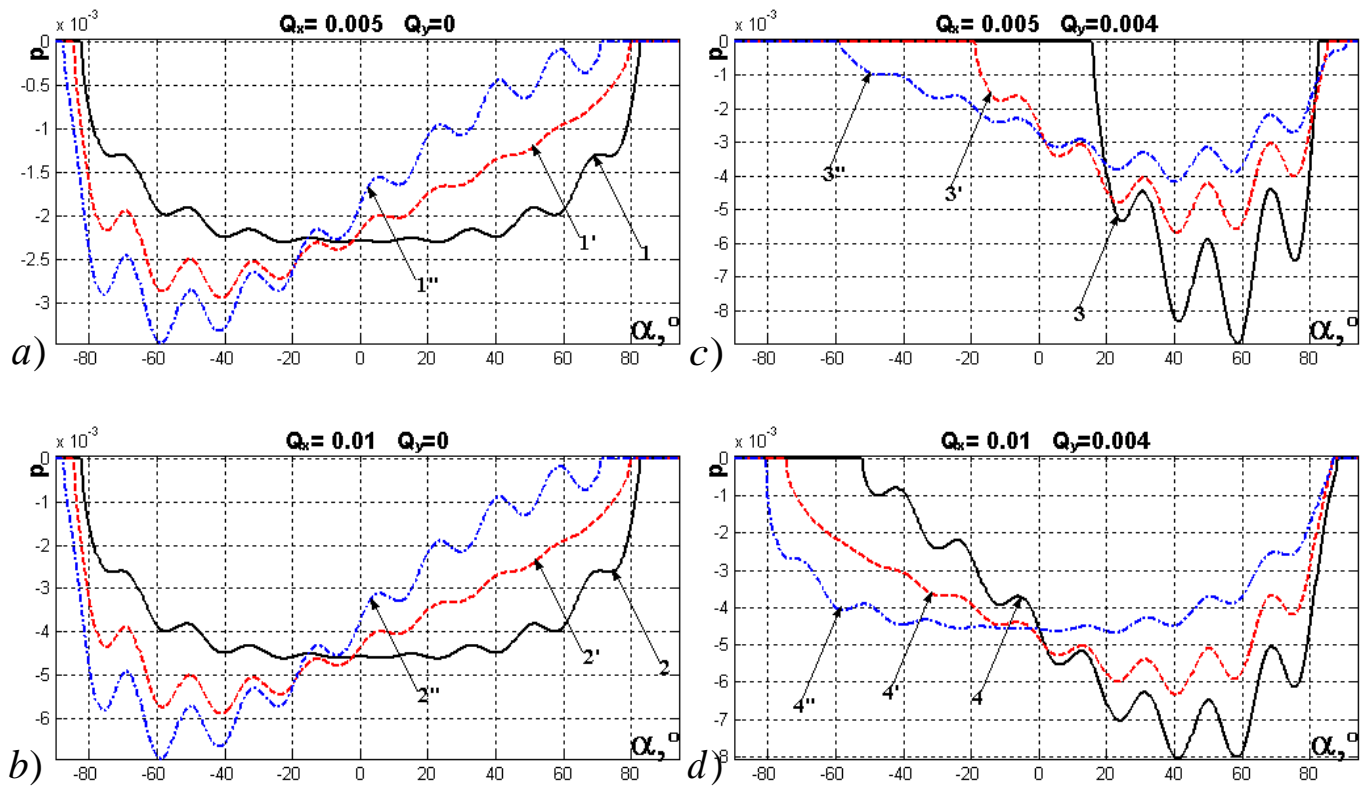
Fig. 4. Contact stresses under the stamp, which shape is similar to the elliptical on the surface of a similar hole in the orthotropic plate (E-glass), when bigger force acts in the direction of minor axis

As shown in Fig. 3 and 4 increase of the coefficient of friction leads to increase of the asymmetry in the negative (clockwise) direction, and an increase relatively to the main vector of force Q_y, however, increases the asymmetry in the positive direction. Let investigate dependence of the characteristics of elasticity and relative distribution of contact stresses. To do this, choose the case where $Q_x = 0.01$, $Q_y = 0.004$ i $\rho = 0.2$.

The results of calculations of contact stresses with $G = 0.5$ are shown in Fig. 5 and 6 for orthotropic materials such as E-glass (properties (14')) – curve (1), fiber reinforced with boron ($E_1 = 12\frac{7}{17}$, $E_2 = 1\frac{41}{170}$, $v_{12} = 0.35$, $v_{21} = 0.035$ – curve (2), fiber-reinforced with graphite ($E_1 = 18.625$, $E_2 = 0.75$, $v_{12} = 0.31$, $v_{21} = \frac{93}{7450}$) – curve (3).
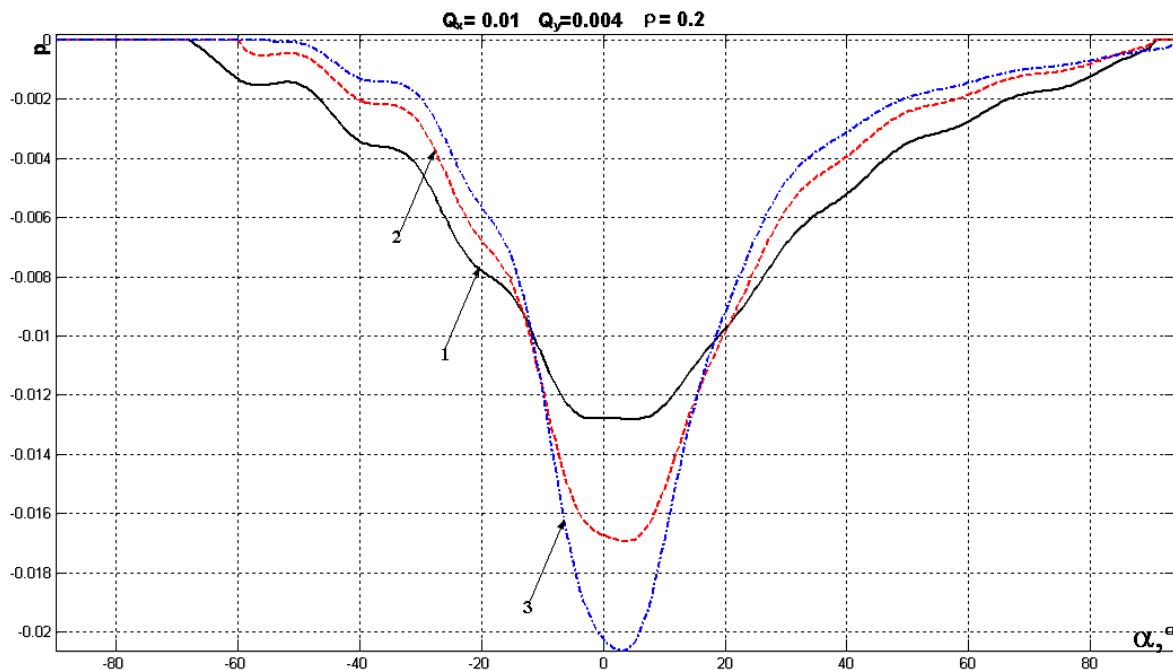

Fig. 5. Contact stresses under the stamp, which shape is similar to the elliptical, on the surface of a similar hole in different orthotropic plates when a larger force acts in the direction of major axis
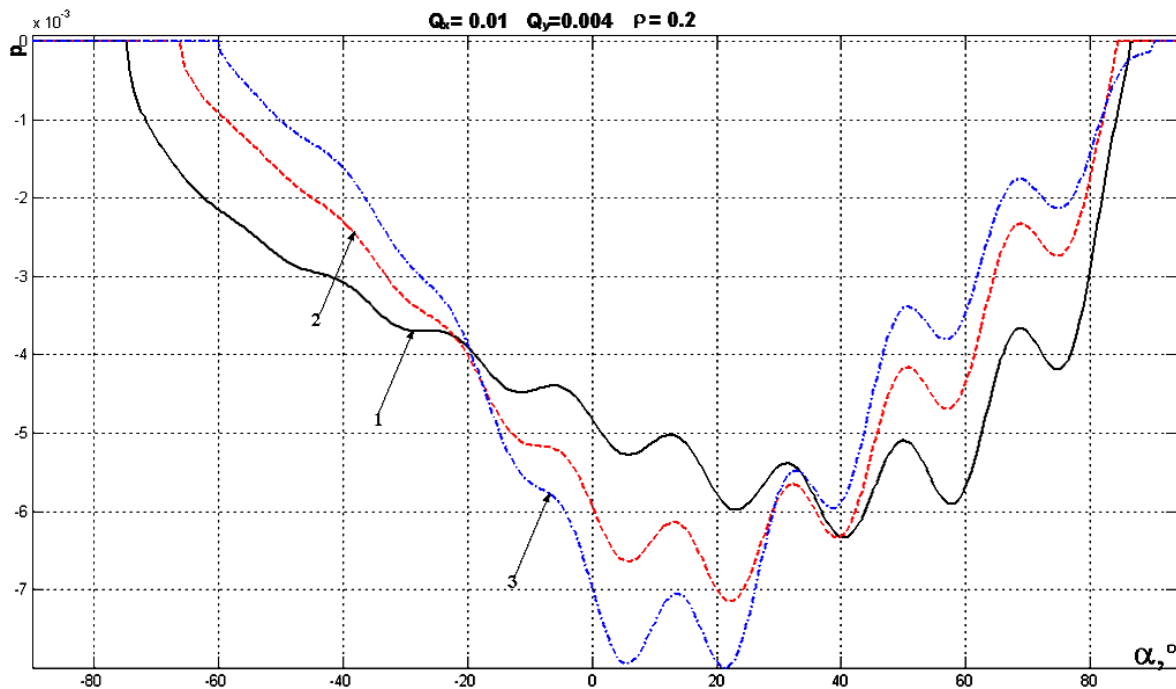
Fig. 6. Contact stresses under the stamp, which shape is similar to the elliptical, on the surface of a similar hole in different orthotropic plates when a larger force acts in the direction of minor axis

As shown in Fig. 5 and 6 in the distribution of contact stresses relative size of the contact area depends on the Poisson ratio (the smaller v_{12} is the greater the contact area) which indicates the physical meaning of the Poisson ratio. While it is clear that the contact area and maximum stress significantly influence the modulus of elasticity. For a more overall understanding of the influence it'd be better to consider more examples and without waviness. In this study, we aimed to describe the versatility of the developed numerical and analytical methods for which is of no value bulkiness of recording of the resulting integral equation and the complexity of analytically solving of the problem (7, 4).

6. CONCLUSIONS

Numerical and analytical methods for calculating the relative distributions of contact stresses on the surfaces of complex shape holes in infinite plates (Maksimovic et al., 2012), which is based on the methods of boundary integral equations, mechanical quadratures and quadratic programming, which is developed for the case of orthotropy are worked out. Integral equations were constructed similarly as in Bozhydarnik et al. (2007); Kombel (2003); Panasyuk and Tepliy (1975), Savin (1968), Syackyj and Shynkarchuk (2010, 2011); Syackyj and Trokhymchuk (2009, 2010a, b). The very same methods are tested on simpler problems (Maksimovic et al., 2012), for which the analytical solutions are known in the science.

REFERENCES

1. **Abd-El-Naby S.F.M., Hollaway L., Gunn M.** (1993), The tangential stresses in an infinite orthotropic composite plate with a loaded hole Original Research Article, *Composites Engineering*, Vol. 3, Issue 1, 19-30.
2. **Bozhydarnik V.M.**, **Kotsyuba A.Yu., Maksimovic O.V.** (2007), Contact interaction of arbitrary shape stamp and plate with elliptical hole, *Bulletin of Dnipropetrovsk University Series: Mechanics*, Edition 11, Vol. 2, No 2/2, 29–34, (in Ukrainian).
3. **Kombel S.M.** (2003), Landing of hard drive into elliptical hole of infinite orthotropic plate, *Engineering*, No 8, 29–34, (in Ukrainian).
4. **Maksimovic V.M., Kotsyuba A.Yu., Lavrenchuk S.V.** (2012), *Plane contact problems of elasticity theory for bodies of complex shape*, LNTU, Lutsk, (in Ukrainian).
5. **Panasyuk V.V., Tepliy M.Y.** (1975), *Some contact problems of the theory of elasticity*, Naukova Dumka, Kyiv, (in Ukrainian).
6. **Savin G.H.** (1968), *The stress distribution around the holes*, Naukova Dumka, Kyiv, (in Russian).
7. **Syackyj A.O, Shynkarchuk N.V.** (2010), Mixed contact problem for orthotropic plate with elliptical hole and rigid disk, *Herald of Ternopil National Technical University*, Vol. 15, No 4, 7–13, (in Ukrainian).
8. **Syackyj A.O, Shynkarchuk N.V.** (2011), Mixed contact problem for isotropic plate with curvilinear hole and rigid disk, *Herald of Ternopil National Technical University*, Vol. 16, No 1, 16–21, (in Ukrainian).
9. **Syackyj A.O, Trokhymchuk O.Ya.** (2009), Pressure rigid stamp with corner points on a partially strengthened contour elliptic hole in infinite orthotropic plate, *Herald of Ternopil State Technical University*, Vol. 14, No 3, 12–18, (in Ukrainian).
10. **Syackyj A.O, Trokhymchuk O.Ya.** (2010a), Mixed contact problem for a plate with a curvilinear hole and the system of stamps with corner points, *Herald of National Technical University of Ukraine "Kyiv Polytechnic Institute". Series of "Mechanical Engineering"*, No 58, 36–41, (in Ukrainian).
11. **Syackyj A.O, Trokhymchuk O.Ya.** (2010b), Pressure system of two stamps with corner points on a partially strengthened contour elliptic hole orthotropic plate, *Herald of Ternopil State Technical University*, Vol. 15, No 1, 14–20, (in Ukrainian).

FRICTIONAL HEATING DURING SLIDING OF TWO SEMI-SPACES WITH SIMPLE THERMAL NONLINEARITIES

Ewa OCH*

*Faculty of Mechanical Engineering, Bialystok University of Technology, ul. Wiejska 45C, Bialystok, 15-351, Poland

e.och@doktoranci.pb.edu.pl

Abstract: In the article the nonstationary thermal problem of friction for two semi-spaces with taking into account their imperfect thermal contact and thermosensitivity of materials (simple nonlinearity), has been considered. The linearization of this problem has been carried out using Kirchhoff transformation, and next using the Laplace integral transform. The analytical solution to the problem in the case of constant speed sliding, has been obtained. On the basis of the obtained solutions and using Duhamel's formula, the analytical solution to the problem for sliding with constant deceleration, has been obtained, too. The results of numerical analysis are presented for two friction pairs.

Key words: Frictional Heating, Simple Thermal Nonlinearities, Thermosensitive Materials

1. INTRODUCTION

The review of analytical and numerical methods to solve the one-dimensional heat problems of friction, has been presented in the article by Yevtushenko and Kuciej (2012). It has been established, that there are practically no solutions to contact problem involving frictional heating, which would take into account the dependence of the thermal materials properties on temperature. In articles by Abdel-Aal (1997) and Abdel-Aal and Smith (1998) the solutions to heat problems of friction in case of separate heating of the two bodies have been obtained.

The aim of this work is to obtain a solution of the contact heat problem with friction for two thermosensitive semi-spaces, which relatively slide with constant speed. It is assumed that materials properties of the bodies have a simple nonlinearity, i.e. the coefficients of thermal conductivity and specific heat are dependent on temperature and their ratio – the thermal diffusivity – is constant (Kushnir and Popovych, 2011). For many friction materials dependence of thermal properties on temperature is linear (Gundlach, 1983; Abdel-Aal, 1997; Abdel-Aal and Smith, 1998; Sok, 2006):

$$K_l(T_l) = K_{l,0}\, K_l^*(T_l)\,,\, c_l(T_l) = c_{l,0}\, c_l^*(T_l) \qquad (1)$$

where:

$$K_l^*(T_l) = 1 + \lambda_l(T_l - T_0)\,,\, c_l^*(T_l) \approx K_l^*(T_l)\,,\; l = 1,2 \qquad (2)$$

Here and further, all values referring to the semi-spaces will have subscripts 1 and 2, respectively.

2. STATEMENT OF THE PROBLEM

The problem of contact interaction of two bodies (semi-spaces) with different thermal-physical properties is considered. It is supposed, that the constant compressive pressure p_0 in direction of z-axis of the Cartesian system of coordinates Oxyz are applied to the infinities in semi-spaces (Fig. 1). In the initial time moment $t = 0$ the semi-spaces start to slide with a constant speed V_0 in the positive direction of the y-axis. Due to friction the heat is generated on a contact plane $z = 0$. The sum of intensities of frictional heat fluxes directed into each semi-spaces is equal to the specific power of friction $q_0 = fV_0 p_0$ (Ling, 1973). Because of the thermal resistance between surfaces of the bodies, the heat transfer with a constant coefficient of thermal conductivity of contact h takes place.
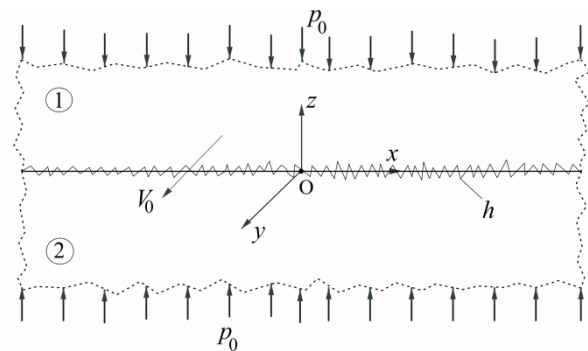

Fig. 1. Scheme of the problem

Let us find the distribution of the transient temperature fields $T_l(z,t)$, $l = 1,2$ in each of the semi-spaces from the solution to the following heat problem of friction:

$$K_1(T_1)\frac{\partial^2 T_1(z,t)}{\partial z^2} = \rho_1 c_1(T_1)\frac{\partial T_1(z,t)}{\partial t}\,,\; z > 0,\; t > 0\,, \qquad (3)$$

$$K_2(T_2)\frac{\partial^2 T_2(z,t)}{\partial z^2} = \rho_2\, c_2(T_2)\frac{\partial T_2(z,t)}{\partial t}\,,\; z < 0,\; t > 0\,, \qquad (4)$$

$$K_1(T_1)\frac{T_1(z,t)}{\partial z}\bigg|_{z=0} - K_2(T_2)\frac{\partial T_2(z,t)}{\partial z}\bigg|_{z=0} = -q,\ t>0, \qquad (5)$$

$$K_1(T)\frac{\partial T_1(z,t)}{\partial z}\bigg|_{z=0} + K_2(T)\frac{\partial T_2(z,t)}{\partial z}\bigg|_{z=0} = \qquad (6)$$
$$= h[T_1(0,t) - T_2(0,t)],\ t>0,$$

$$T_l(z,t) \to T_0,\ |z|\to\infty,\ l=1,2, \qquad (7)$$

$$T_l(z,0) = T_0,\ |z|<\infty,\ l=1,2. \qquad (8)$$

By introducing dimensionless variables and parameters:

$$\zeta = \frac{z}{a},\ \tau=\frac{k_2 t}{a^2},\ K_0^* = \frac{K_{1,0}}{K_{2,0}},\ k^* = \frac{k_1}{k_2}, \qquad (9)$$

$$Bi = \frac{h\,a}{K_{2,0}},\ T_a = \frac{q_0\,a}{K_{2,0}},\ T_{1,2}^* = \frac{T_{1,2}}{T_a},\ T_0^* = \frac{T_0}{T_a}, \qquad (10)$$

the above mentioned non-linear transient boundary-value heat conduction problem of friction (3)–(8) can be represented in the dimensionless form:

$$K_1(T_1^*)\frac{\partial^2 T_1^*(\zeta,\tau)}{\partial\zeta^2} = \frac{c_1^*(T_1^*)}{k^*}\frac{\partial T_1^*(\zeta,\tau)}{\partial\tau},\ \zeta>0,\tau>0 \qquad (11)$$

$$K_2(T_2^*)\frac{\partial^2 T_2^*(\zeta,\tau)}{\partial\zeta^2} = c_2^*(T_2^*)\frac{\partial T_2^*(\zeta,\tau)}{\partial\tau},\ \zeta>0,\ \tau>0 \qquad (12)$$

$$K_0^* K_1^*(T_1^*)\frac{\partial T_1^*(\zeta,\tau)}{\partial\zeta}\bigg|_{\zeta=0} - K_2^*(T_2^*)\frac{\partial T_2^*(\zeta,\tau)}{\partial\zeta}\bigg|_{\zeta=0} = -1, \qquad (13)$$
$$\tau>0,$$

$$K_0^* K_1^*(T_1^*)\frac{\partial T_1^*(\zeta,\tau)}{\partial\zeta}\bigg|_{\zeta=0} + K_2^*(T_2^*)\frac{\partial T_2^*(\zeta,\tau)}{\partial\zeta}\bigg|_{\zeta=0} = \qquad (14)$$
$$= Bi[T_1^*(0,\tau) - T_2^*(0,\tau)],\ \tau>0,$$

$$T_l^*(\zeta,\tau) \to T_0^*,\ |\zeta|\to\infty,\ l=1,2 \qquad (15)$$

$$T_l(\zeta,0) = T_0^*,\ |\zeta|<\infty\ l=1,2 \qquad (16)$$

where, taking into account the relations (9), (10), the linear dependencies of thermal conductivity on temperature (2) express as follows:

$$K_l^*(T_l^*) = 1 + \Lambda_l(T_l^* - T_0^*),\ \Lambda_l = \lambda_l T_a,\ l=1,2 \qquad (17)$$

3. LINEARIZATION OF THE PROBLEM

To the linearization of the boundary-value problem (11)–(16), the Kirchhoff transform has been used (Kirchhoff, 1894):

$$\Theta_l = \int_{T_0^*}^{T_l^*} K_l^*(T_l^*)\ dT_l^*,\ l=1,2. \qquad (18)$$

By applying the transformation (18) to the problem (11)–(16) and taking into account the relations $c_l^*(T_l^*) \approx K_l^*(T_l^*)$, we have:

$$\frac{\partial^2 \Theta_1(\zeta,\tau)}{\partial\zeta^2} = \frac{1}{k^*}\frac{\partial\Theta_1(\zeta,\tau)}{\partial\tau},\ \zeta>0,\ \tau>0, \qquad (19)$$

$$\frac{\partial^2 \Theta_2(\zeta,\tau)}{\partial\zeta^2} = \frac{\partial\Theta_2(\zeta,\tau)}{\partial\tau},\ \zeta<0,\ \tau>0, \qquad (20)$$

$$K_0^*\frac{\partial\Theta_1(\zeta,\tau)}{\partial\zeta}\bigg|_{\zeta=0} - \frac{\partial\Theta_2(\zeta,\tau)}{\partial\zeta}\bigg|_{\zeta=0} = -1,\ \tau>0, \qquad (21)$$

$$K_0^*\frac{\partial\Theta_1(\zeta,\tau)}{\partial\zeta}\bigg|_{\zeta=0} + \frac{\partial\Theta_2(\zeta,\tau)}{\partial\zeta}\bigg|_{\zeta=0} = \qquad (22)$$
$$= Bi[T_1^*(0,\tau) - T_2^*(0,\tau)],\ \tau>0,$$

$$\Theta_l(\zeta,\tau) \to 0,\ |\zeta|\to\infty, \tau>0,\ l=1,2, \qquad (23)$$

$$\Theta_l(\zeta,0) = 0,\ |\zeta|<\infty,\ l=1,2. \qquad (24)$$

In the assumption of linear dependence (17), from formula (18) we find the connection between the dimensionless temperature $T_l^*(\xi,\tau)$ and the Kirchhoff function $\Theta_l(\xi,\tau)$, $l=1,2$ in the form:

$$T_l^*(\zeta,\tau) = T_0^* + \Lambda_l^{-1}[\sqrt{1+2\Lambda_l\Theta_l(\zeta,\tau)} -1],\ l=1,2, \qquad (25)$$

Using the approximate expansion (Nowinski, 1962):

$$\sqrt{1+2\Lambda_l\Theta_l(0,\tau)} \approx 1+\Lambda_l\Theta_l(0,\tau),\ l=1,2. \qquad (26)$$

from equation (25) we obtain the linear dependence between dimensionless temperature and the Kirchhoff function on the surface of friction:

$$T_l^*(0,\tau) = T_0^* + \Theta_l(0,\tau),\ l=1,2. \qquad (27)$$

In accordance with relations (27) the boundary condition (22) takes the form:

$$K_0^*\frac{\partial\Theta_1(\zeta,\tau)}{\partial\zeta}\bigg|_{\zeta=0} + \frac{\partial\Theta_2(\zeta,\tau)}{\partial\zeta}\bigg|_{\zeta=0} = \qquad (28)$$
$$= Bi[\Theta_1(0,\tau) - \Theta_2(0,\tau)],\ \tau>0.$$

Note that the linear relationship (27) between the dimensionless temperature and the Kirchhoff function takes place only on the surface of the contact. Within each semi-spaces the dependences between these variables are nonlinear and are given by equation (25).

4. THE KIRCHHOFF FUNCTIONS AT UNIFORM SLIDING

By applying the Laplace integral transform (Sneddon, 1972):

$$\overline{\Theta}_l(\zeta, p) \equiv L[\Theta_l(\zeta,\tau); p] = \int_0^\infty \Theta_l(\zeta,\tau)e^{-p\tau}d\tau. \qquad (29)$$

to the linear boundary-value problem (19)–(21), (23), (24) and (28), we obtain the following boundary problem for two ordinary differential equations of the second order:

$$\frac{d^2\overline{\Theta}_1(\zeta,p)}{d\zeta^2} - \frac{p}{k^*}\overline{\Theta}_1(\zeta,p) = 0,\ \zeta>0, \qquad (30)$$

$$\frac{d^2 \overline{\Theta}_2(\zeta, p)}{d\zeta^2} - p\overline{\Theta}_2(\zeta, p) = 0, \ \zeta < 0, \tag{31}$$

$$K_0^* \frac{d\overline{\Theta}_1(\zeta, p)}{d\zeta}\bigg|_{\zeta=0} - \frac{d\overline{\Theta}_2(\zeta, p)}{d\zeta}\bigg|_{\zeta=0} = -\frac{1}{p}, \tag{32}$$

$$K_0^* \frac{d\overline{\Theta}_1(\zeta, p)}{d\zeta}\bigg|_{\zeta=0} + \frac{d\overline{\Theta}_2(\zeta, p)}{d\zeta}\bigg|_{\zeta=0} =$$
$$= Bi[\overline{\Theta}_1(0, p) - \overline{\Theta}_2(0, p)], \tag{33}$$

$$\overline{\Theta}_l(\zeta, p) \to 0, \ |\zeta| \to \infty, \ l=1,2. \tag{34}$$

The solution to the problem (30)–(34) has the form:

$$\overline{\Theta}_1(\zeta, p) = \frac{e^{-\zeta_1 \sqrt{p}}}{2\varepsilon(\sqrt{p}+\beta)}\left(\frac{1}{p} + \frac{Bi}{p\sqrt{p}}\right), \ \zeta \geq 0, \tag{35}$$

$$\overline{\Theta}_2(\zeta, p) = \frac{e^{-\zeta_2 \sqrt{p}}}{2\varepsilon(\sqrt{p}+\beta)}\left(\frac{\varepsilon}{p} + \frac{Bi}{p\sqrt{p}}\right), \ \zeta \leq 0, \tag{36}$$

where:

$$\beta = \frac{Bi(1+\varepsilon)}{2\varepsilon}, \ \varepsilon = \frac{K_0^*}{\sqrt{k^*}}, \ \zeta_1 = \frac{\zeta}{\sqrt{k^*}}, \ \zeta_2 = -\zeta. \tag{37}$$

Applying the inversion formulae (Bateman and Erdelyi, 1954):

$$L^{-1}\left[\frac{e^{-\zeta_l \sqrt{p}}}{p(\sqrt{p}+\beta)}; \tau\right] = \beta^{-1}\Psi(\zeta_l, \tau), \tag{38}$$

$$L^{-1}\left[\frac{e^{-\zeta_l \sqrt{p}}}{p\sqrt{p}(\sqrt{p}+\beta)}; \tau\right] = \beta^{-1}\Phi(\zeta_l, \tau) - \beta^{-2}\Psi(\zeta_l, \tau), \tag{39}$$

where:

$$\Phi(\zeta_l, \tau) = 2\sqrt{\tau}\ \text{ierfc}\left(\frac{\zeta_l}{2\sqrt{\tau}}\right), \tag{40}$$

$$\Psi(\zeta_l, \tau) = \text{erfc}\left(\frac{\zeta_l}{2\sqrt{\tau}}\right) - e^{\beta^2\tau + \zeta_l\beta}\text{erfc}\left(\frac{\zeta_l}{2\sqrt{\tau}} + \beta\sqrt{\tau}\right), \tag{41}$$

to the Laplace'a transform solutions (35) and (36), we obtain the Kirchhoff functions for each semi-spaces at any time moment $\tau \geq 0$:

$$\Theta_l(\zeta, \tau) = (1+\varepsilon)^{-1}[\Phi(\zeta_l, \tau) + \gamma_l\Psi(\zeta_l, \tau)], \ l=1,2. \tag{42}$$

where:

$$\gamma_1 = \frac{1-\varepsilon}{Bi(1+\varepsilon)}, \ \gamma_2 = \frac{\varepsilon(\varepsilon-1)}{Bi(1+\varepsilon)}. \tag{43}$$

At $\xi = 0$ from solutions (40)–(42) we have:

$$\Theta_l(0, \tau) = (1+\varepsilon)^{-1}[\varphi(\tau) + \gamma_l\psi(\tau)], \ \tau \geq 0, \ l=1,2. \tag{44}$$

where:

$$\varphi(\tau) = 2(\tau/\pi)^{1/2}, \ \psi(\tau) = 1 - e^{\beta^2\tau}\text{erfc}\ (\beta\sqrt{\tau}). \tag{45}$$

The dimensionless temperature of the semi-spaces we calculate using the formulae (25) and (42)–(45).

5. THE KIRCHHOFF FUNCTIONS AT SLIDING WITH UNIFORM DECELERATION

At braking with a constant deceleration the specific power of friction is equal (Kuciej, 2012):

$$q(\tau) = q_0 q^*(\tau), \ q^*(\tau) = 1 - \tau\tau_s^{-1}, \ 0 \leq \tau \leq \tau_s, \tag{46}$$

where $\tau_s = k_2 t_s a^{-2}$. In this case, the Kirchhoff functions can be found from the Duhamel formula (Ozisik, 1980) at $0 \leq \tau \leq \tau_s$:

$$\Theta_l^*(\zeta, \tau) = \int_0^\tau q^*(s)\frac{\partial}{\partial\tau}\Theta_l^{(0)*}(\zeta, \tau - s)ds, \tag{47}$$

where the functions $\theta_l^{(0)*}(\xi, \tau)$, $l = 1,2$ have the form (42) and (43). Substituting under the integral sign in formula (47) the functions (42), after integration we find at $0 \leq \tau \leq \tau_s$:

$$\Theta_l^*(\zeta, \tau) = \Theta_l^{(0)*}(\zeta, \tau) - \tau_s^{-1}\Theta_l^{*(1)}(\zeta, \tau), \ l=1,2 \tag{48}$$

where:

$$\Theta_l^{*(1)}(\zeta, \tau) = (1+\varepsilon)^{-1}\{[\tau + 6^{-1}\zeta_l^2 - \gamma_l(0.5\zeta_l + \beta^{-1})] \times$$
$$\times \Phi(\zeta_l, \tau) - 3^{-1}\tau\varphi(\tau)\exp(-0.25\zeta_l^2\tau^{-1}) + \tag{49}$$
$$+ \gamma_l[\beta^{-2}\Psi_l(\zeta_l, \tau) + \tau\ \text{erfc}\ (0.5\zeta_l\tau^{-1/2})]\}.$$

At $\xi = 0$ from the solution (49) it follows:

$$\Theta_l^{*(1)}(0, \tau) = (1+\varepsilon)^{-1}\{[(2/3)\tau - \gamma_l\beta^{-1}]\varphi(\tau) +$$
$$+ \gamma_l[\beta^{-2}\psi_l(\tau) + \tau]\}, 0 \leq \tau \leq \tau_s. \tag{50}$$

In limiting case $Bi \to \infty$ from the formulae (44) and (48), (50) we obtain the Kirchhoff functions at the perfect thermal contact between the semi-spaces in the form (Fazekas, 1953):

$$\Theta_l^*(\zeta, \tau) = \frac{1}{(1+\varepsilon)}\left[1 - \frac{2\tau}{3\tau_s}\right]\varphi(\tau), \ 0 \leq \tau \leq \tau_s. \tag{51}$$

6. NUMERICAL ANALYSIS AND CONCLUSIONS

The numerical analysis for two friction pairs gray iron - A356 and A315 - A356 for $q = 1$ MW/m^2, $a = 0.015\ m$ and $T_0 = 20°C$, has been performed. The values of coefficients of thermal conductivity K_0, thermal diffusivity k of materials and values of the coefficients λ, which characterize changing of the coefficients of thermal conductivity and specific heat with tempera-ture, are shown in Tab. 1.
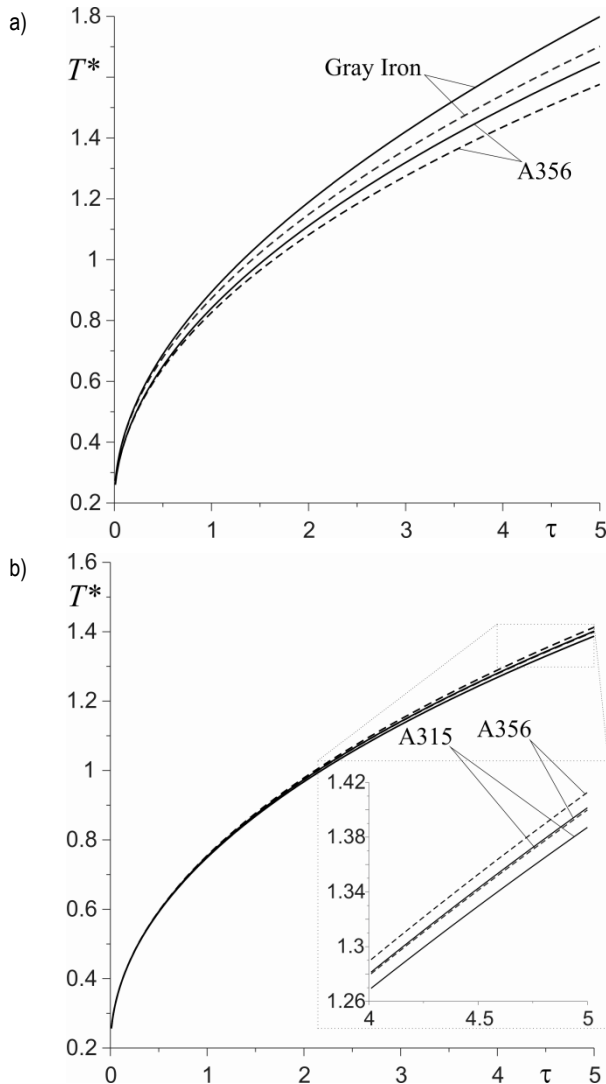
The evolutions of the dimensionless temperature on the contact surfaces during constant sliding for two friction pair, with and without taking into account the thermosensitive materials, are shown in Figs. 2: gray iron - A356 (Fig. 2a) and A315 - A356 (Fig. 2b).

Tab. 1. Thermo-physical materials properties used in numerical analysis

Materials	K_0 Wm^{-1}°C^{-1}	$k \times 10^5$ m$^2 s^{-1}$	$\lambda \times 10^5$ °C^{-1}
Gray Iron (Gundlach, 1983)	45.45	1.368	-0.253026
A315 (Overfelt, 2001)	128.65	5.9552	0.914108
A356 (Sok, 2006)	150.01	7.9	0.712619

a)

b)

Fig. 2. Evolutions of the dimensionless temperature on the contact surface during constant sliding, for two friction pairs: a) gray iron - A356, b) A315 - A356, for *Bi* = 5. The solid curves – termosensitive materials; the dashed curves – constant properties

a)

b)

Fig. 3. Evolutions of the dimensionless temperature on the contact surface during linearly decreasing velocity of sliding for two friction pairs: a) gray iron - A356, b) A315 - A356, for *Bi* = 5. The solid curves – termosensitive materials; the dashed curves – constant properties

For this pair of friction: gray iron - A356 (Fig. 2a), taking into account the thermal sensitivity of the materials causes a slight increase of temperature in comparison with the temperature evolution calculated without taking into account thermal sensitivity of materials. Thermal conductivity of gray iron is three times less than the thermal conductivity of the material A356, which makes the temperature for this material on the contact surface is always greater, from the beginning of the friction process to the end. Decrease of the thermal conductivity of gray iron with temperature, causes increase in the temperature on the contact surface.
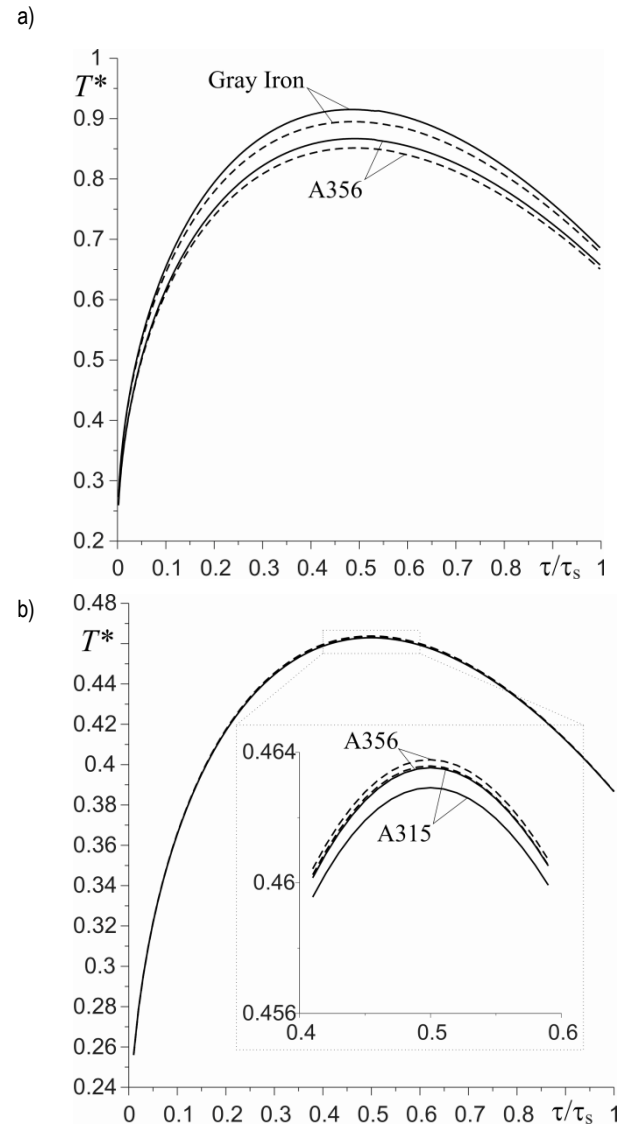
A different situation can be observed in Fig. 2b, where for the friction pair A315 - A356 the evolutions of temperature are shown. Because of close values of thermal conductivity of both materials (see Tab. 1), the evolutions of the temperature on the contact surface are almost the same, whether it takes into account the thermal sensitivity or not. Increase of the thermal conductivity with temperature, reduces the temperature on the contact surface.

The evolution of dimensionless temperature on the contact surface with linearly decreasing velocity from the nominal value at the start of heating to zero during a stop (braking with constant delay) is presented in Figs. 3.

For both pairs of friction, i.e. Gray iron - A356 (Fig. 3a) and A315 - A356 (Fig. 3b), with the beginning of the braking, temperature on the contact surface increases rapidly, reaching a maximum value in the middle of heating time, and then begins to decrease until it reaches a minimum value at the stop time. Taking into account changes in thermo-physical properties of materials under the influence of temperature, for both pairs of friction it causes the same changes in the evolution of the temper-

ature as in the case of constant sliding velocity.

Using Duhamel's formula and obtained solution to the heat conduction problem of friction in the case of a constant sliding speed of two homogeneous semi-space, the mathematical model has been proposed to calculate the non-stationary temperature fields with a linear velocity sliding (braking with uniform delay). The solutions obtained in this article can be used as an introduction to further research on determining distribution of temperature in friction pairs, taking into account changes in their thermal properties under the influence of temperature.

Notations: a – characteristic dimension; Bi – Biot number; c – specific heat; $erf(\ )$ – Gauss error function; $\mathrm{erfc}(x) = 1 - \mathrm{erf}(x)$; $\mathrm{ierfc}(x) = \pi^{-1/2}e^{-x^2} - x\mathrm{erfc}(x)$, f – coefficient of friction; h – coefficient of thermal conductivity of contact; K – coefficients of thermal conductivity; k – coefficients of thermal diffusivity; p_0 – pressure; T – temperature; T^* – dimensionless temperature; T_0 – initial temperature, t – time; t_s – breaking time; V_0 – constant speed; z – spatial coordinate.

Greek symbols: Θ – Kirchhoff's variable; τ – dimensionless time; τ_s –dimensionless breaking time; ξ – dimensionless spatial coordinate; λ – coefficient.

Subscripts: 1 – top semi-space; 2 – bottom semi-space.

REFERENCES

1. **Abdel-Aal H.A.** (1997), On the distribution of friction-induced heat in the dry sliding of metallic solid pairs, *Int. Comm. Heat Mass Trans.*, Vol. 24, No. 7, 989–998.
2. **Abdel-Aal H.A., Smith S.T.** (1998), On friction-induced temperatures of rubbing metallic pairs with temperature-dependent thermal properties, *Wear*, Vol. 216, No. 1, 41–59.
3. **Bateman H., Erdelyi A.** (1954), *Tables of integral transforms*, V. 1, McGraw-Hill, New York.
4. **Fazekas G.A.G.** (1953), Temperature gradient and heat stresses inbrakes drums, *SAE. Trans.*, Vol. 61, No. 1, 279–284.
5. **Gundlach, R.B.** (1983), The effects of alloying elements on the elevated temperature properties of gray irons. (Retroactive Coverage),, *Transactions of the American Foundrymen's Society*, Vol. 91, 389–422.
6. **Kirchhoff G.R.** (1894), *Vorlesungen über die Theorie der Wärme*, B.G. Teubner, Leipzig.
7. **Kuciej M.** (2012), *Analytical models of transient frictional heating*, Oficyna Wydawnicza Politechniki Bialostockiej, Bialystok (in Polish),.
8. **Kushnir R.M., Popovych V.S.** (2011), Heat conduction problems of thermosensitive solids under complex heat exchange. In: *Heat conduction – Basic Research*, V. Vikhrenko Ed., 131–154, In Tech, Croatia.
9. **Ling F.F.** (1973), *Surface Mechanics*, John Wiley&Sons, New York.
10. **Nowinski J.** (1962), Transient thermoelastic problem for an infinite medium with a spherical cavity exhibiting temperature-dependent properties, *J. Appl. Mech.*, Vol. 29, 399–407.
11. **Overfelt R.A., Taylor R.E., Bakhtiyarov S.I., Wang D.** (2001), Thermophysical properties of 319 aluminum, compacted graphite iron, and inconel 713, *AFS Transactions*, 02-115, 141–150.
12. **Ozisik M.N.** (1980), *Heat conduction*, New York, John Wiley, 687 p.
13. **Sneddon I.N.** (1972), *The use of integral transforms*, McGraw-Hill, New York.
14. **Sok W.K.** (2006), Thermophysical properties of automotive brake disk materials, *International Forum on Strategic Technology* (*IFOST*),, 18-20 Oct. 2006, 163–166, Ulsan.
15. **Yevtushenko A.A., Kuciej M.** (2012), One-dimensional thermal problem of friction during braking: The history of development and actual state, *Int. J. Heat Mass Trans.*, Vol. 55, No. 15–16, 4148–4153.

EXPERIMENTAL SETUP FOR TESTING ROTARY MR DAMPERS
WITH ENERGY HARVESTING CAPABILITY

Bogdan SAPIŃSKI*, **Marcin WĘGRZYNOWSKI****

*AGH University of Science and Technology, Faculty of Mechanical Engineering and Robotics, Department of Process Control,
Al. Mickiewicza 30, 30-059 Kraków, Poland

deep@agh.edu.pl, mweg@agh.edu.pl

Abstract: The experimental setup has been developed for laboratory testing of electromechanical energy transducers and rotary magnetorheological (MR) dampers. The design objectives are outlined and the parameters of the key elements of the setup are summarised. The structure of the mechanical and measurement and control systems is presented. Results of functional testing of a newly developed transducer and a MR rotary damper are summarised.

Key words: MR Rotary Damper, Experimental Setup, Energy Harvesting

1. INTRODUCTION

Conventional semi-active vibration reduction systems require an external source of energy. Recently a great deal of attention has been given to semi-active self-powered systems utilising the recovered energy of vibrations (Wang et al., 2009, 2010; Sapiński, 2011; Zhu et al., 2012; Wang and Bai, 2013; Li et al., 2013). Such systems incorporate electromechanical transducers which convert the mechanical into electrical energy.

The experimental setup was constructed for testing the main subassemblies of semi-active vibration reduction systems capable of recovering the energy of rotating motion which are an electromechanical transducer and a MR damper. Mechanical energy is generated by a rotating object (a disk in a flywheel, powered by an electric motor), the energy conversion is effected through the use of a rotary electromechanical transducer whilst electric energy (load) is taken up by a rotary MR damper. The functional testing of the setup is summarised, testing was done on a newly developed electromechanical transducer (Sapiński and Krupa, 2011) and a MR damper (Sapiński and Szydło, 2013).

An experimental setup for similar tests is described in works (Vavreck and Ho, 2005; Młot, 2007; An and Kwon, 2003; Sapiński and Bydłoń, 2002). The experimental setup for testing the characteristics of a rotary MR damper under the torsion is presented in Vavreck and Ho (2005). The work (Młot, 2007) investigates the setup for testing electric motors and electromechanical transducers, while An and Kwon (2003) focuses on testing of power elements filled with MR fluid, including rotary MR dampers. The work (Sapiński and Krupa, 2011) explores the applications of MR dampers to control rotational speed.

2. EXPERIMENTAL SETUP

Underlying the structure of the experimental setup are the design objectives and requirements. Utmost care was taken to ensure easy adaptability of the setup configuration, to enable the testing of transducers, dampers and MR dampers with the energy recovery capability without the needs of major restructuring and to implement the rotary motion in both directions, at the maximal

speed ω_{max}= 600 [rpm]. Finally, the serial structure was adopted in which all elements are configured coaxially, as shown in the schematic diagram Fig. 1, revealing the most expanded version, incorporating an MR damper with the energy recovery capability (MR damper connected with an electromechanical energy transducer). The internal damping in the shafts, pivots and couplings is neglected. The operational characteristics of the driving motor BSM90N (manufactured by BALDOR (http://www.baldor.com/) and of the electromagnetic transducer are assumed to be known beforehand. Basing on the manufacturer's data on the rotary MR damper RD–2087–01 (http://openi.nlm.nih.gov) supplied by the LORD Co., the variability range of torque is assumed 0.4−10 [Nm], the maximal speed ω_{max}= 600 [rpm]. Torsional rigidity (elasticity constants) of couplings of the Toolflex (http://www.ktr.com/de/home.htm) type is taken into account. The manufacturers' specifications and calculation data on the designed assemblies of the driving system were utilised to find the parameters of the test facility (Tab. 1).
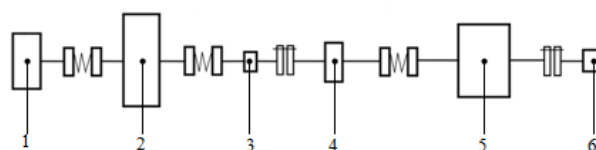

Fig. 1. Experimental setup: 1 − electric motor; 2 − flywheel;
3 − torque meter; 4 − MR damper;
5 − electromechanical transducer; 6 − encoder

Bridle joints are provided at most critical points in consideration of the variable driving torque. This solution enables the transmission of the nominal stationary driving torque and of the acting overloading moment whose instantaneous value may double. As the measuring system in the torque meter are particularly sensitive to overloading, a torque coupling is provided, set on a bridle joint, between the torque meter and the MR damper.

All elements are fixed on the structure made of aluminium profiles (Fig. 2). This construction allows a prompt modification of the setup, at the same time retaining the coaxial array of its constituent elements.

Tab. 1. Parameters of the test facility

Element	Parameter	
	Name	Value
Motor	Mass moment of inertia	3.4·10-4 [kg·m2]
	Nominal torque	6 [N·m]
Flywheel disk	Mass moment of inertia	50·10-4 [kg·cm2]
Torque meter	Mass moment of inertia	0.1·10-4 [kg·m2]
	Torsional rigidity	417.4 [N·m/rad]
MR damper	Mass moment of inertia	0.76·10-4 [kg·m2]
	Torsional rigidity	3762 [N·m/rad]
Transducer	Mass moment of inertia	20·10-4 [kg·m2]
	Torsional rigidity of the shaft	30000 [N·m/rad]
Encoder	Mass moment of inertia	0.05·10-4 [kg·m2]
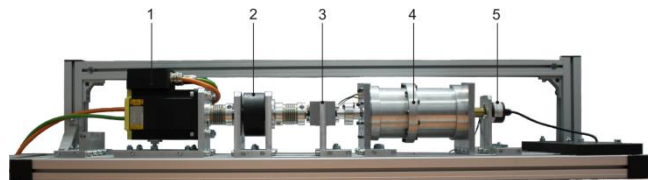
Fig. 2. View of the experimental setup: 1 − motor, 2 − flywheel,
3 − torque meter; 4 − MR damper with energy recovery capability,
5 – encoder
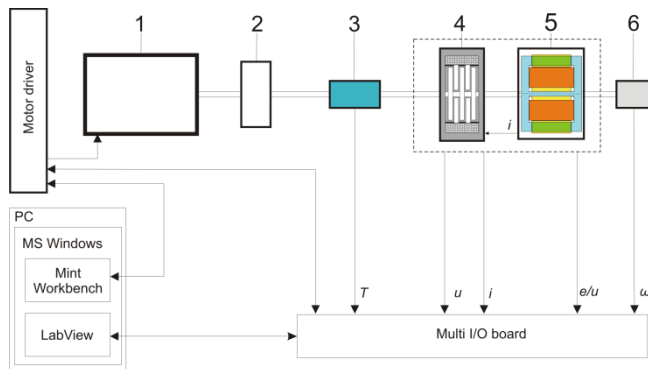
Fig. 3. Schematic diagram of the measurement and control system:
1 − motor, 2 − flywheel, 3 − torque meter, 4 − MR damper,
5 − electromechanical transducer, 6 − encoder

The schematic diagram of the measurement and control system is shown in Fig. 3. The system comprises a control box CompacDAQ (National Instruments) connected to a computer via a USB port, an impulse feeder and the drive element MINT Drive II (controlled by the Mint Workbench software), controlling the electric motor (manufactured by Baldor). The LabView 2010 installed on a PC operates under MS Windows. Analogue modules (NI9227 (http://www.ni.com/pdf/manuals/374068f.pdf), NI9205 (http://www.ni.com/pdf/manuals/374188d.pdf) and a digital module (NI9401 (http://www.ni.com/pdf/manuals/374068f.pdf) are installed in the control box CompacDAQ. The power drive in the motor is connected to the PC via a port RS232. Operating parameters of the motor are adjustable with the use of the Mint Workbench software (setting the controllers' parameters and the operational

parameters) or using the analogue output card in the Compac-DAQ box (adjustment of operational parameters).

3. FUNCTIONAL TESTING

Testing was done on a newly-developed electromechanical transducer and a MR damper to determine their characteristics.

In the first place the dynamic characteristic of the transducer was determined under the step voltage supplied to its coil $u(t)=0.5$ l(t) [V] (Fig. 4). The time constant of the transducer coil was 0.068 [s].
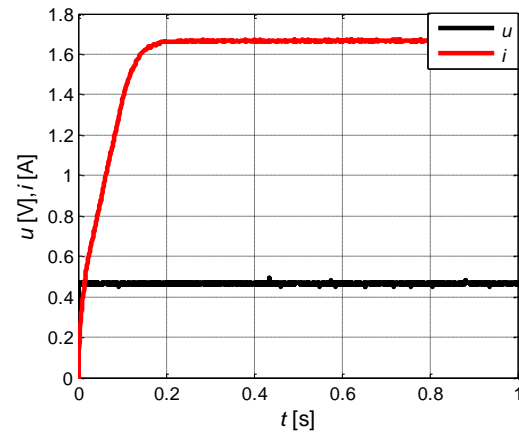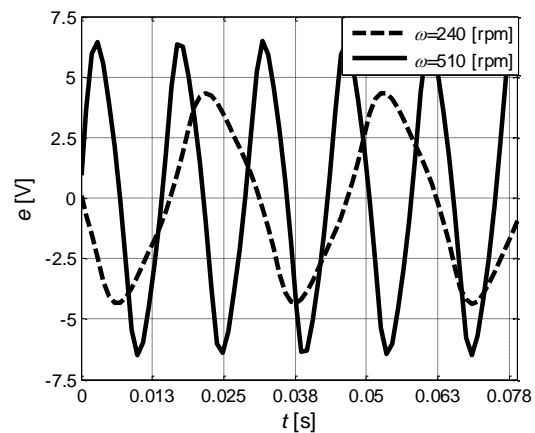

Fig. 4. Dynamic characteristic of the transducer

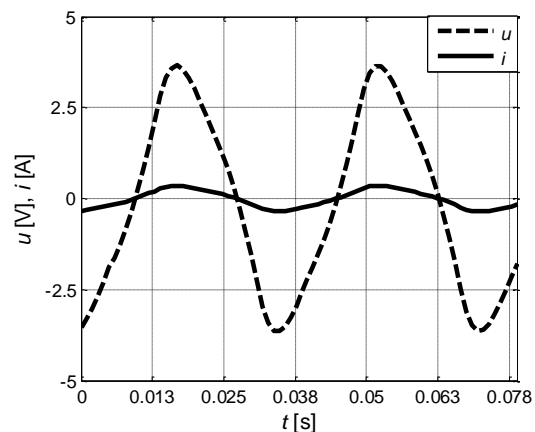**Fig. 5.** Emf force e in the function of time

Fig. 6. Voltage u and current i in the function of time; resistance load

The transducer characteristic was then determined under the idle run and under the resistance loading (10 [Ω]) and resistanceinduction loading (MR damper's control coil) at the rotating speed in range ω (0, 600) [rpm]. The plots of *emf* force under the idle run are shown in Fig. 5, voltage u and current i (under loading) at the rotational speed $\omega=240$ [rpm] are shown in Fig. 6 and 7. It appears that the electromotive force induced in the transducer coil increases with an increase in rotational speed (Fig. 5).
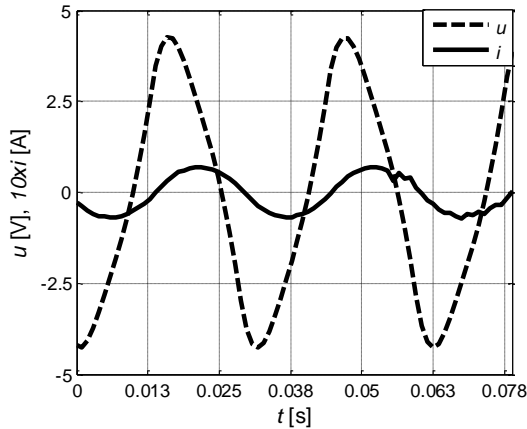

Fig. 7. Voltage *u* and current *i* in the function of time; resistance-induction load
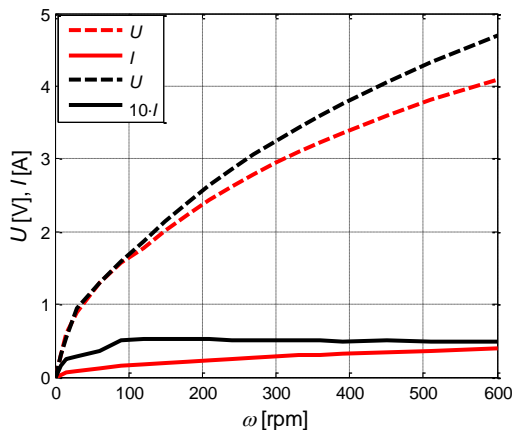

Fig. 8. Rms values of voltage and current under the resistance load and the resistance-induction load

Under the resistance load (grey line), voltage and current the transducer tends to increase with rotational speed. When the transducer is subjected to the load due to the MR damper control coil (black line), the current *i* tends to increase linearly in the velocity range (0, 100) [rpm]. At velocities in excess of $\omega=100$ [rpm], the current reaches the level 0.05 [A] and stabilises despite the further increase of the rotational speed (Fig. 8).

Further tests were done on a MR damper to determine its static T(I) and dynamic i(t) characteristics. Static characteristics were determined under the low frequency sine voltage signal applied to the coil. The dynamic characteristics of the MR damper were obtained under the step voltage changes $u(t) =16\cdot l(t)$ [V] in the control coil (Fig. 9). The time constant of the control coil in the MR damper is 0.052 [s].

Static characteristics of the damper for the unipolar power-supply of the control coil were showed in Fig. 10. It is readily apparent (Fig. 10) that the static characteristics of the MR damper exhibits the hysteresis associated with the properties of its component materials. The maximal ambiguity error for the MR damper is equal to 22.5% of the maximal torque generated by the damper. The initial torque (0.16 [Nm]) is associated with viscous friction and magnetic residues in the damper housing and disks.

On the basis of characteristics of the investigated transducer and the damper it appears that the MR damper with the energy recovery capability is able to generate the maximal torque 0.25 [Nm].
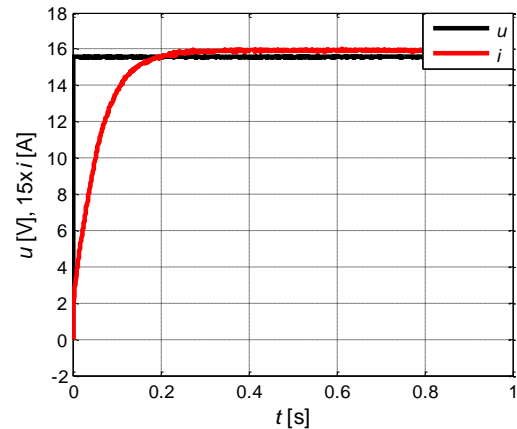

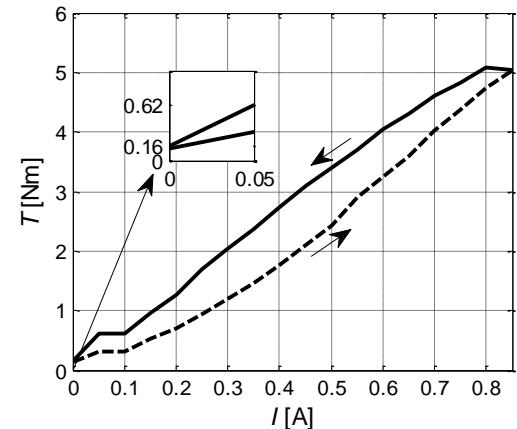**Fig. 9.** Dynamic characteristics of the MR damper

Fig. 10. Static characteristics of the MR damper

4. SUMMARY

The laboratory setup has been designed for testing the MR dampers with the energy recovery capability. The design objectives and the structure of the test facility is outlined, results of testing done on a newly developed rotational transducer and a MR damper are summarised.

High rigidity of the test facility, and carefully selected bearings and couplings help maintain the coaxial array of its all components, at the same time making it modifications easy. Extensive tests revealed that the setup performs well both in the low and high range of rotational speed. Results evidence the correct performance of the measurement and control system, which proves to be insensitive to disruptions and its modular structure makes it easily adjustable and modifiable.

This experimental setup is intended for use for research and teaching in the Laboratory of Adaptronics in the Department of Process Control of AGH−UST.

REFERENCES

1. **An J., Kwon D. S**. (2003), Modeling of a Magnetorheological Actuator Including Magnetic Hysteresis, http://citeseerx.ist.psu.edu/viewdoc/download?doi=10.1.1.101.4352&rep=rep1&type=pdf.

2. **Li Z., Zhuo L., Luhrs G., Lin L., Qin Y. (**2013), Electromagnetic Energy-Harvesting Shock Absorbers: Design, Modeling and Road Tests. *IEEE Transactions on Vehicular Technology*, Vol. 62, no.3, 1065−1074.

3. **Młot A.** (2007), *Structural pulsation dampening methods of the electromechanical torque in a brushless DC motor with permanent magnets*, PhD thesis. Opole University of Technology, Faculty of electrical engineering, Automatic control and informatics. (in Polish)

4. **Sapiński B., Krupa S.** (2011), *Rotary transducer of mechanical energy into electrical energy*, Application for the patent no. P−395 787. (in Polish)

5. **Sapiński B.** (2011), Experimental study of self-powered and sensing MR damper-based vibration control system. *Smart Materials and Structures*, Vol. 20, 105012.

6. **Sapiński B., Bydoń S.** (2002), Application of Magnetorheological Fluid Brake to Shaft Position Control in Induction Motor, *Pneumatyka*, Vol.3, no.34, 27–29. (in Polish)

7. **Sapiński B., Szydło Z.** (2013), Magnetorheological damper for torsional vibration with electromechanical rotary transducer. Application for the patent no. P−403 371 (in Polish)

8. **Vavreck A. N., Ho Ch. H.** (2005), Characterization of a commercial magnetorheological brake/damper in oscillatory motion, *Smart Structures and Materials: Damping and Isolation*, 256−267.

9. **Wang Z. H., Chen, Z. Q. and Spencer, B. F.** (2009), Self-powered and sensing control system based on MR damper, presentation and application, *Proc. of SPIE on Sensors and Smart Structures Technologies for Civil, Mechanical, and Aerospace Systems*, 7292, 729240.

10. **Wang D. H., Bai X. X.(**2013), A magnetorheological damper with an integrated self-powered displacement sensor. *Smart Materials and Structures*, Vol. 22, 075001.

11. **Wang D. H., Bai X. X., Liao W. H.(**2010), An integrated relative displacement self-sensing magnetorheological damper: prototyping and testing. *Smart Materials and Structures*, Vol.19, 105008.

12. **Zhu S. Y., Shen W. A., Xu Y. L., Lee W. C.(**2012), Linear electromagnetic devices for vibration damping and energy harvesting: *Modeling and testing, Engineering Structures*, Vol. 34, 198−212.

13. http://www.baldor.com/

14. http://openi.nlm.nih.gov/detailedresult.php?img=3251984_sensors11 11305f22&query=the&fields=all&favor=none&it=none&sub=none&uni q=0&sp=none&req=4&simCollection=3142198_1477-7525-9-44-1&npos=86&prt=3

15. http://www.ktr.com/de/home.htm

16. http://www.ni.com/pdf/manuals/374068f.pdf

17. http://www.ni.com/pdf/manuals/374188d.pdf

18. http://www.ni.com/pdf/manuals/374068f.pdf